THE CALCULATIONS OF THE FLOW FIELD ABOUT A BLUNTED 9° CONE

FINAL REPORT

GASL Report TR-256

November 6, 1961

Reissued September 18, 1962

The work reported in this document was performed at General Applied Science Laboratory, Inc. for M. I. T. Lincoln Laboratory under Subcontract No. 226; this work was supported by the U.S. Advanced Research Projects Agency under Air Force Contract AF 19(604)-7400 (ARPA Order 13).

TIP CALCULATIONS OF THE FLOW FIELD ABOUT A BLUNTED 9° CONE

FINAL REPORT

TECHNICAL REPORT NO. 256

SECTION I

SUBCONTRACT NO. 226

Prepared For

Massachusetts Institute of Technology
Lincoln Laboratory
Lexington 73, Massachusetts

Prepared By

General Applied Science Laboratories, Inc.
Merrick & Stewart Avenues
Westbury, L.I., New York

November 6, 1961

Approved By: 

Antonio Ferri
President

TABLE OF CONTENTS

THE CALCULATION OF THE FLOW FIELD ABOUT A BLUNTED 9° CONE

SECTION I

CHARACTERISTICS CALCULATIONS

By E. Kennedy, A. Fields, and M. Seidman

SUMMARY

The inviscid flow fields about a hemispherically blunted cone (9° half-angle) have been calculated at five hypersonic Mach numbers. The calculation is begun in the subsonic region by the method of Vaglio-Laurin and Ferri and extended into the near wake by the method of characteristics. The air was taken to be a mixture of perfect gases, either chemically frozen or in thermodynamic equilibrium. Results from these calculations were used as initial data for rate and wake calculations presented in Sections II and III of this report.

I. DISCUSSION

In order to determine flight conditions for the flow field calculations, a reentry trajectory beginning at 22,000 fps, 300,000 feet altitude and flight path angle of 79° was calculated on the Bendix G-15 Computer. With these initial conditions and with $W/C_D A$ constant at 30 lbs/ft^2, a ballistic trajectory passes through the following points in the h-v plane.

h	v
250,000	22,550 fps
200,000	22,475 fps
150,000	21,600 fps
100,000	15,875 fps
80,000	9,150 fps

Some work of Bloom and Steiger (summarized in Reference 1) indicated that at the three higher altitudes the flow would be chemically frozen downstream of the nose region while at the two lower altitudes it would be closer to equilibrium. Accordingly, at the lower altitudes both equilibrium and frozen calculations were run and only the frozen case at 150,000 feet and above. The details of the calculation are given by Vaglio-Laurin and Bloom in Reference 1 and need not be repeated here. Some difficulty was experienced in beginning the frozen calculation from the equilibrium calculation in the subsonic and transonic region. This difficulty was traced to the difference between the frozen and equilibrium speeds of sound and resulted in subsonic velocities in the frozen flow calculations. This, of course, violates a fundamental requirement for the existence of real characteristics

and stops the calculation. The solution was to begin the characteristics calculation a little further from the sonic line so that the reduced "frozen" Mach number was still greater than one. This allowed the calculation to proceed to the end of the body without interruption. In order to develop the flow field about the base of the body and in the near wake, it was necessary to estimate the base pressure and the position of the wake shock. The base pressure was estimated by the method of Chapman (2) and, in general, was several times the ambient pressure. The wake shock began at a point on the constant pressure streamline one-half the base radius from the axis. These admittedly approximate techniques enable one to bridge the base region where the flow processes are fundamentally dissipative and are not yet to well understood. The calculation was then extended downstream for about 20 more radii where the pressure on the axis (more correctly, on the constant diameter core region postulated in the near wake) approached that of the atmosphere. It should be pointed out that the pressure near the bow shock at this station was still considerably above the ambient.

Sufficient data were now available to trace individual streamlines from the bow shock to the beginning of the far wake. Four such streamlines for each flight condition are shown in Figures 1 through 7. With the pressure distribution along these streamlines given by the characteristics analysis, the rate calculations of Section II were performed and the results used to start the wake calculations of Section III.

Aside from the rate and wake calculations, the distribution of flow properties about the body itself is not without interest. Figures 8 through 11 show profiles of thermodynamic data (p, ρ , and T) and electron density at a station 1 1/2 nose radii from the nose and Figures 12 through 15 show the same data at the base of the cone. (In the case of frozen flow, the electron density was calculated by assuming the reaction $N + O \longrightarrow NO^{+} + e^{-}$ to be the only significant electron-producing one and it to be in equilibrium at the state determined by the frozen field). In Figures 12 through 15 , both the inviscid (i.e. characteristics) calculations and the modification of these profiles due to the boundary layer are shown. The boundary layer was calculated by two different methods according to the altitude. At the three lower altitudes, the method of Reference 3 with $\beta = 0$ was used. The flow at the wall was assumed to be in equilibrium at the assumed wall temperature ($1000^{\circ}K$). It has been shown (Reference 4) that for Lewis and Prandtl numbers of one, the mass fractions and stagnation enthalpy obey a Crocco-type relationship and so the solutions of Reference 3 are directly applicable once the free stream or edge conditions are known. The edge of the boundary layer was determined by matching the mass flow within the boundary layer with that in the inviscid layer. (Note that this requires an iterative procedure in order to determine the edge).

In the case of the higher altitudes (200,000 and 250,000 feet) the shear in the inviscid flow approaches that at the wall in the boundary layer solution (Reference 5) and some modification of the above procedure is necessary. Methods of calculation for this case are available in References 6 and 7. The

method of Reference 7 with the same wall conditions (i.e. equilibrium flow at 1000°K) as before were used. In this solution the velocity and shear are matched in the two solutions (viscous and nonviscous) in order to determine the edge of the viscous layer. The Crocco relationship was assumed to remain valid in this case and furnished the concentration and stagnation enthalpy profiles.

The triangular symbols on Figures 12 are the values given by the nonequilibrium streamline calculation. (Since the equilibrium electron density at 80,000 feet is rather low ($\sim 10^5 - 10^4$/cc), this case is missing from Figures 8 through 12.)

REFERENCES

1. Vaglio-Laurin, R., and Bloom, M. H., Chemical Effects in External Hypersonic Flows, International Hypersonics Conference, M. I. T., August 1961.

2. Chapman, Dean R., An Analysis of Base Pressure at Supersonic Velocities and Comparison with Experiment, NACA Report No. 1051, 1951.

3. Cohen, C. and Reshotko, E., Similar Solutions for the Compressible Laminar Boundary Layer With Heat Transfer and Pressure Gradient, NACA Report 1293, 1956.

4. Vaglio-Laurin, R., Heat Transfer on Blunt Nosed Bodies in General Three-Dimensional Hypersonic Flow, 1959 Heat Transfer and Fluid Mechanics Institute

5. Ferri, A., Some Heat Transfer Problems in Hypersonic Flow, PIBAL Report No. 473, July 1959.

6. Ferri, A., Zakkay, V., and Ting, L., Blunt Body Heat Transfer at Hypersonic Speed and Low Reynolds Numbers, PIBAL Report No. 611, June 1960

7. Rogers, Ruth H., The Development of the Boundary Layer in Supersonic Shear Flow, RAE TN Aero 2738, January 1961.

TABLE 1 - MASS FRACTIONS

Streamline	m_{O_2}	m_O	m_N	m_{N_2}	m_{NO}
		250,000			
Body	.000012	.236	.28	.482	.0013
A	.00002	.236	.194	.568	.0019
B	.00015	.235	.0300	.732	.0037
C	.104	.118	.000014	.750	.0275
D	.210	.0215	--	.759	.0099
		200,000			
Body	.00003	.235	.290	.472	.0025
A	.00009	.235	.134	.626	.0044
B	.0027	.227	.00461	.753	.0131
C	.143	.078	--	.749	.0302
D	.237	--	--	.763	--
		150,000			
Body	.0001	.233	.21	.5535	.0064
A	.0004	.231	.0651	.694	.0102
B	.0608	.153	.0002	.744	.0414
C	.1975	.0173	.000012	.745	.0407
D	.237	--	--	.763	--
		100,000			
Body	.0076	.213	.007	.742	.0300
A	.0476	.1581	.0009	.7341	.0593
B	.1451	.0620	.000046	.7362	.0567
C	.237	--	--	.763	--
D	.237	--	--	.763	--
		80,000			
Body	.22	.0035	1.8×10^{-7}	.7515	.025
Others	No Dissociation .				

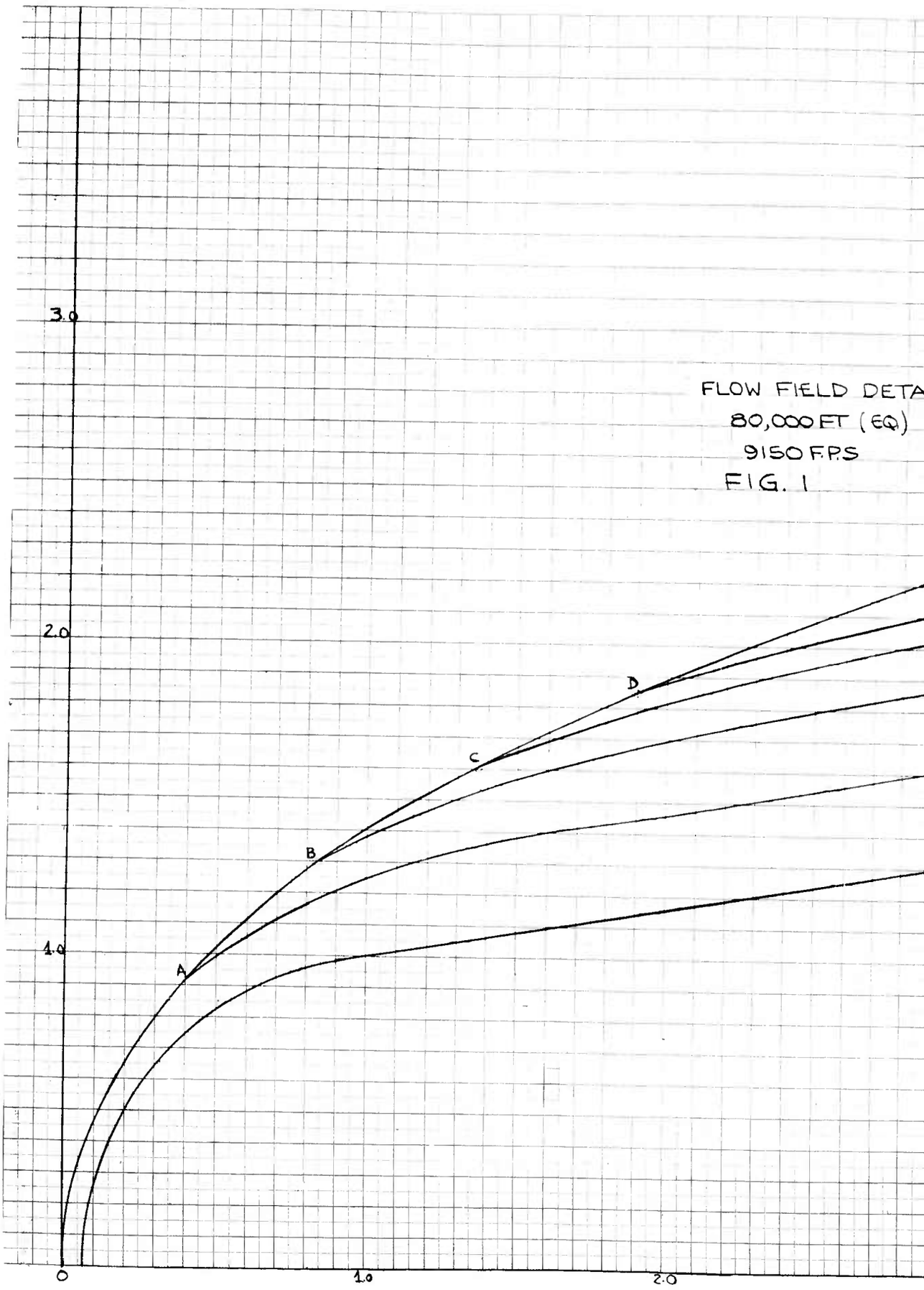

FLOW FIELD DETA
80,000 FT (EQ)
9150 F.P.S
FIG. 1

1

FLOW FIELD DETAILS
80,000 FT (EQ)
9150 F.P.S
FIG. 1

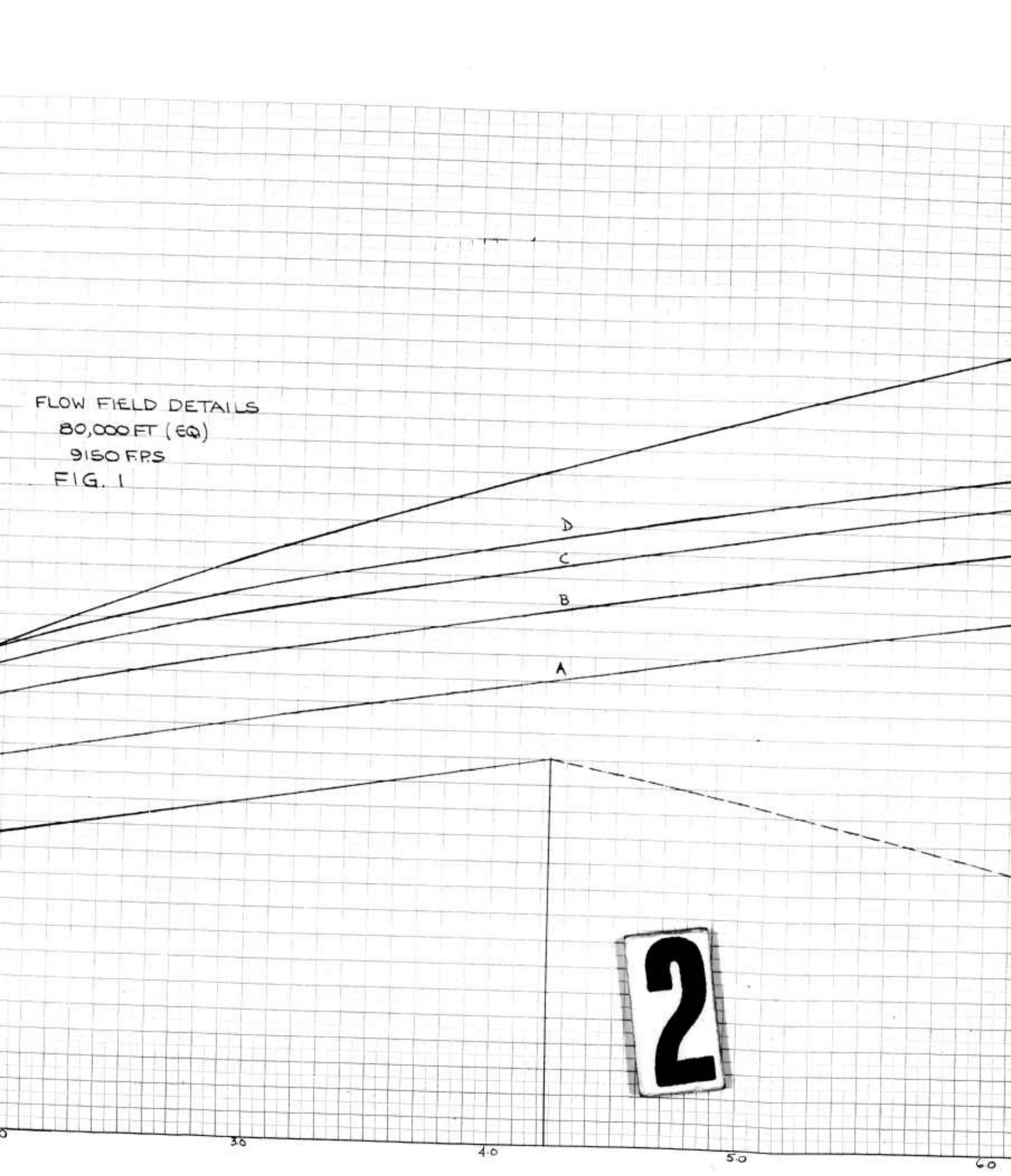

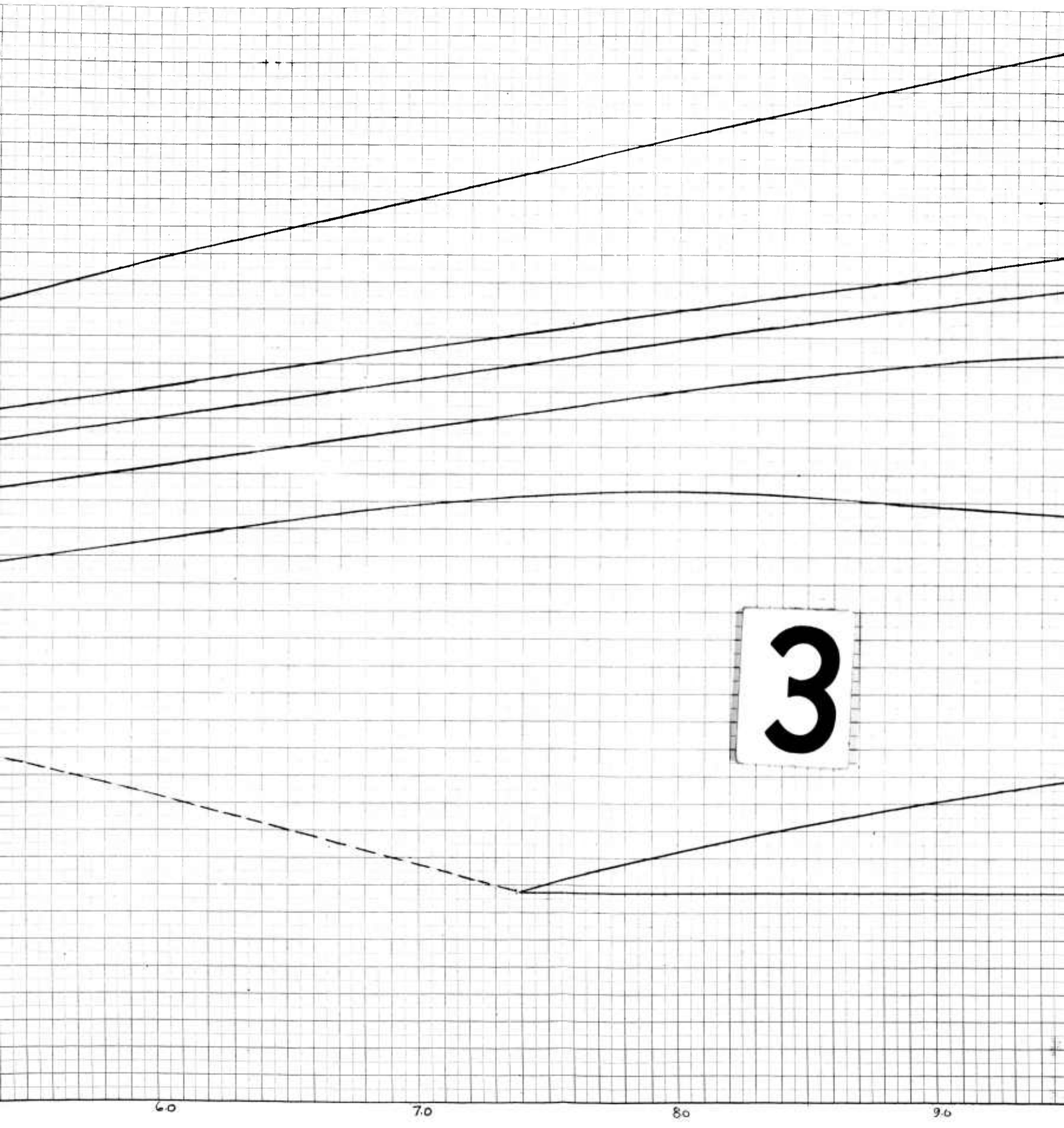
3
6.0
7.0
8.0
9.0

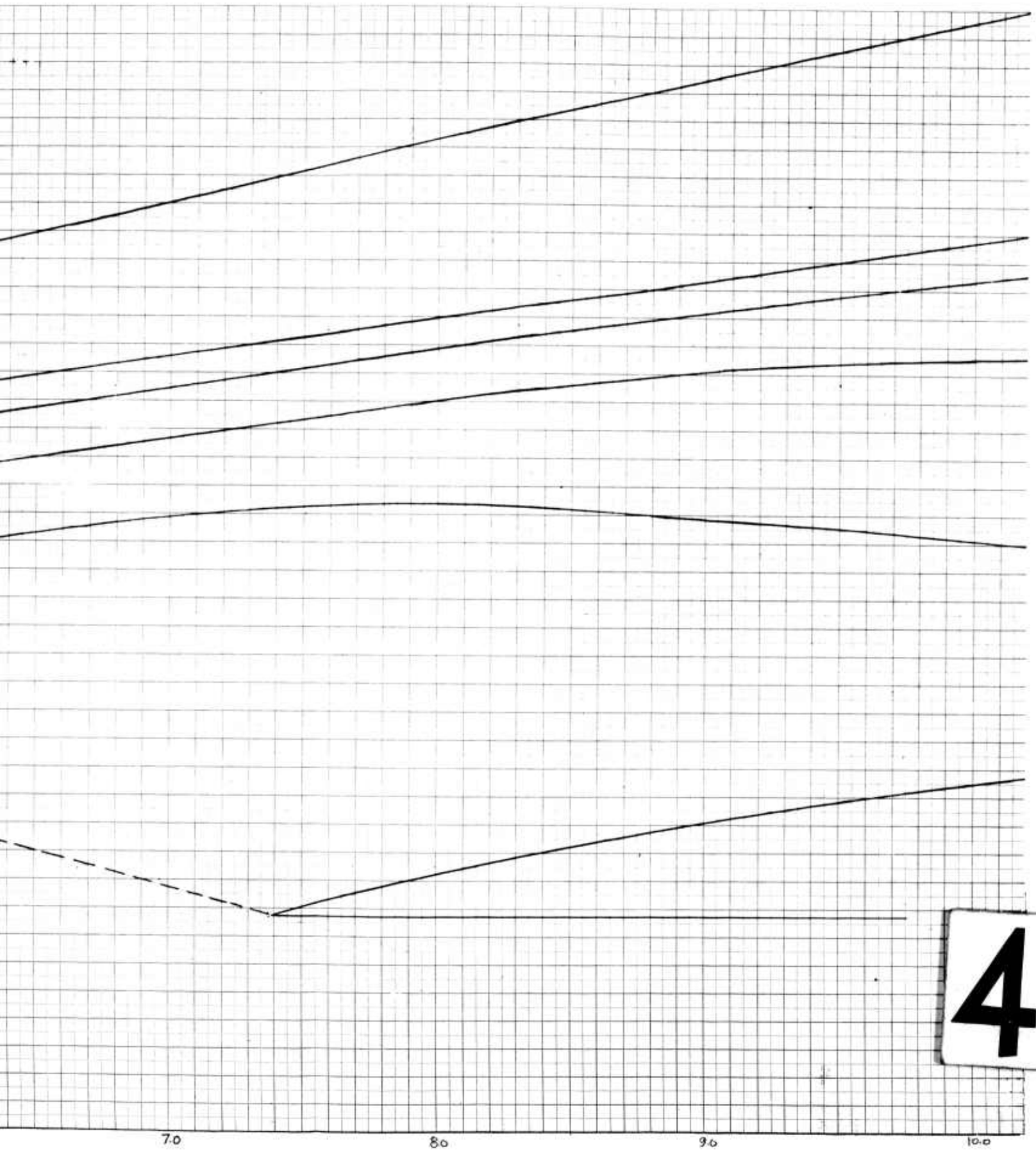
7.0
8.0
9.0
10.0
4

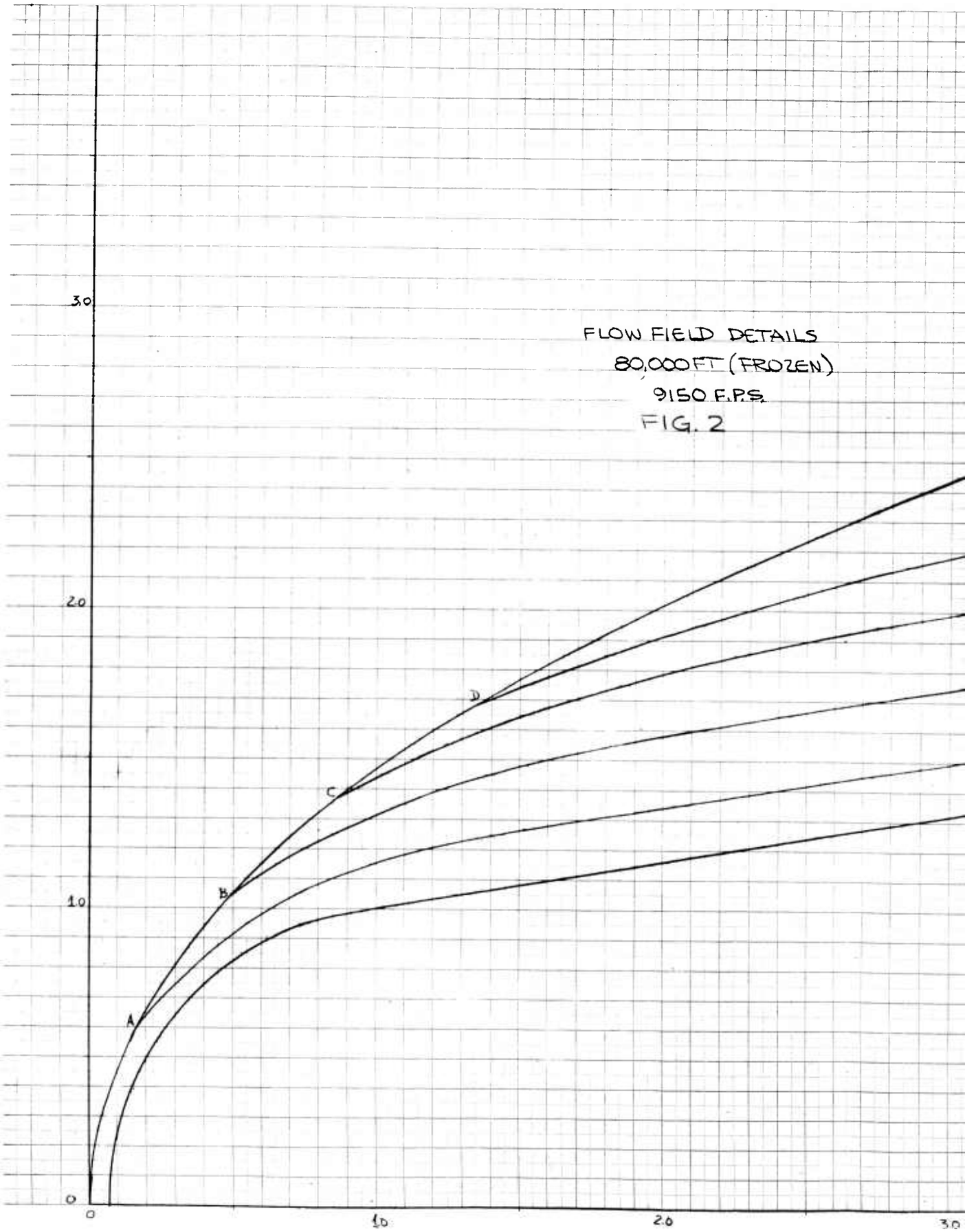

FLOW FIELD DETAILS
80,000 FT (FROZEN)
9150 F.P.S.
FIG. 2

1

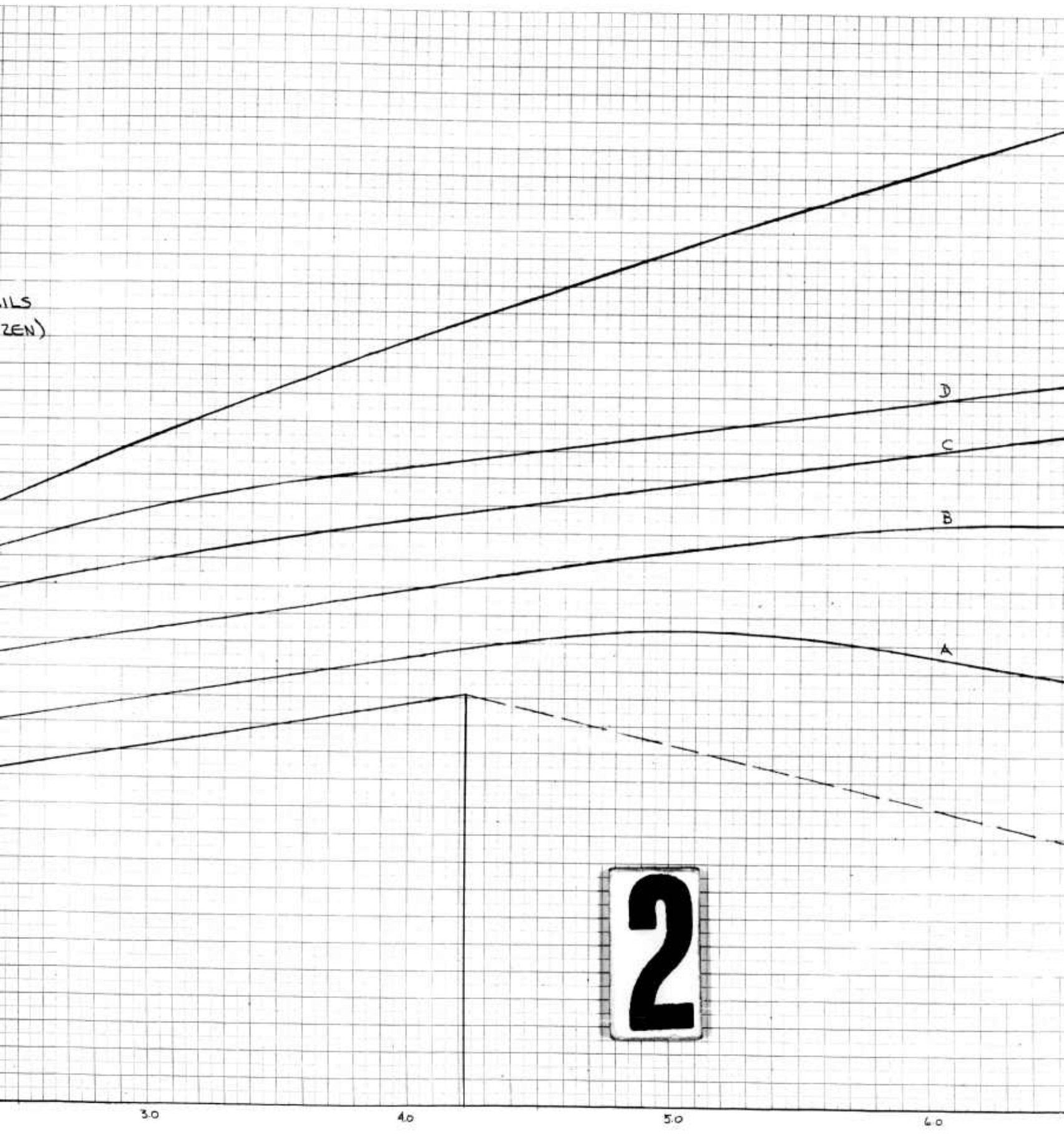
ILS
ZEN)
D
C
B
A
2
3.0
4.0
5.0
6.0

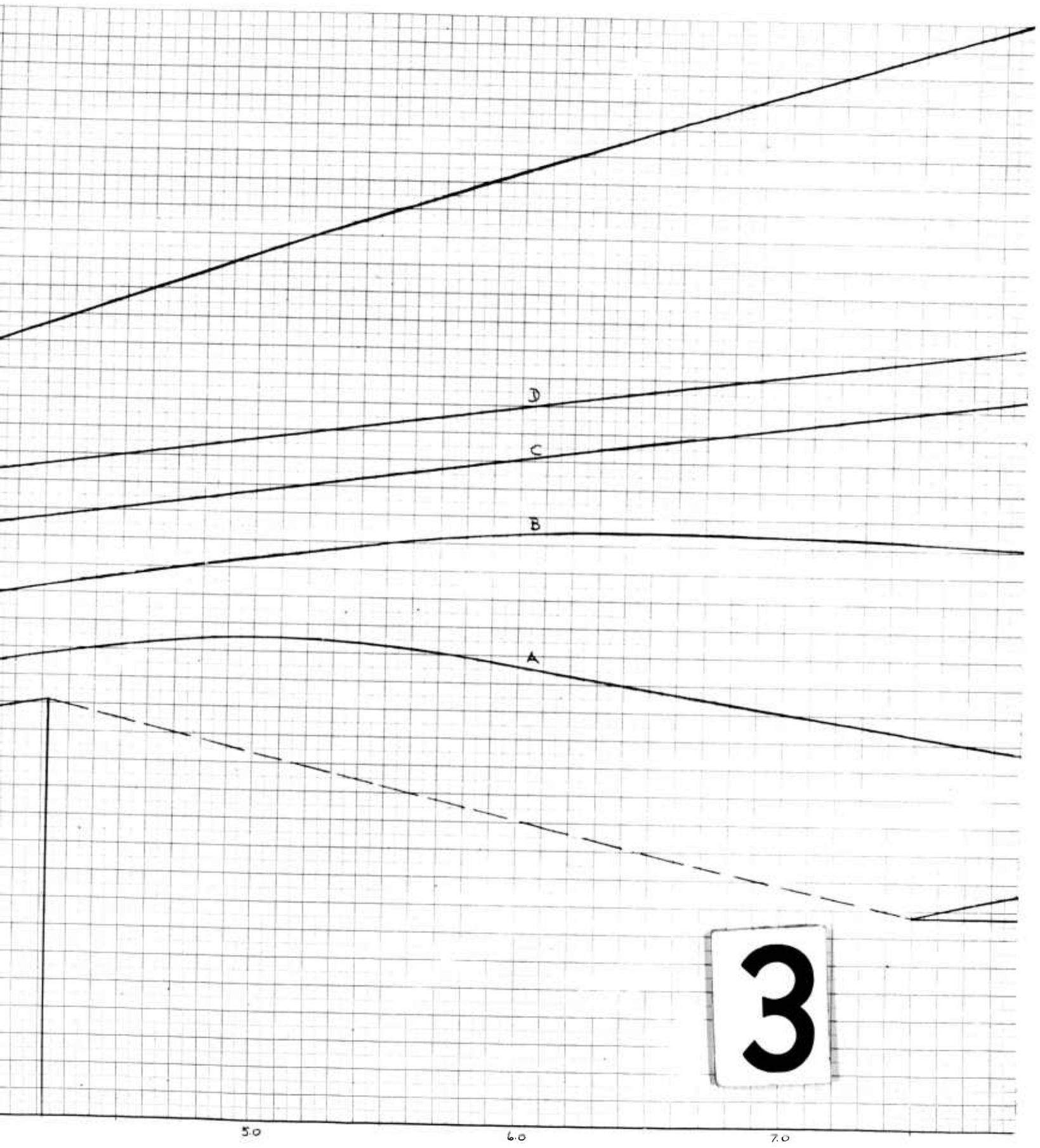
D
C
B
A
5.0
6.0
7.0
3

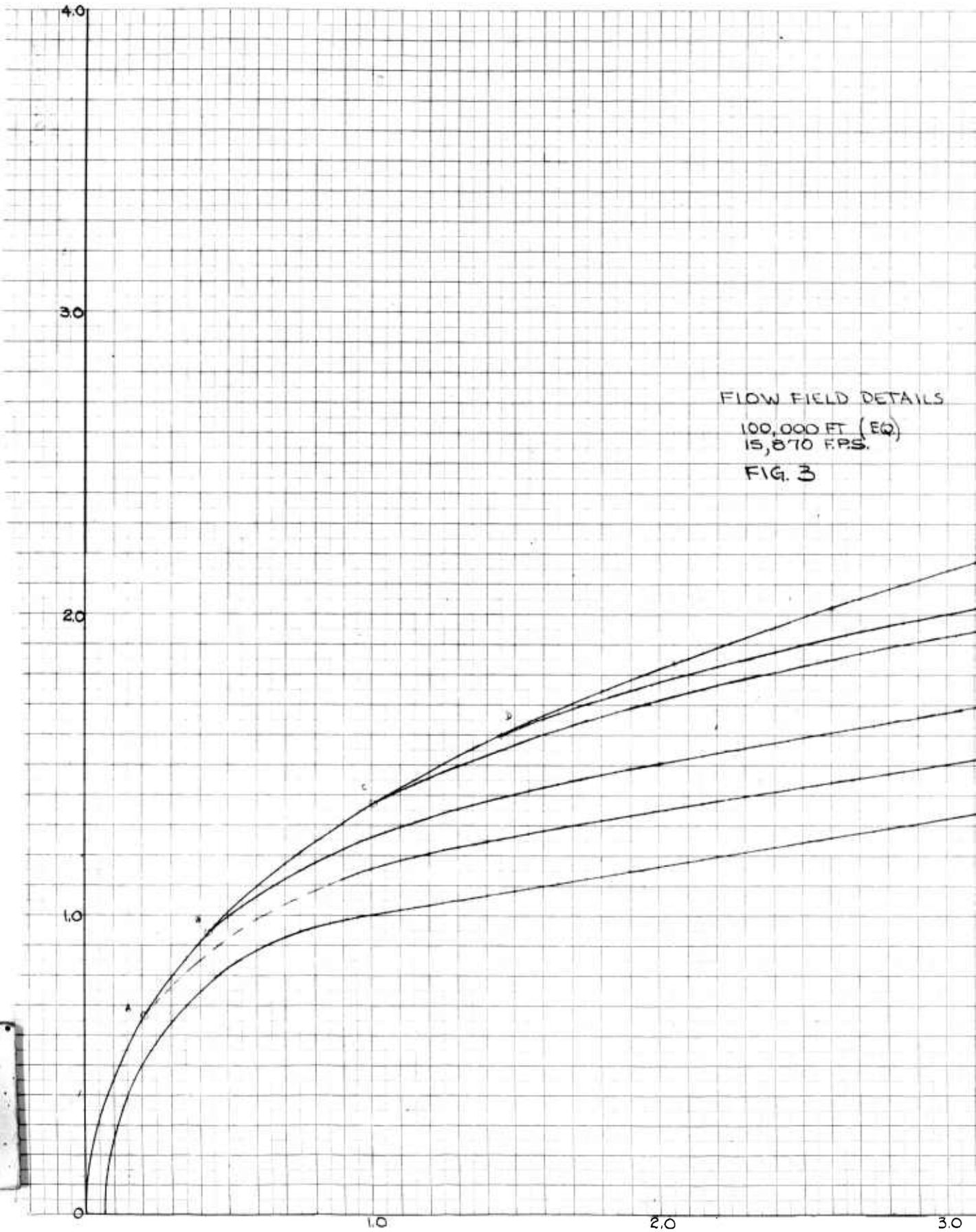
4.0
3.0
2.0
1.0
0
1.0
2.0
3.0
FLOW FIELD DETAILS
100,000 FT (EQ)
15,870 F.P.S.
FIG. 3

1

FIELD DETAILS

00 FT. (EQ.)
10 F.P.S.

3

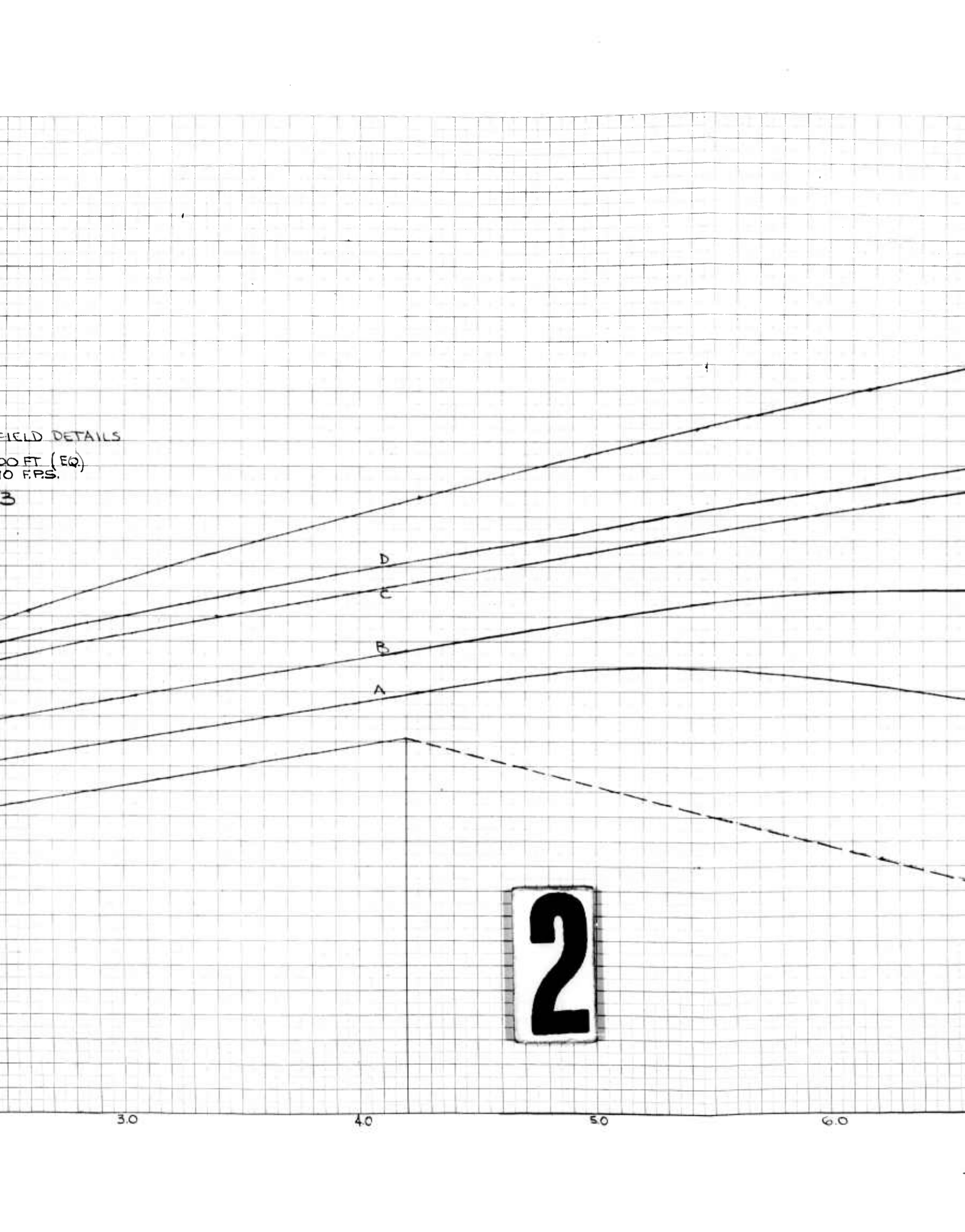

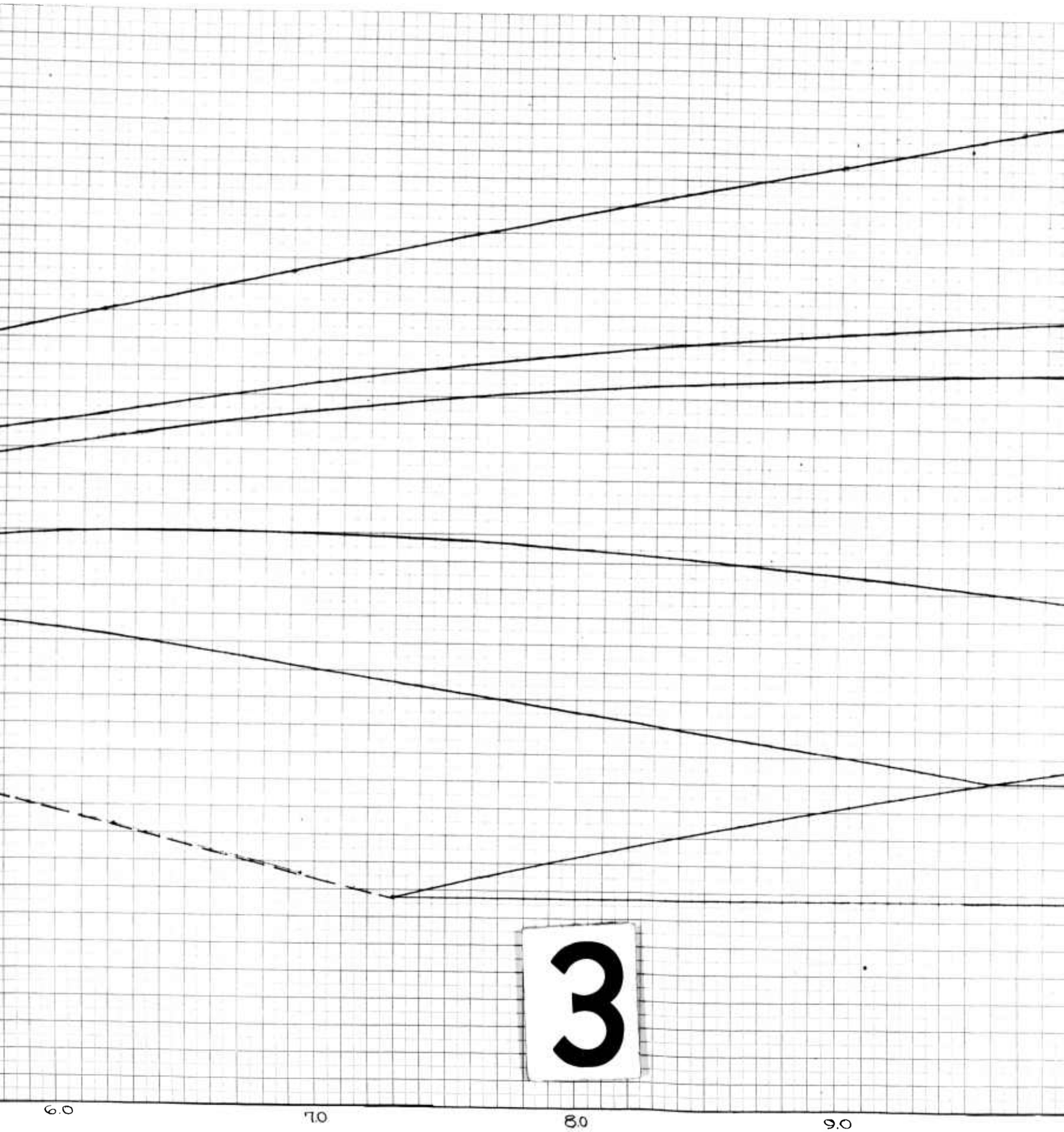
3
6.0
7.0
8.0
9.0

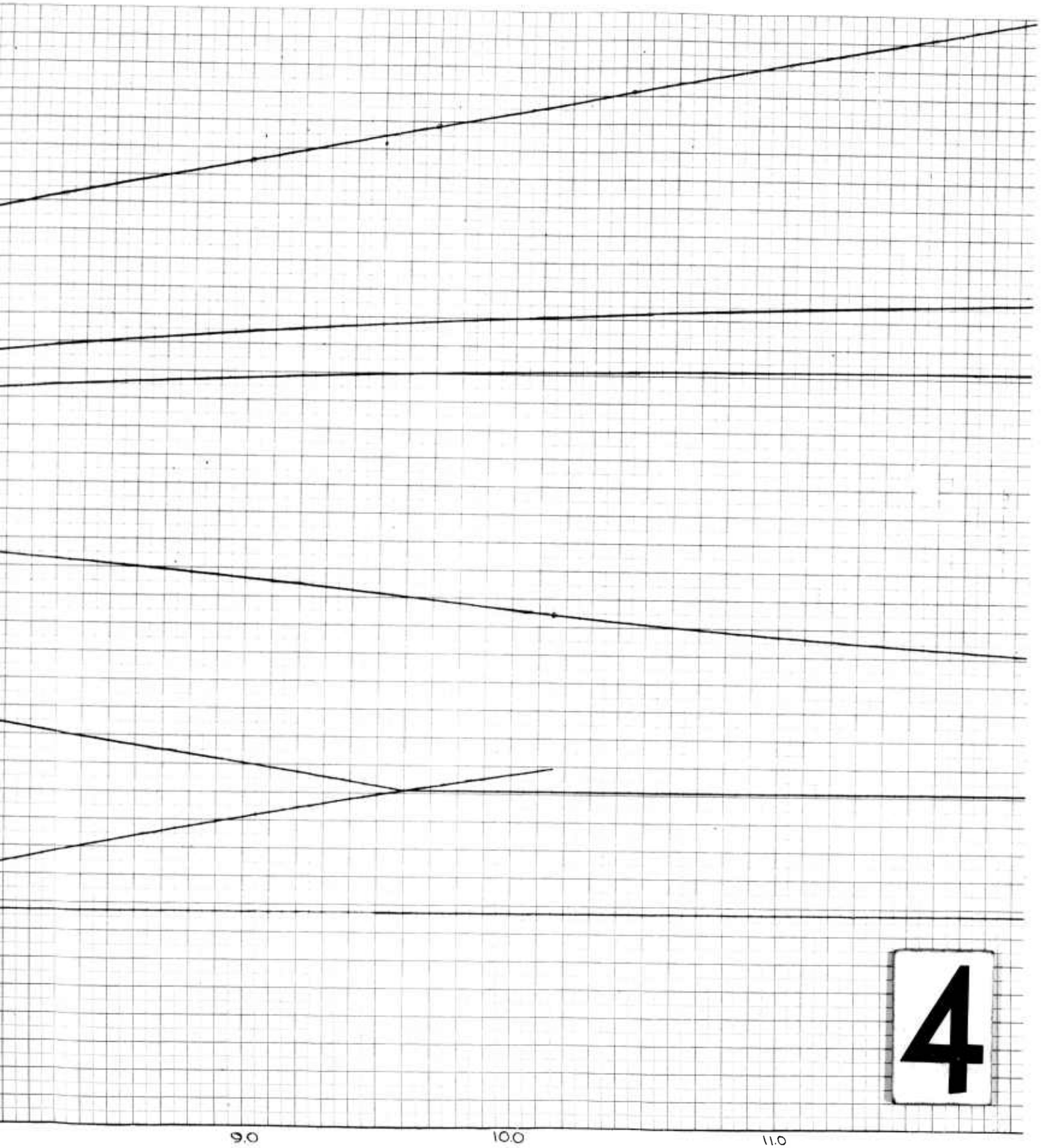
4
9.0
10.0
11.0

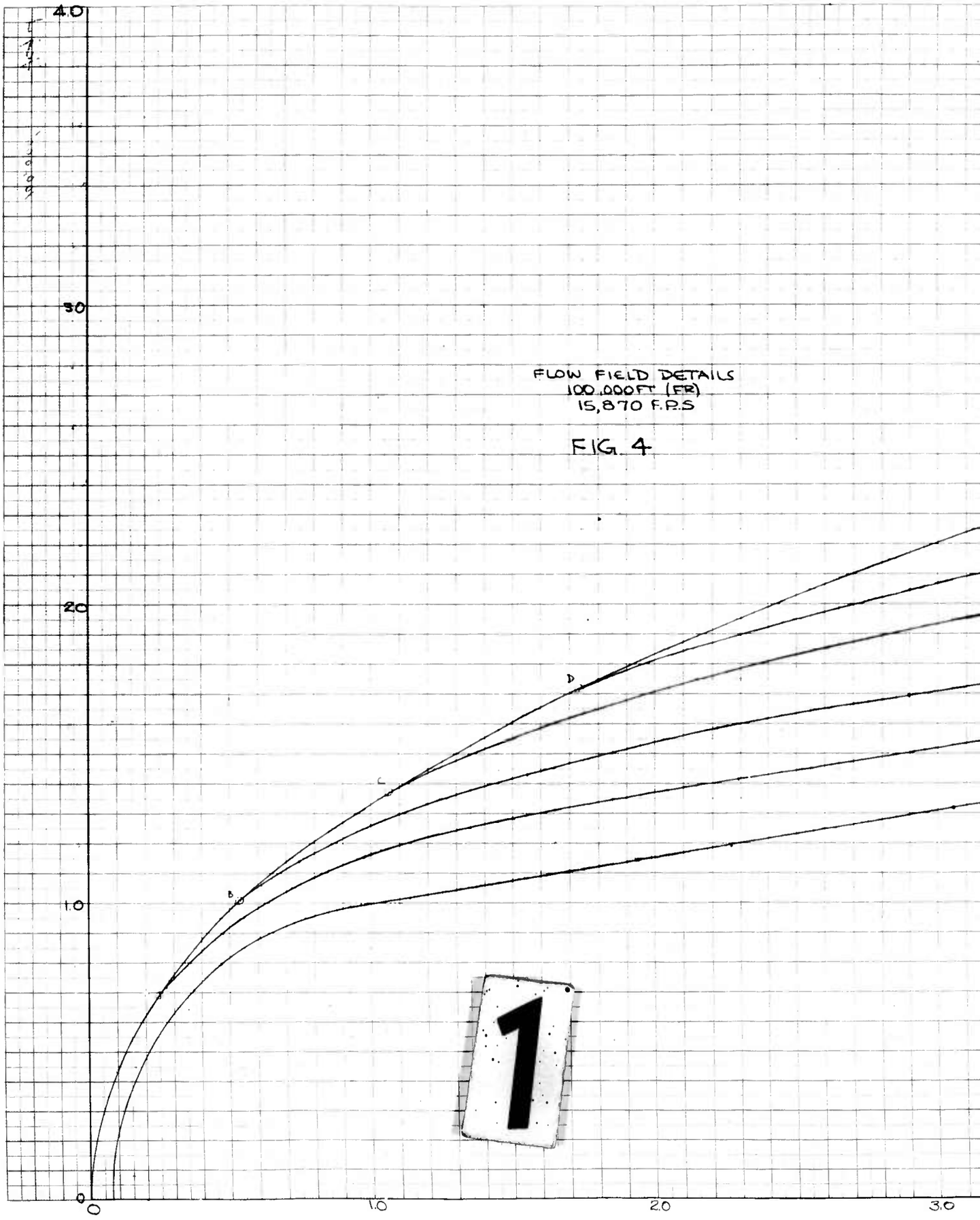

FLOW FIELD DETAILS
100,000 FT (FR)
15,870 F.P.S

FIG. 4

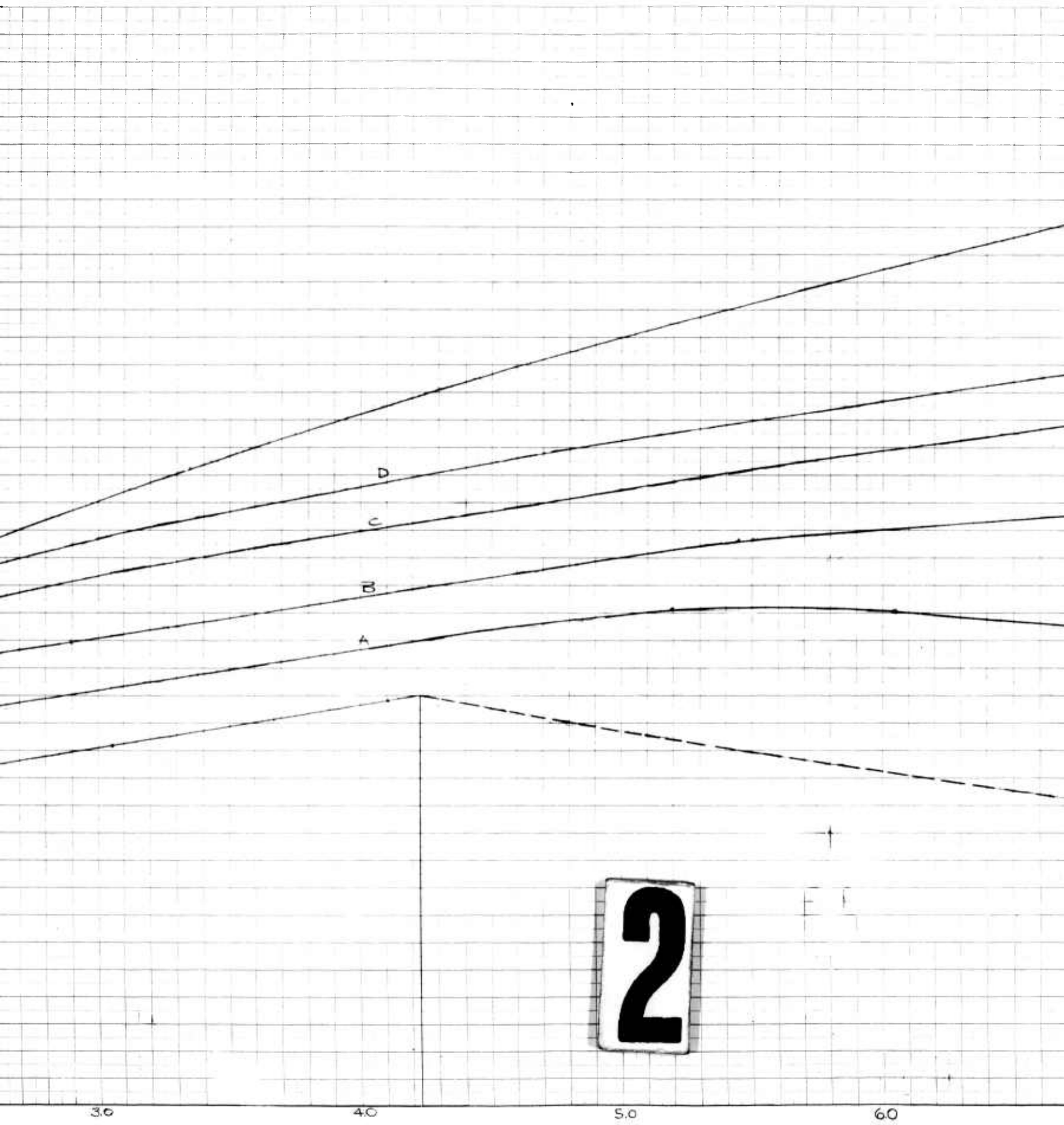
D
C
B
A
3.0
4.0
5.0
6.0

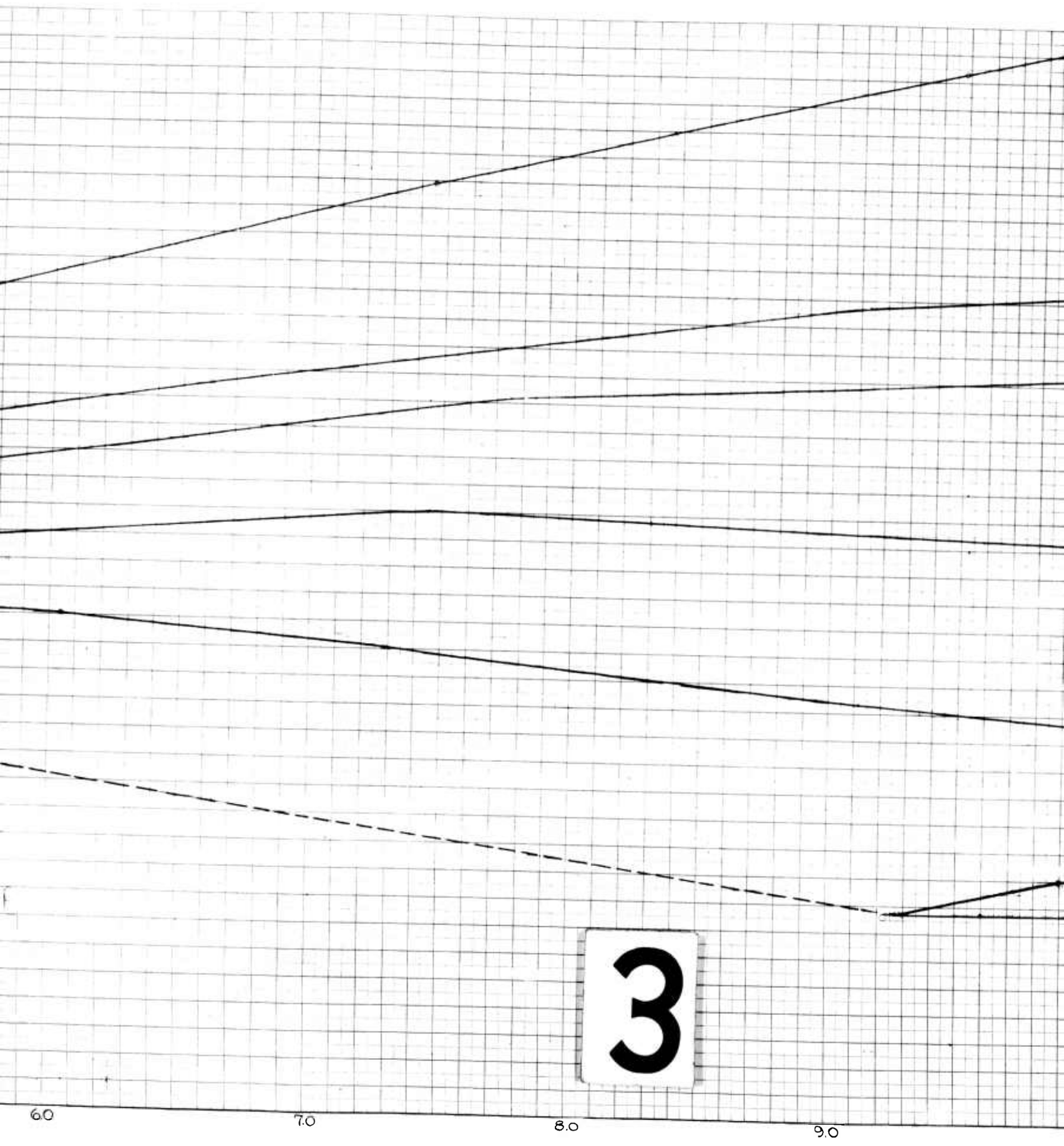
3
6.0
7.0
8.0
9.0

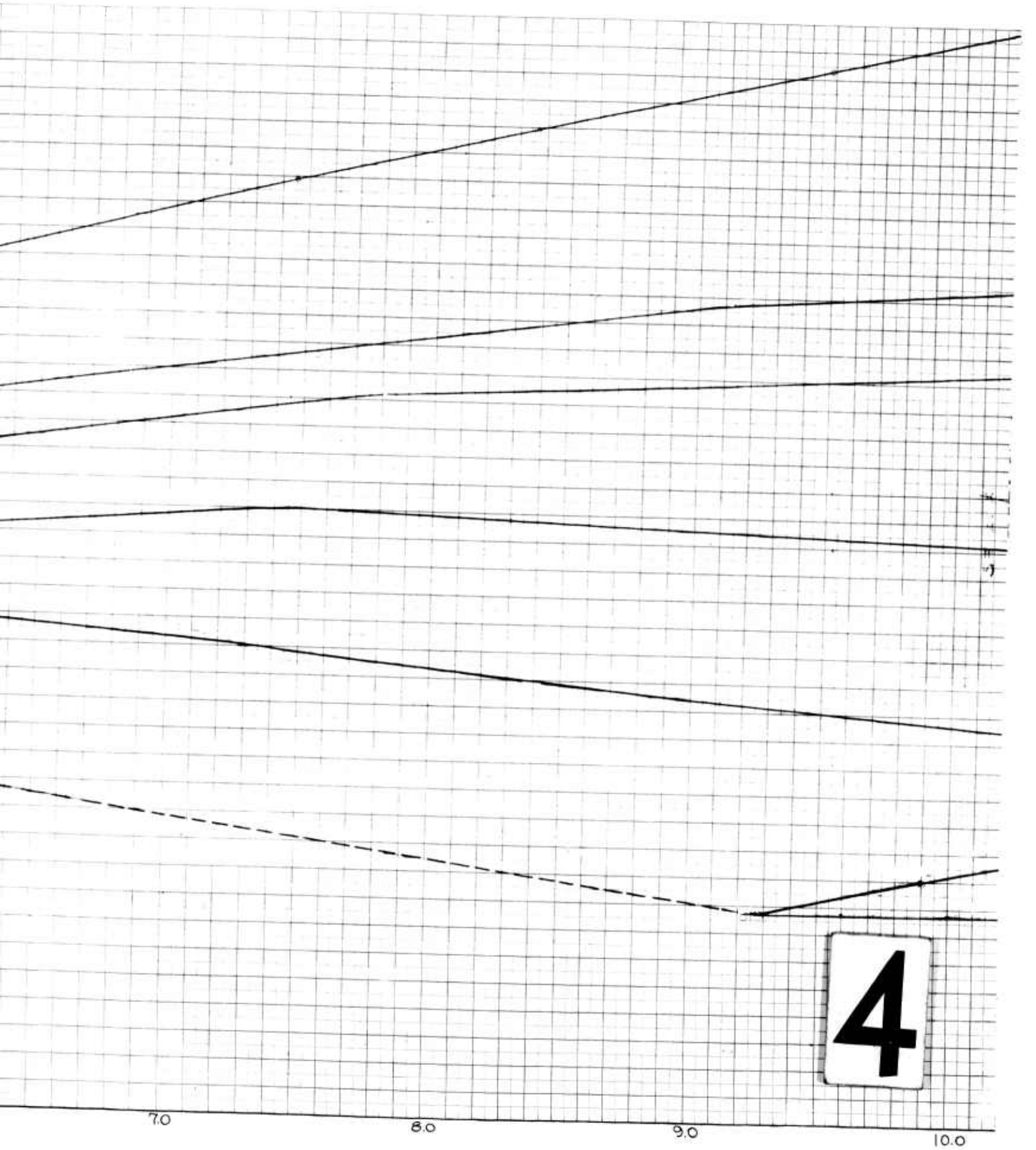
7.0
8.0
9.0
10.0
4

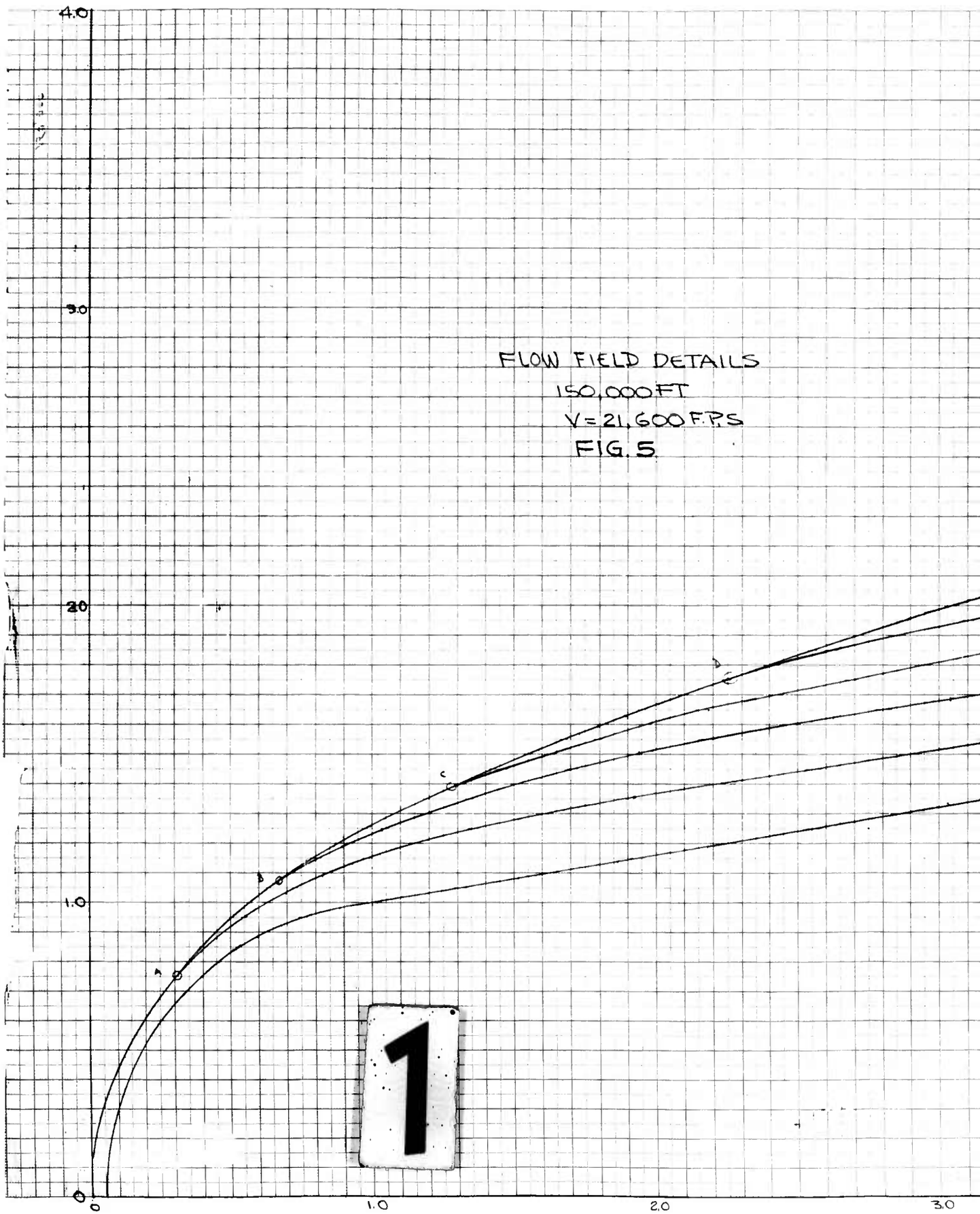
4.0
3.0
2.0
1.0
0
0
1.0
2.0
3.0
FLOW FIELD DETAILS
150,000 FT
V = 21,600 F.P.S
FIG. 5
1

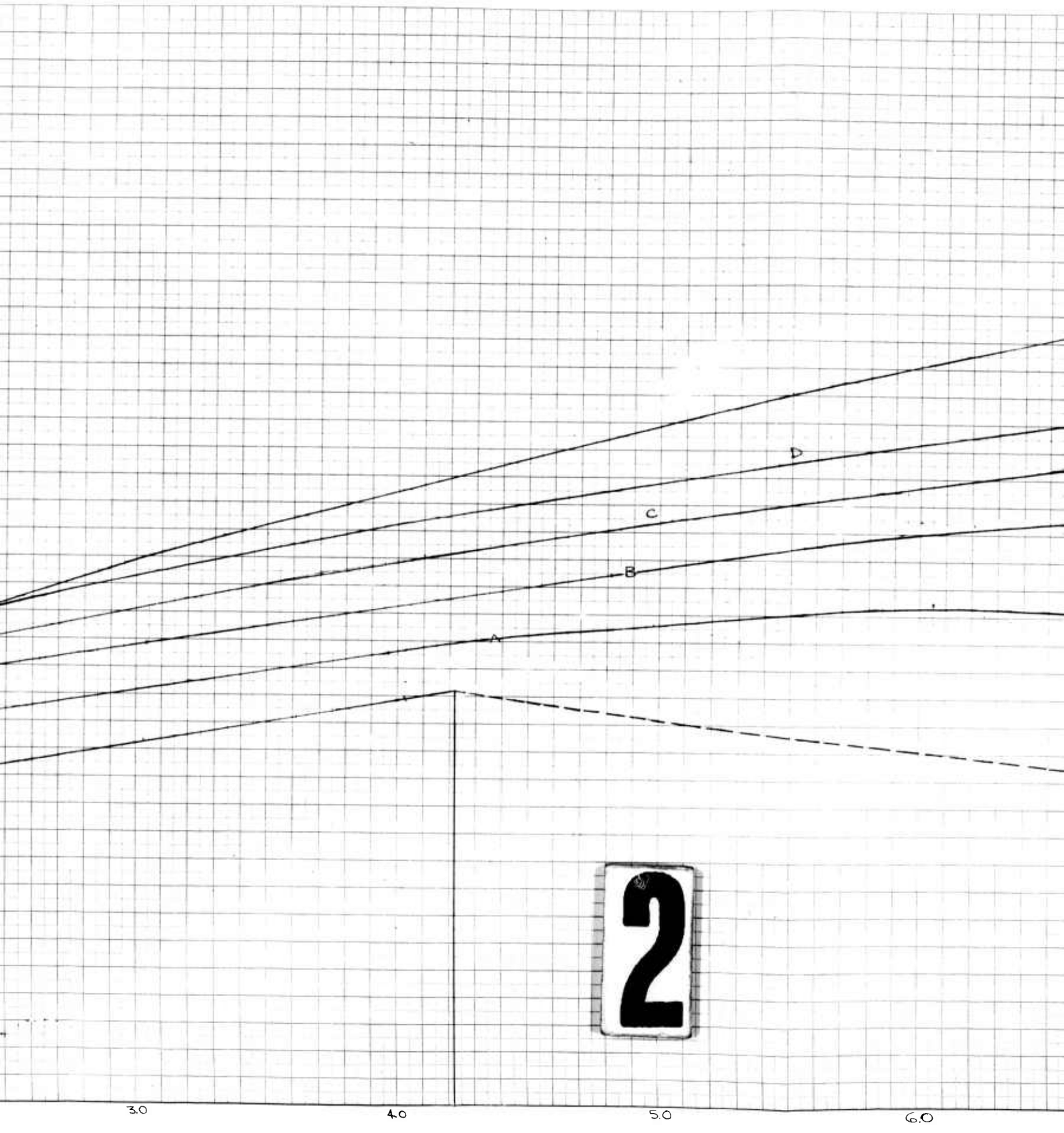
D
C
B
A
2
3.0
4.0
5.0
6.0

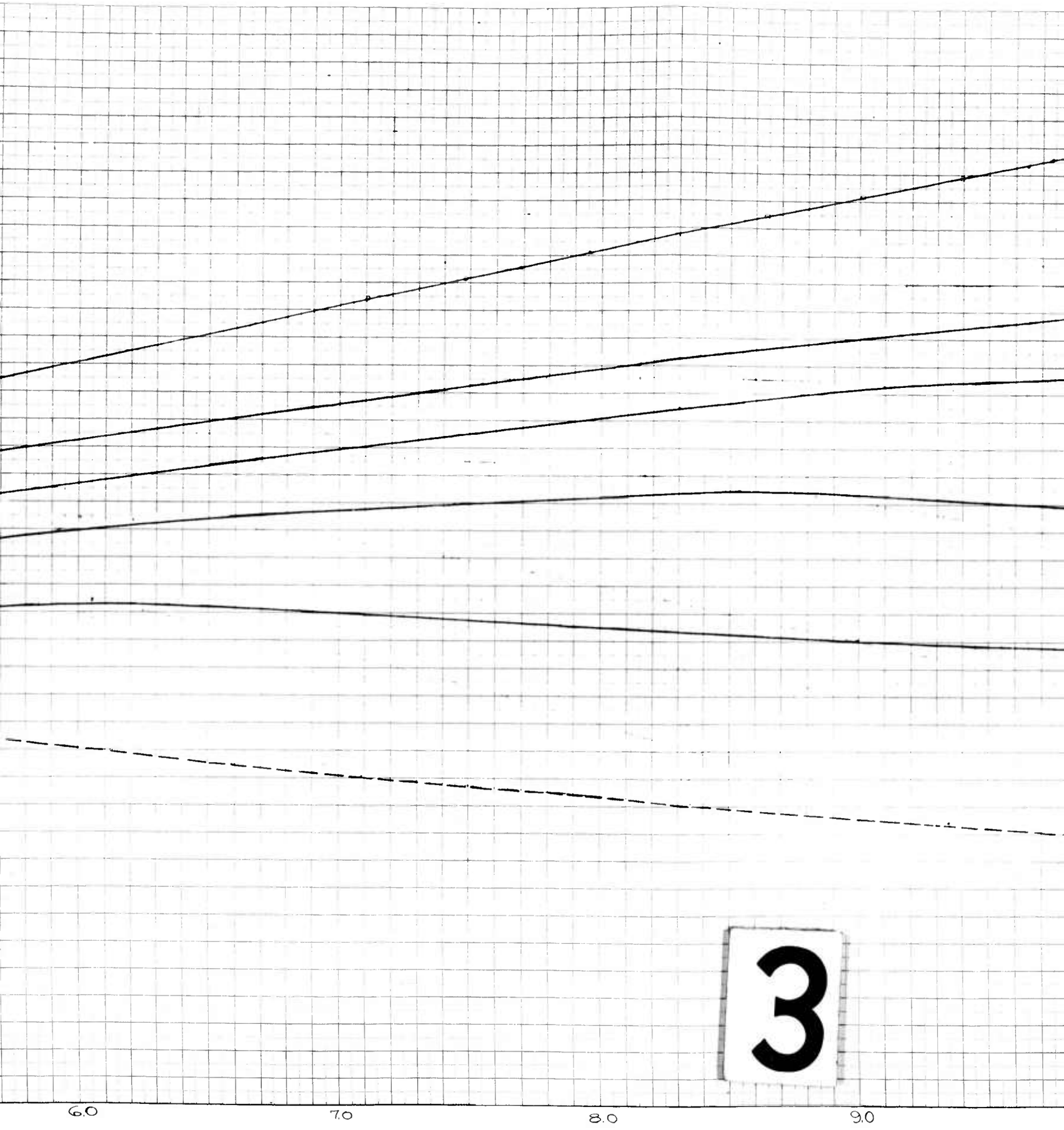
3
6.0
7.0
8.0
9.0

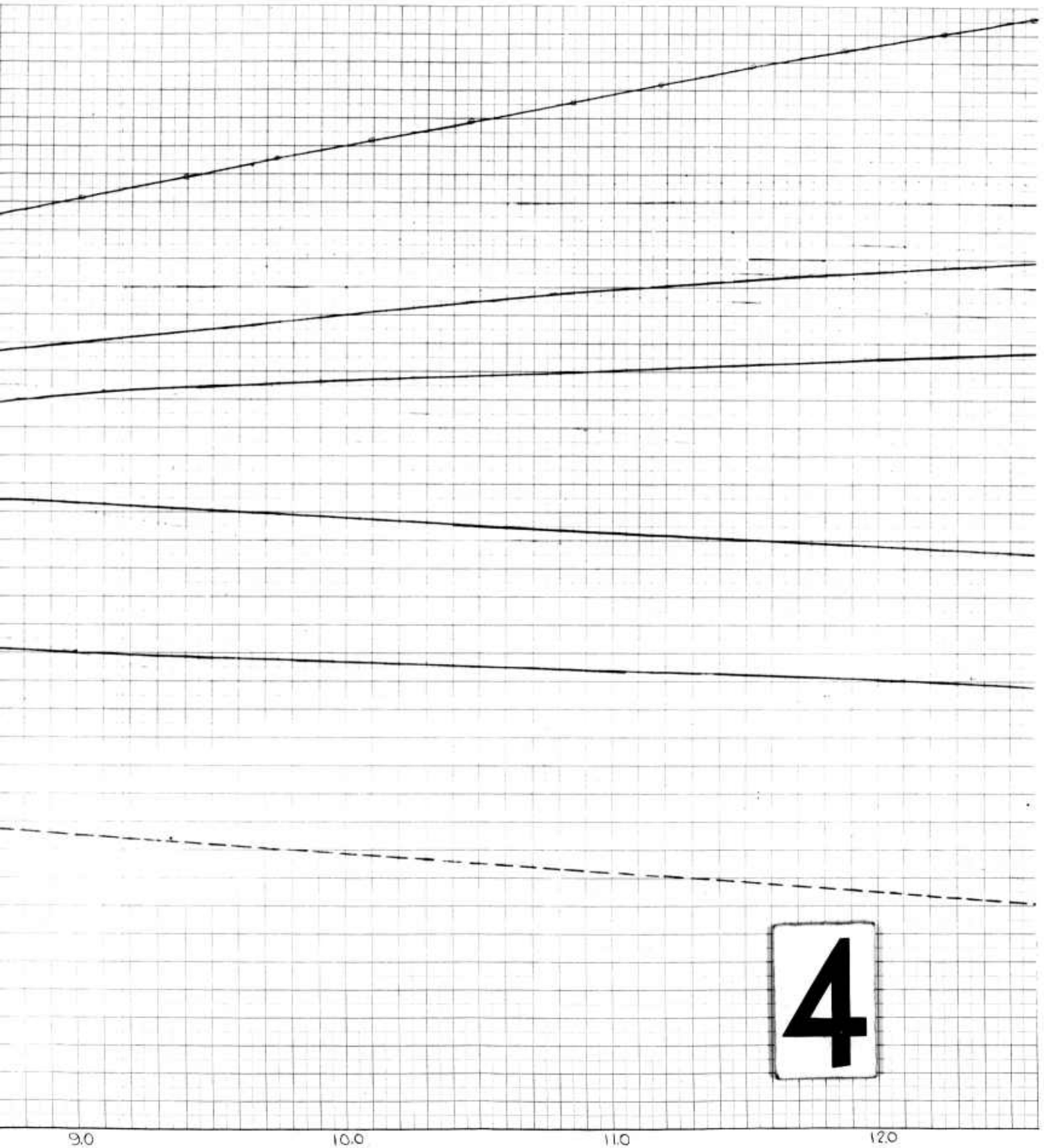

FIG. 5

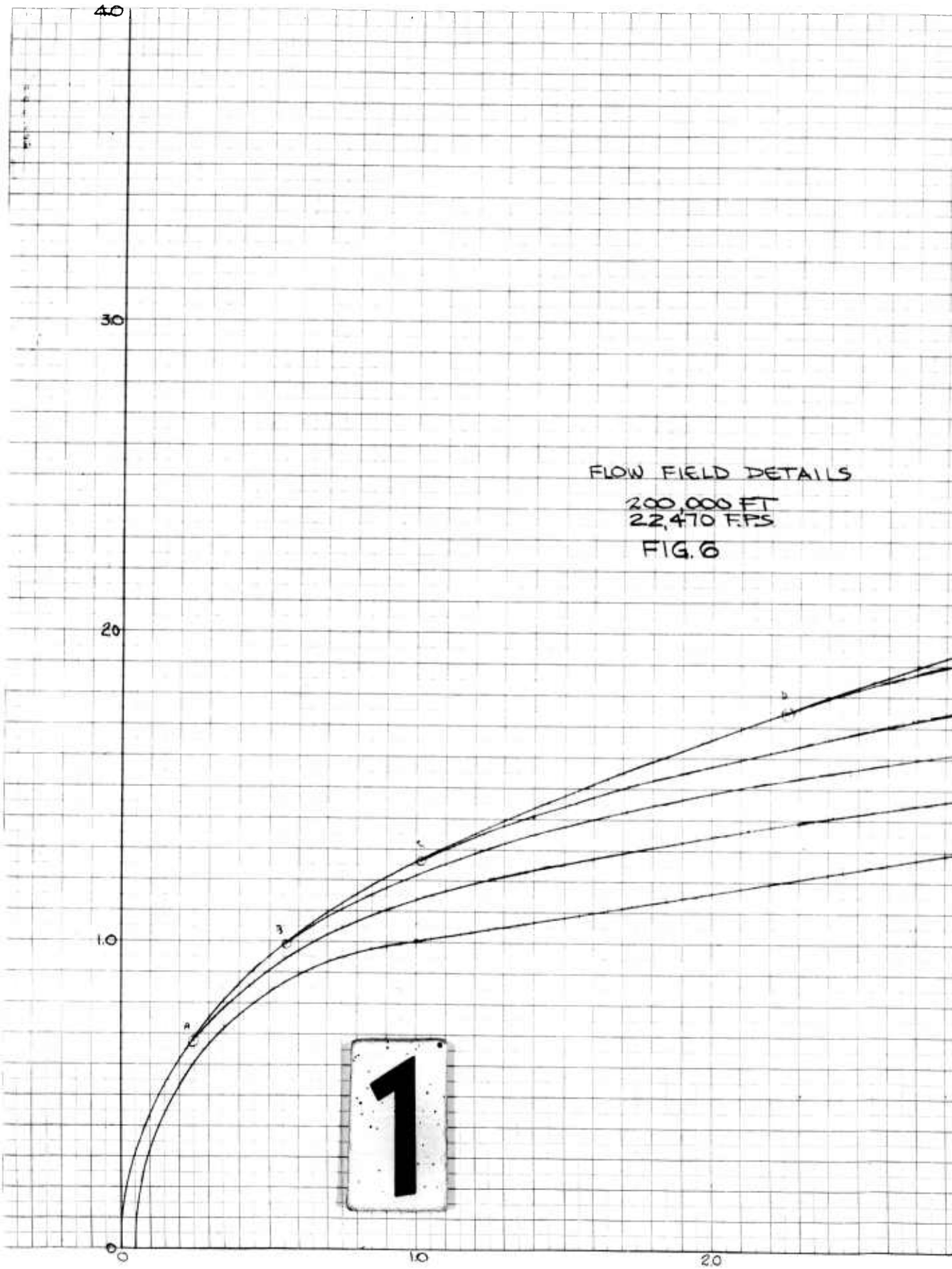

FLOW FIELD DETAILS

200,000 FT
22,470 F.P.S

FIG. 6

ELD DETAILS
000 FT
70 F.P.S
.6

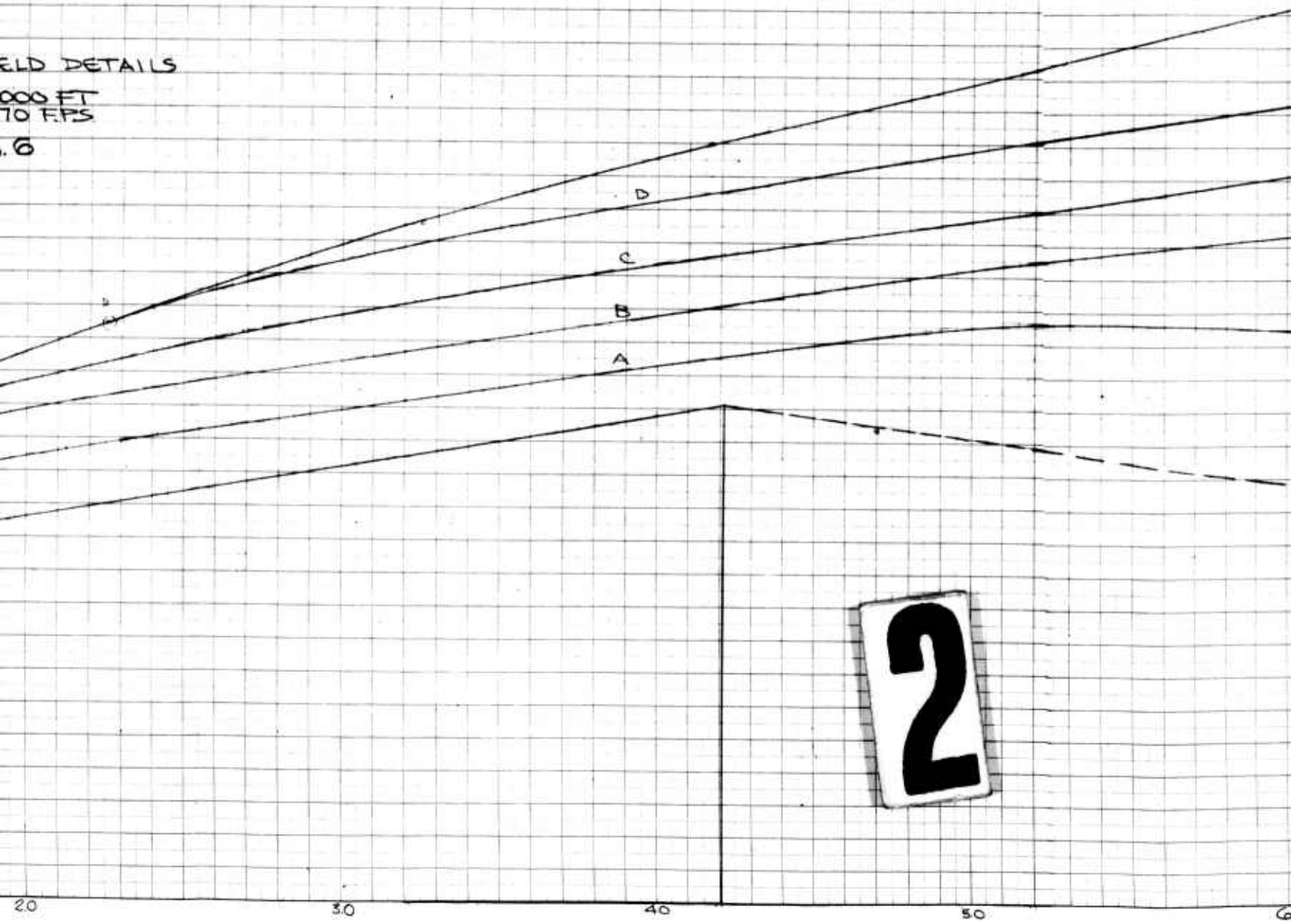

2

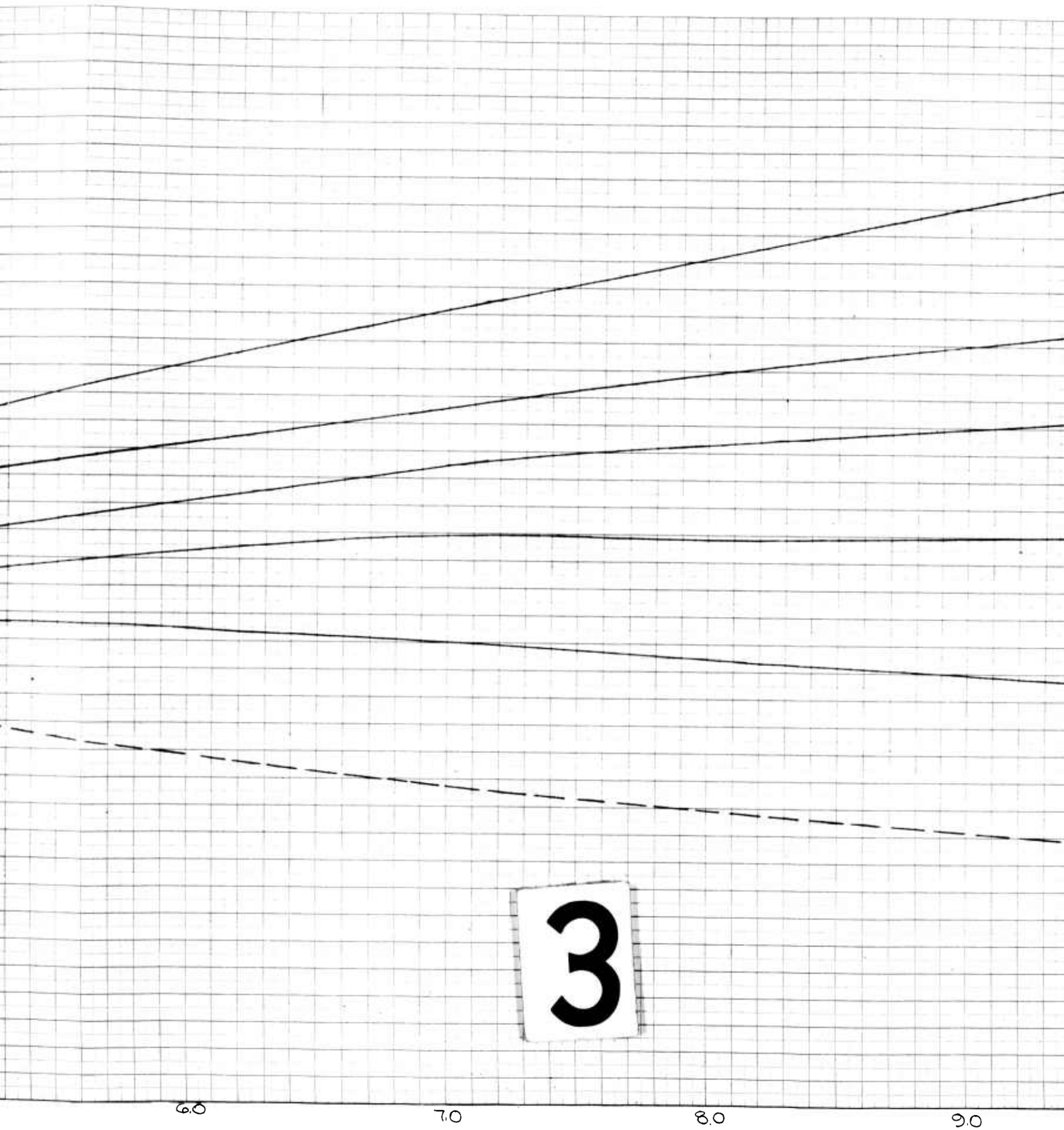
3
6.0
7.0
8.0
9.0

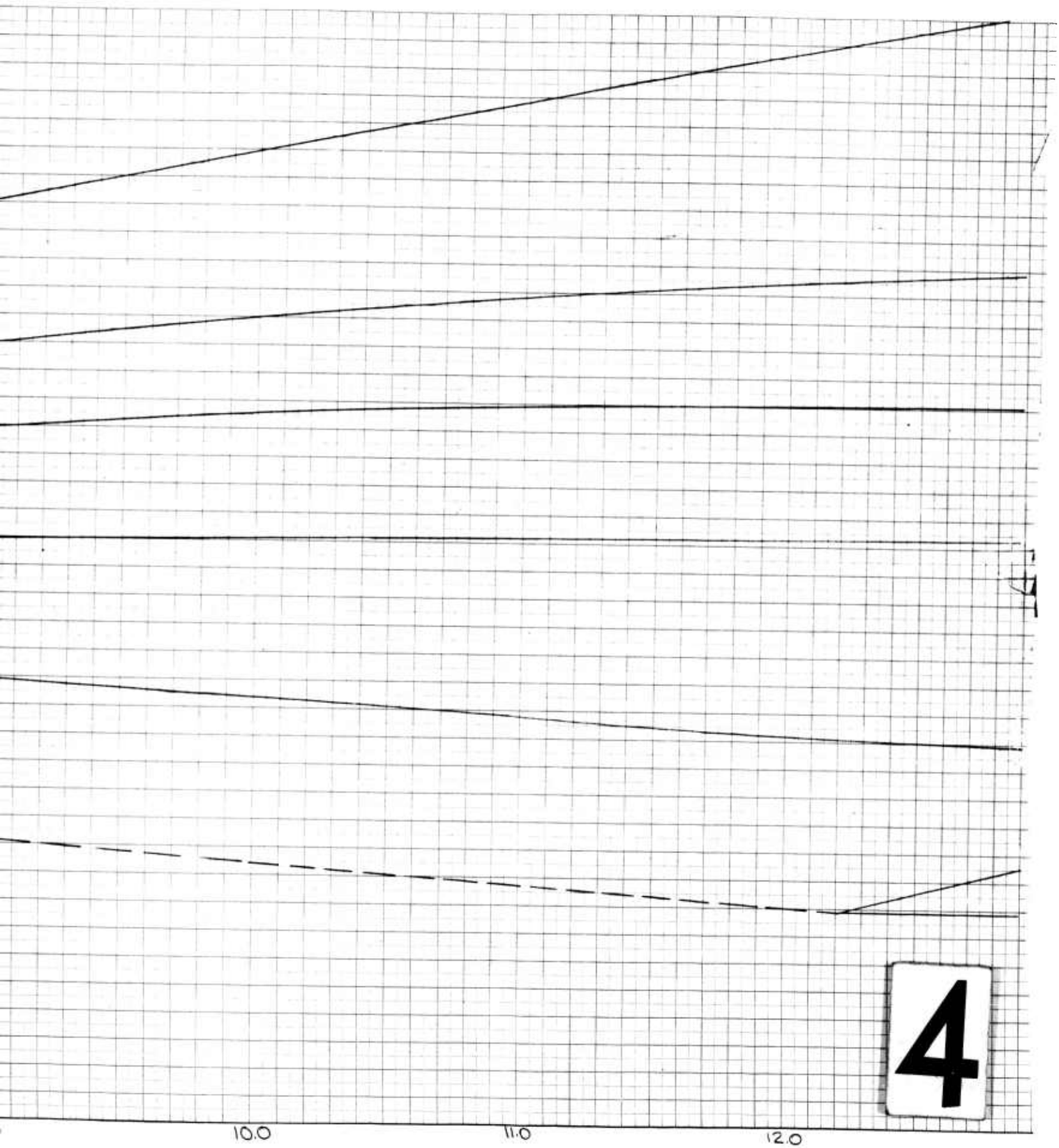
10.0
11.0
12.0
4

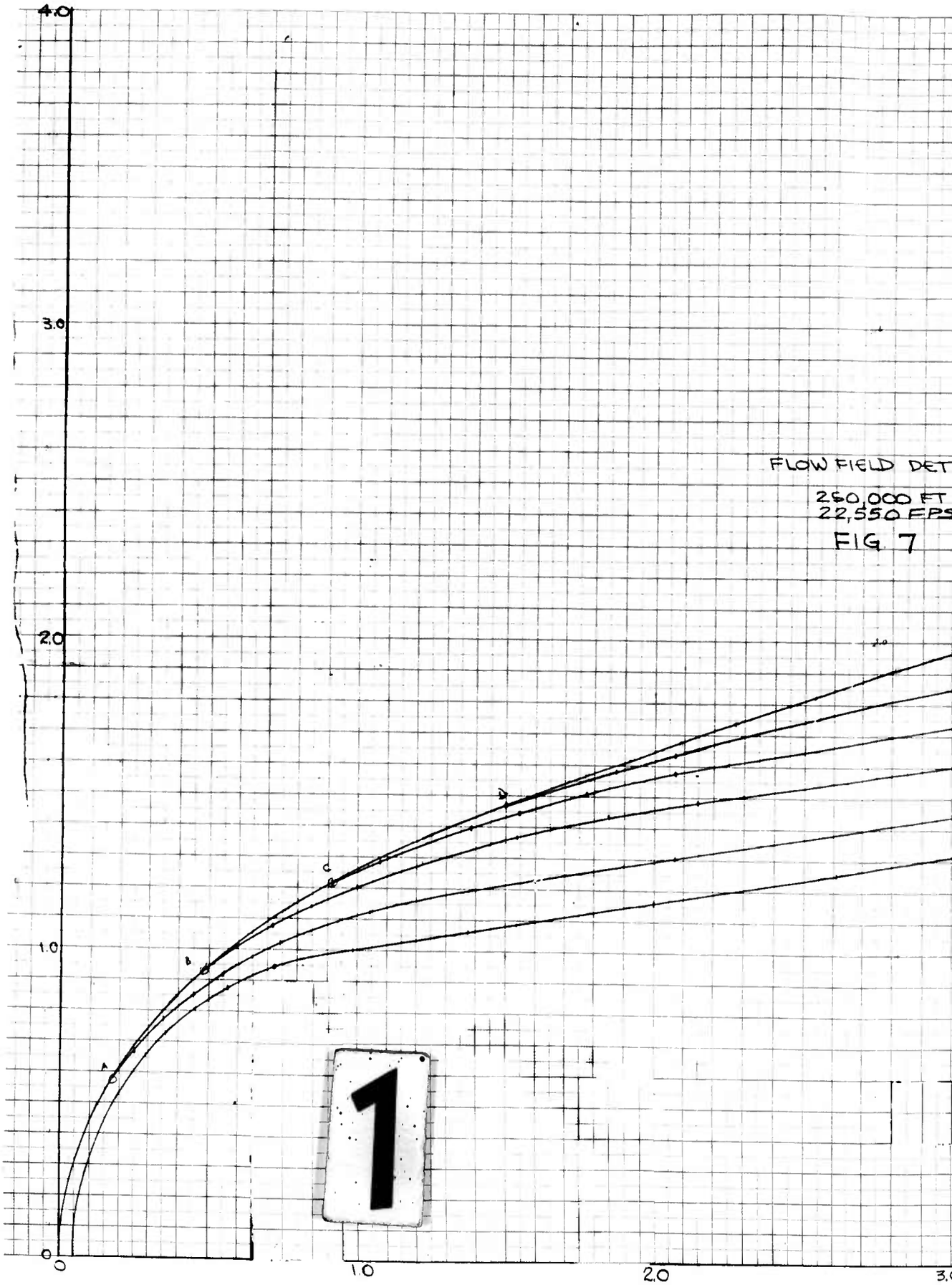
4.0
3.0
2.0
1.0
0
1.0
2.0
A
B
C
D
FLOW FIELD DET
250,000 FT
22,550 FPS
FIG 7
1

LD DETAILS

000 FT
50 FPS

G. 7

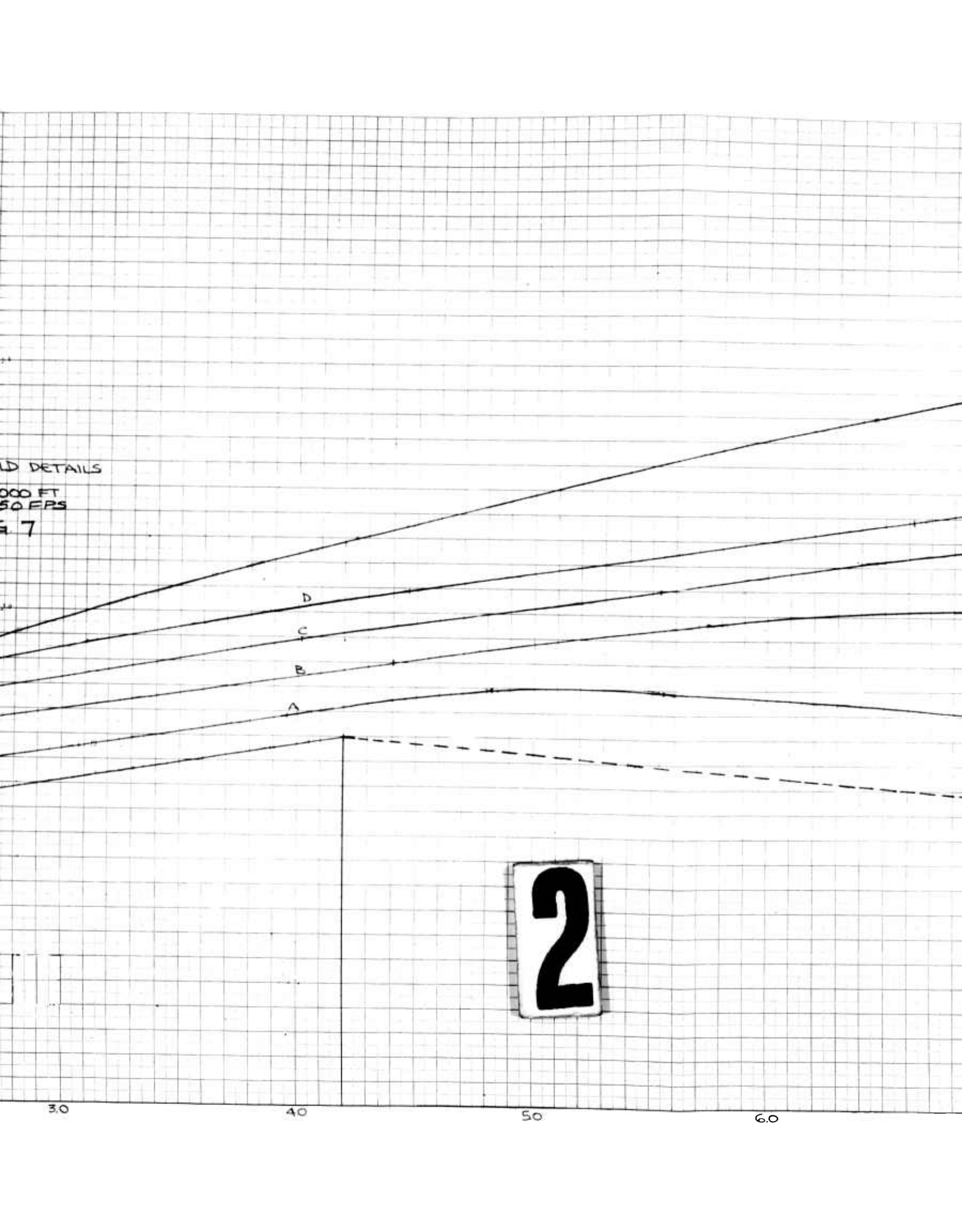

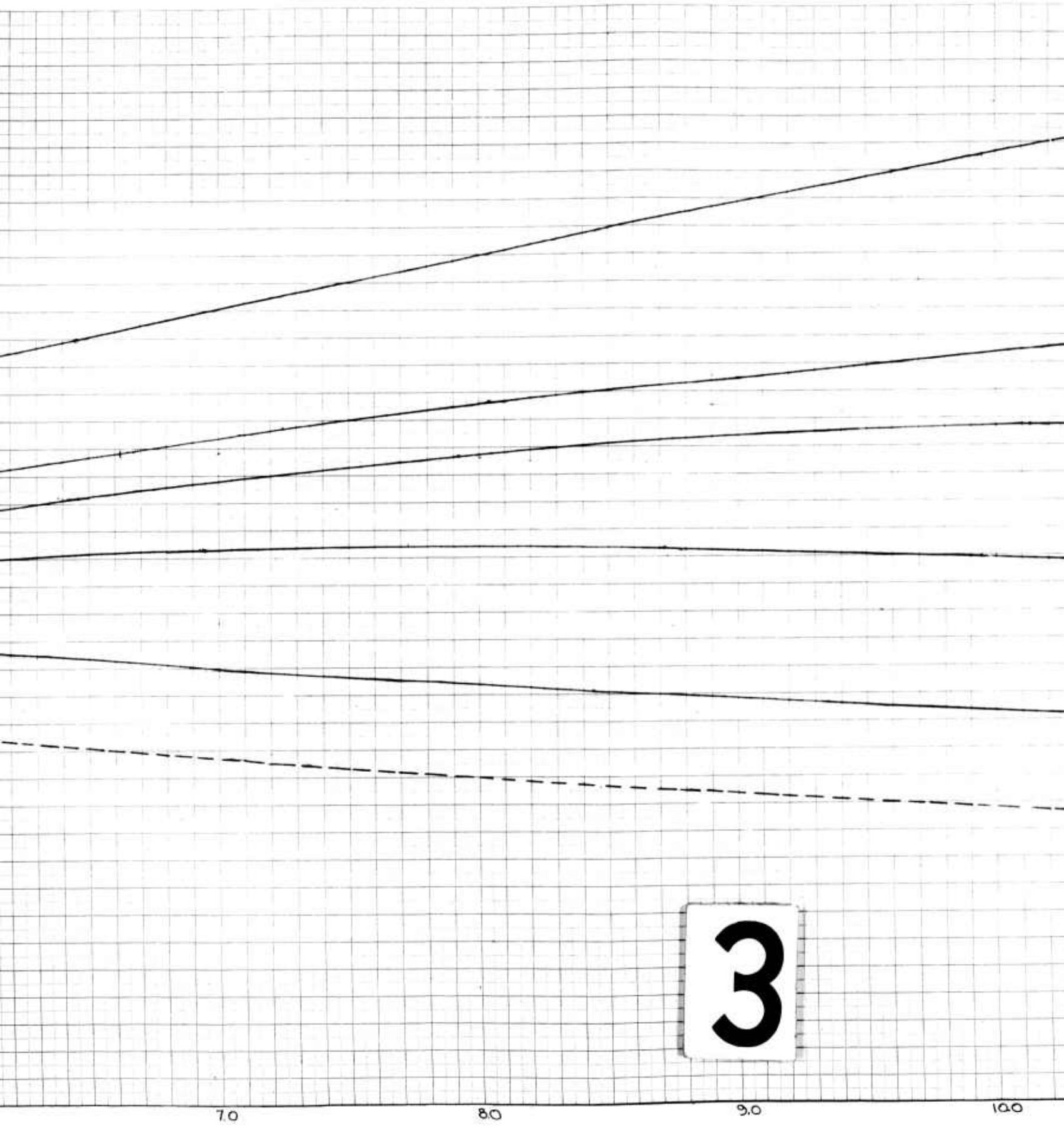
3
7.0
8.0
9.0
10.0

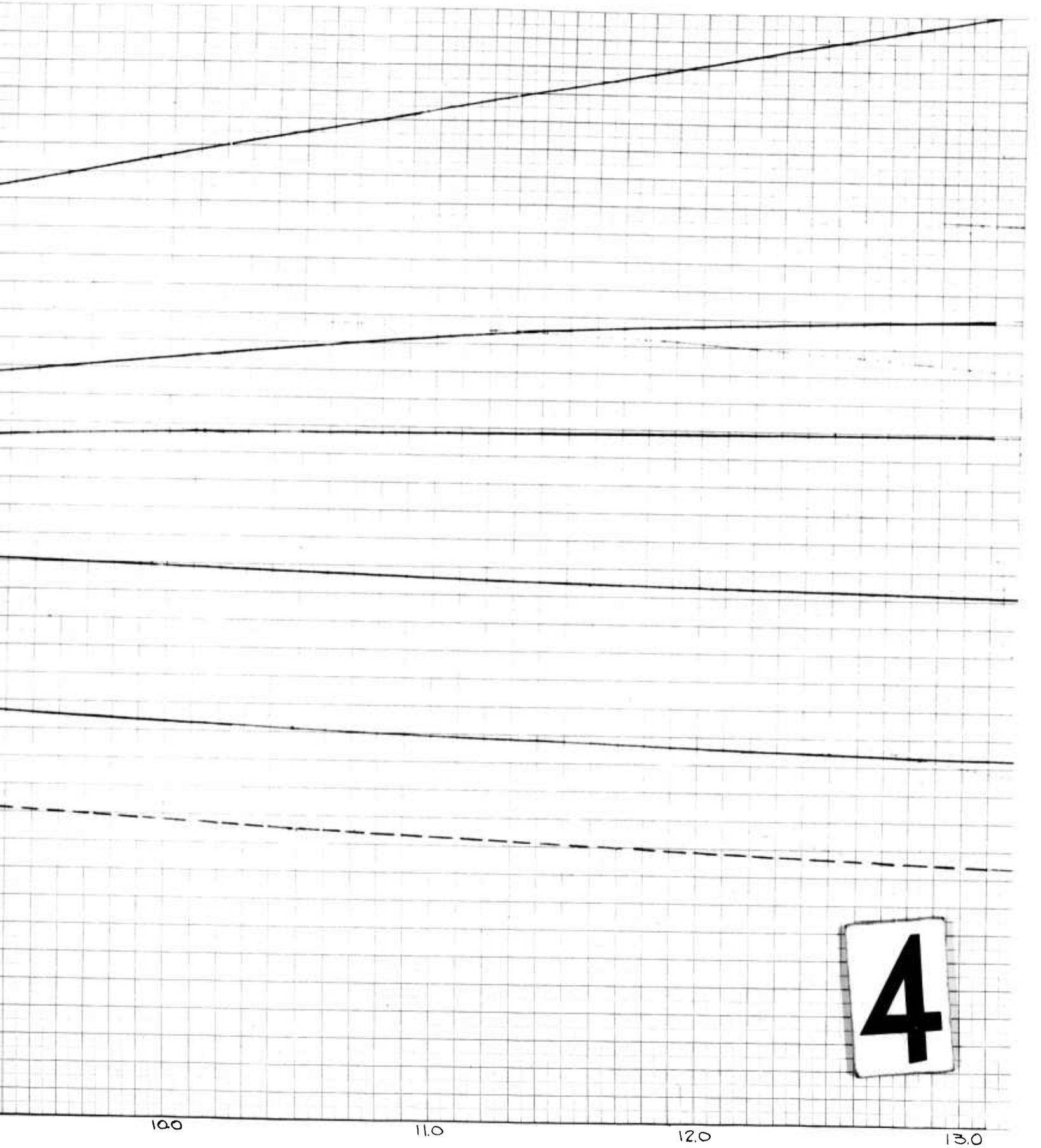
10.0
11.0
12.0
13.0
4

Figure 8a.
Electron Density Distribution Across Shock Layer
at Axial Station 1.5

80,000 Ft. (Frozen)

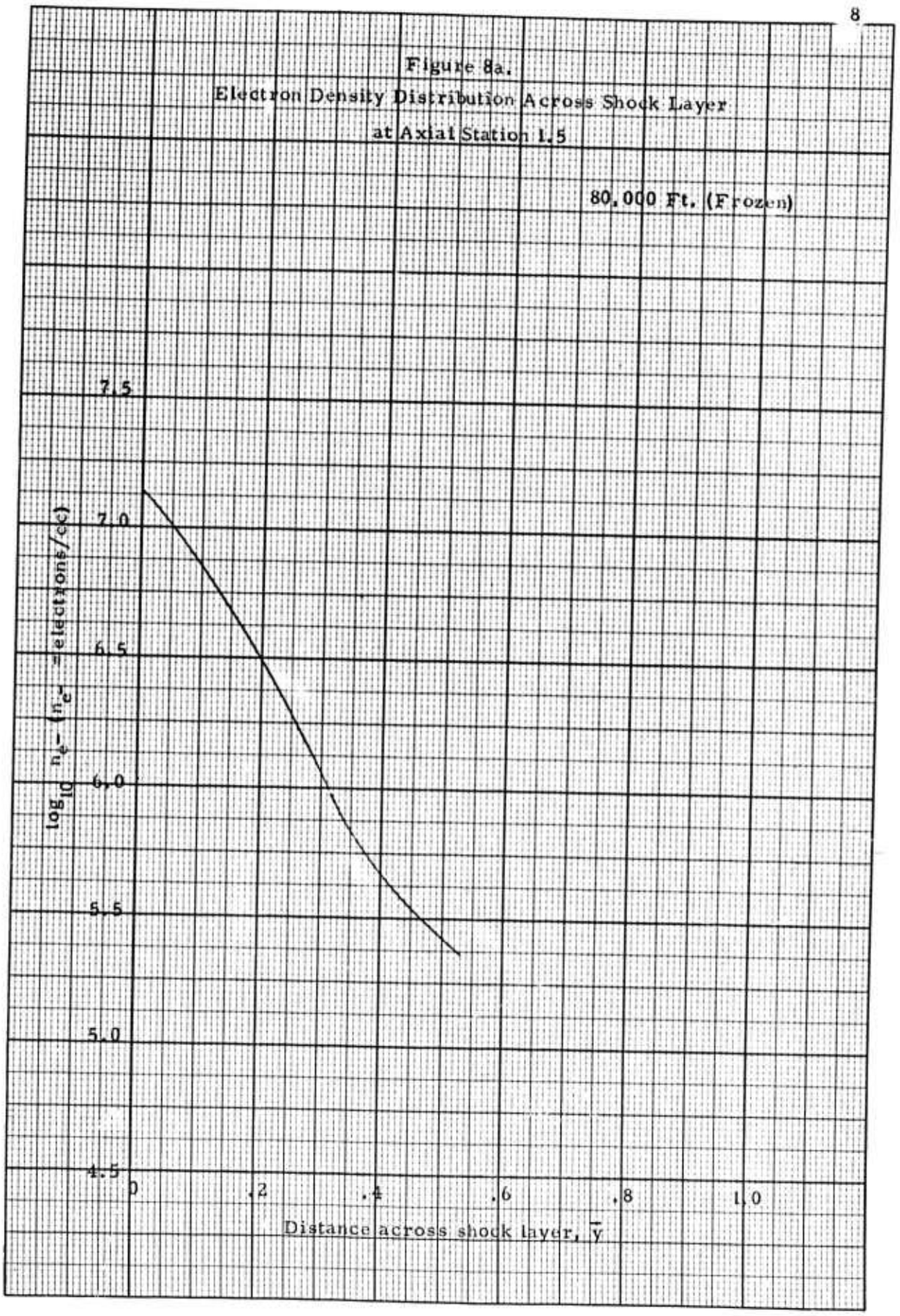

Figure 8b.
Electron Density Distribution Across Shock Layer
at Axial Station 1.5

100,000 Ft. (Equilibrium)

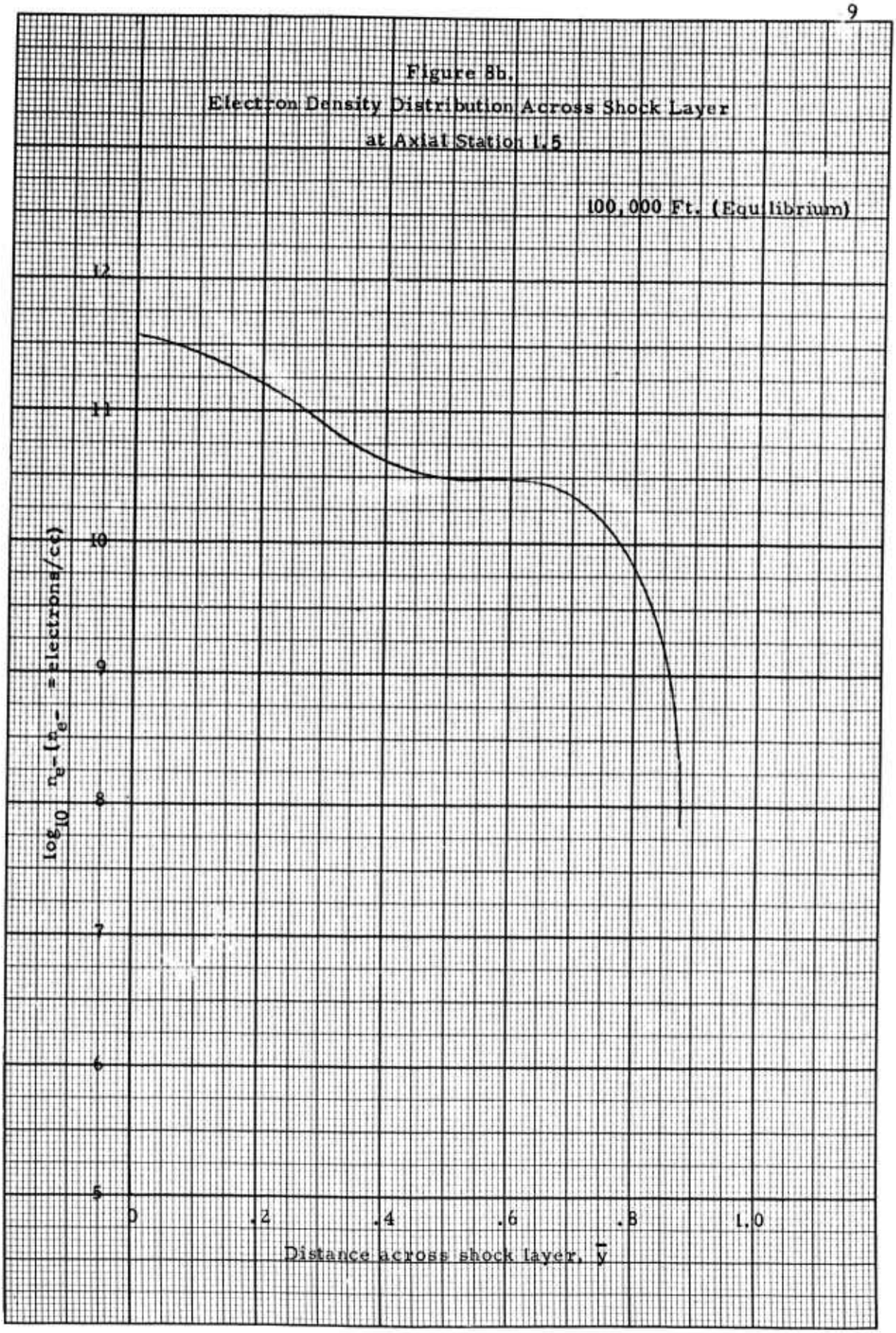

Figure 8c.
Electron Density Distribution Across Shock Layer
at Axial Station 1.5

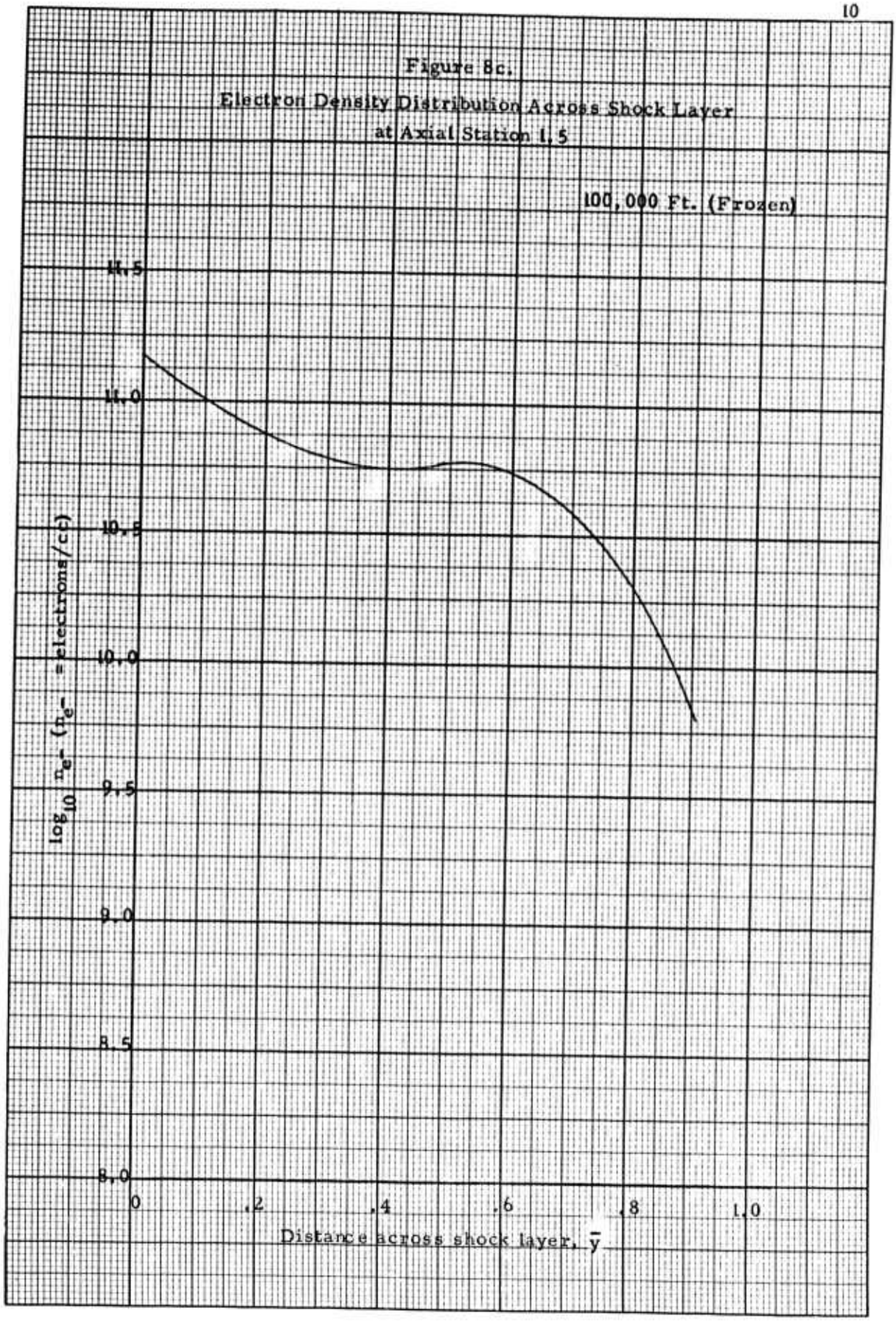

Figure 8d.
Electron Density Distribution Across Shock Layer
at Axial Station 1.5

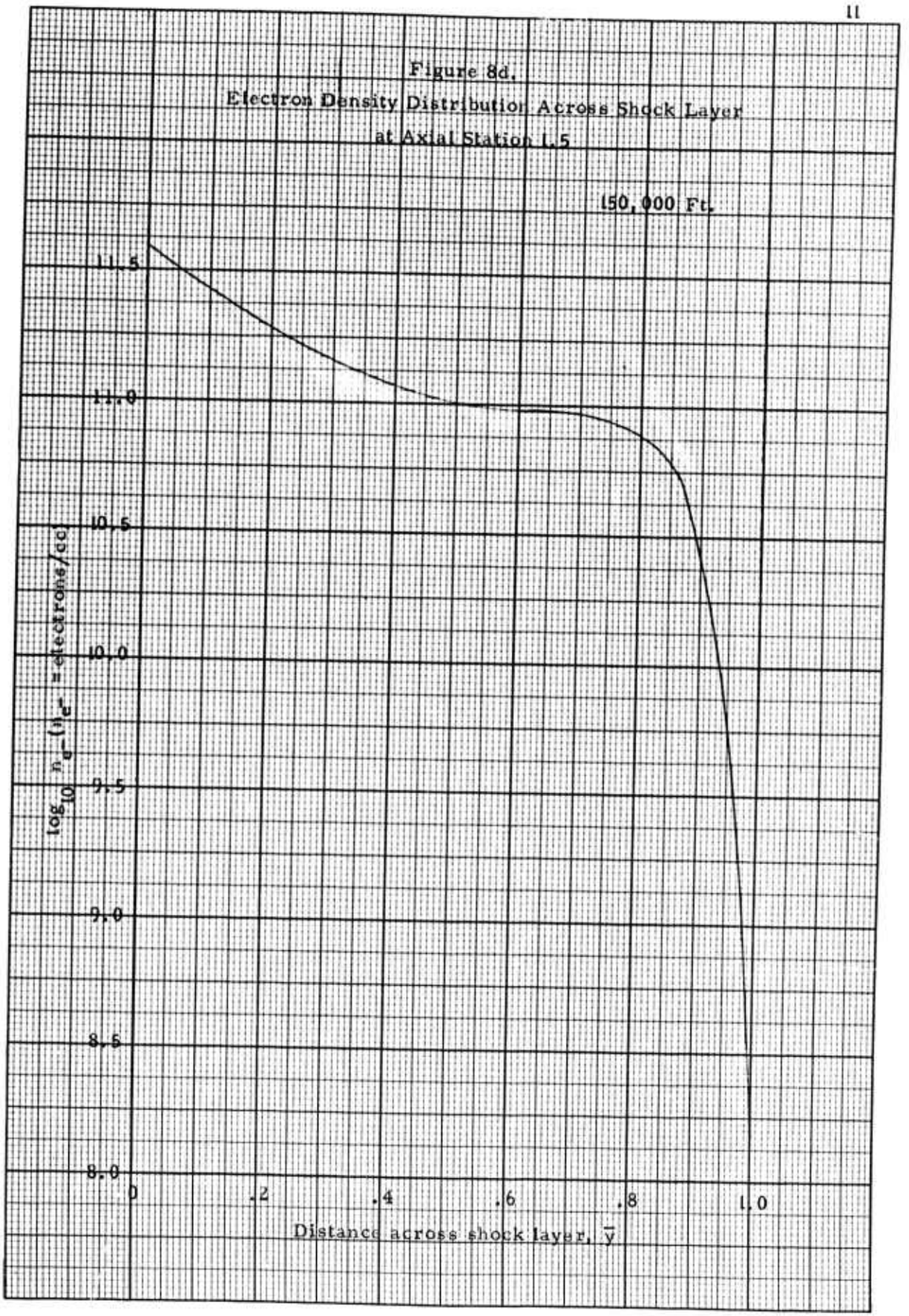

Figure 8e.

Electron Density Distribution Across Shock Layer
at Axial Station 1.5

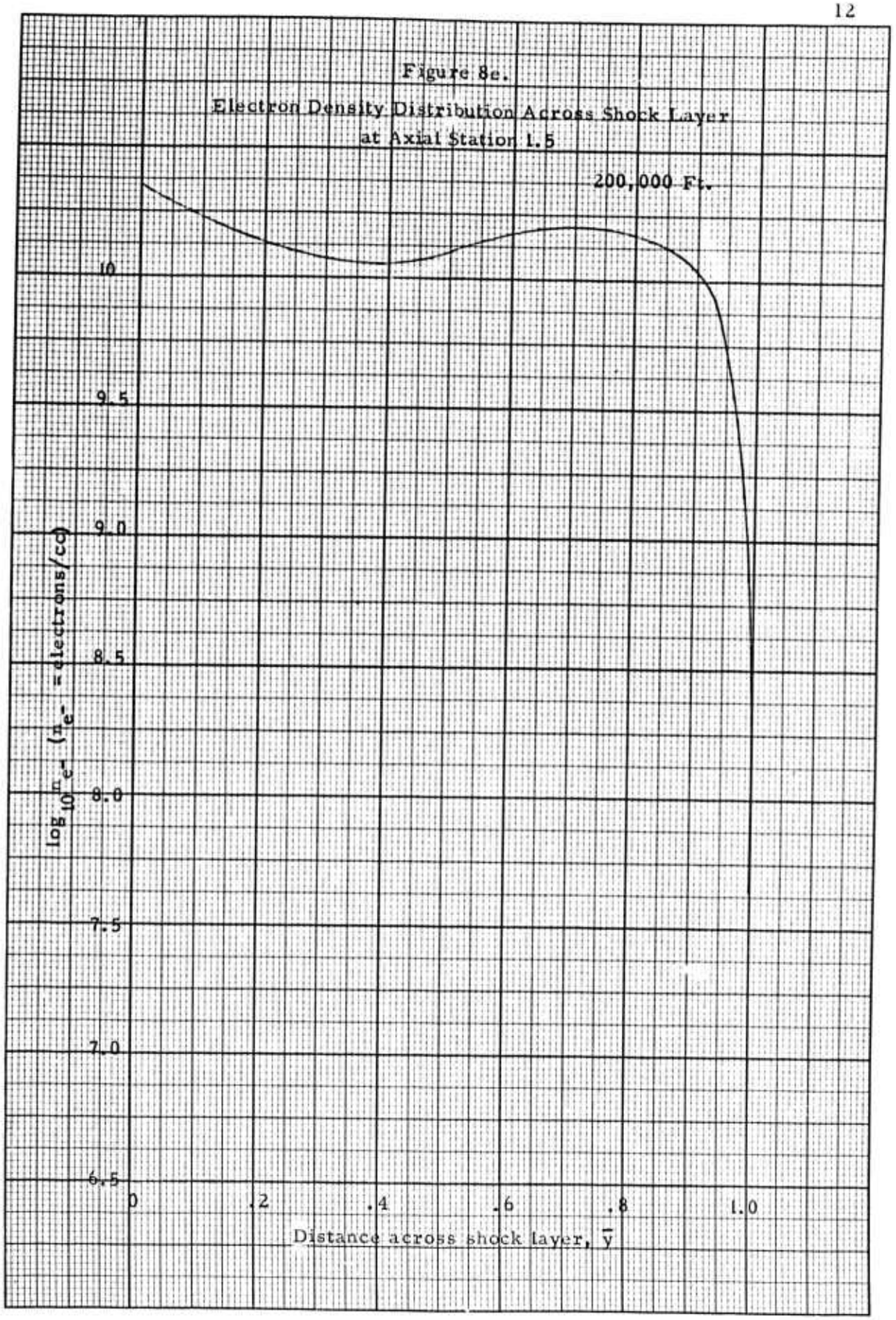

Figure 84.
Electron Density Distribution Across Shock Layer
at Axial Station 1.5

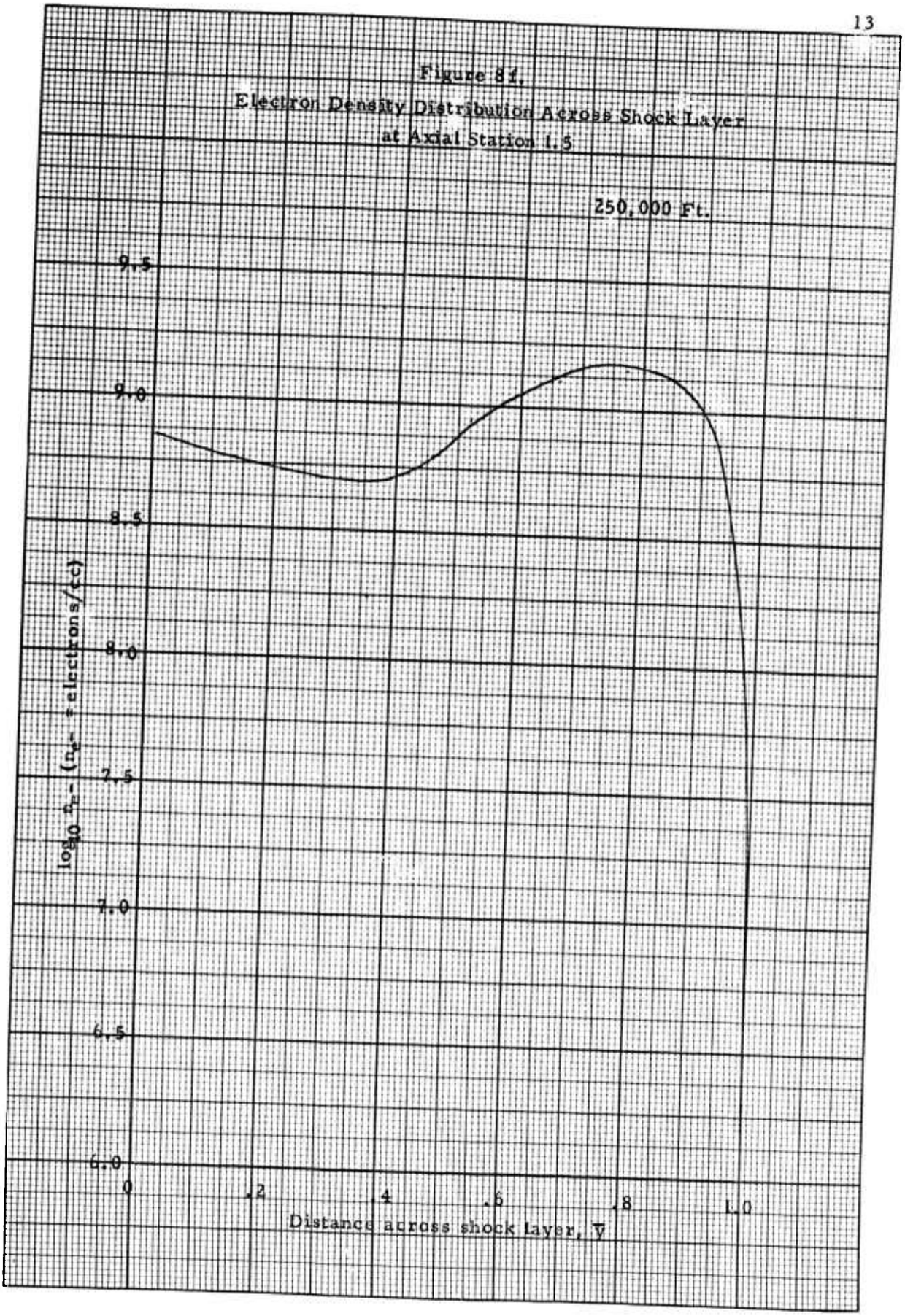

Figure 9a.
Pressure Ratio Across Shock Layer
at Axial Station 1.5

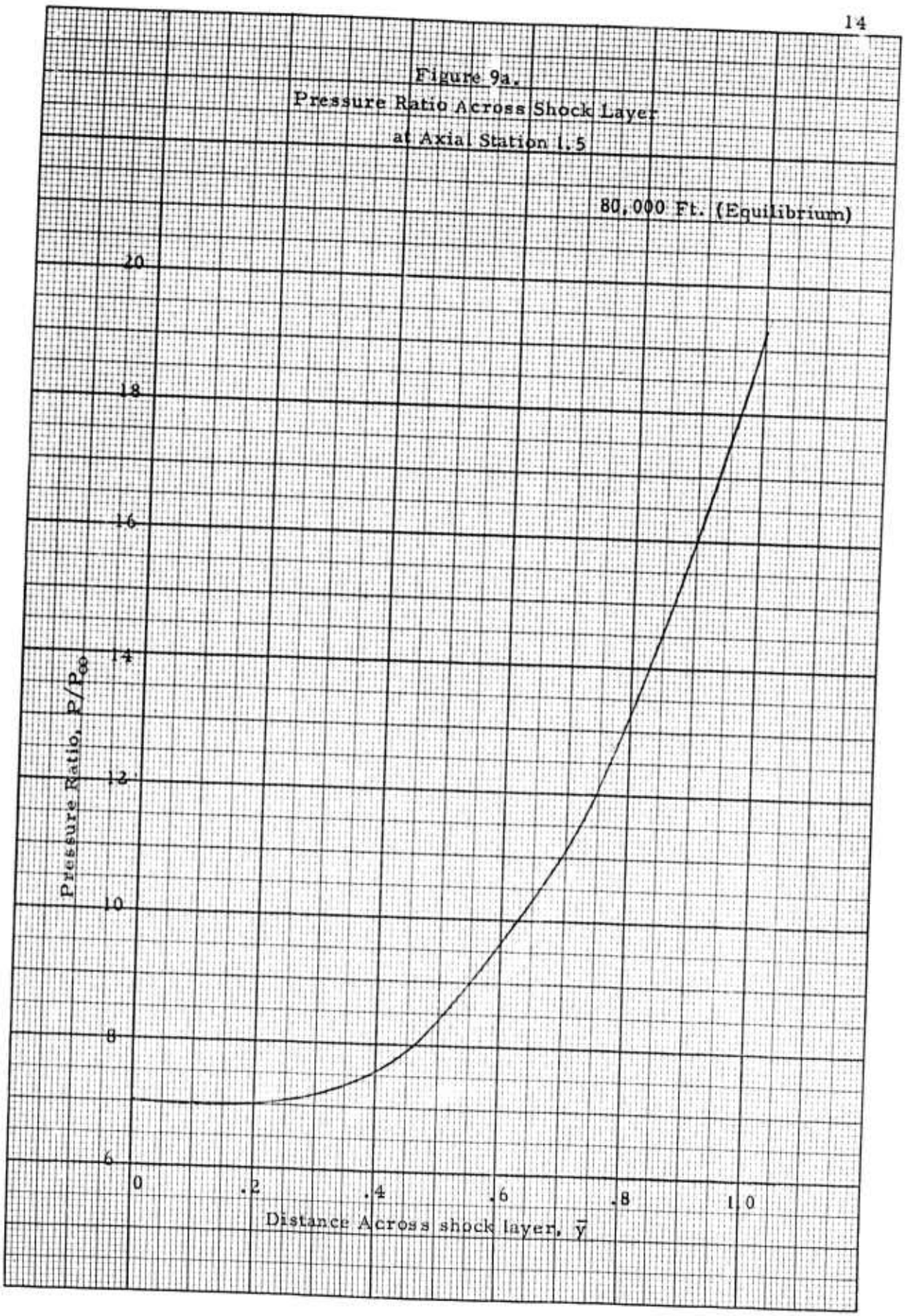

Figure 9b.
Pressure Ratio Across Shock Layer
at Axial Station 1.5

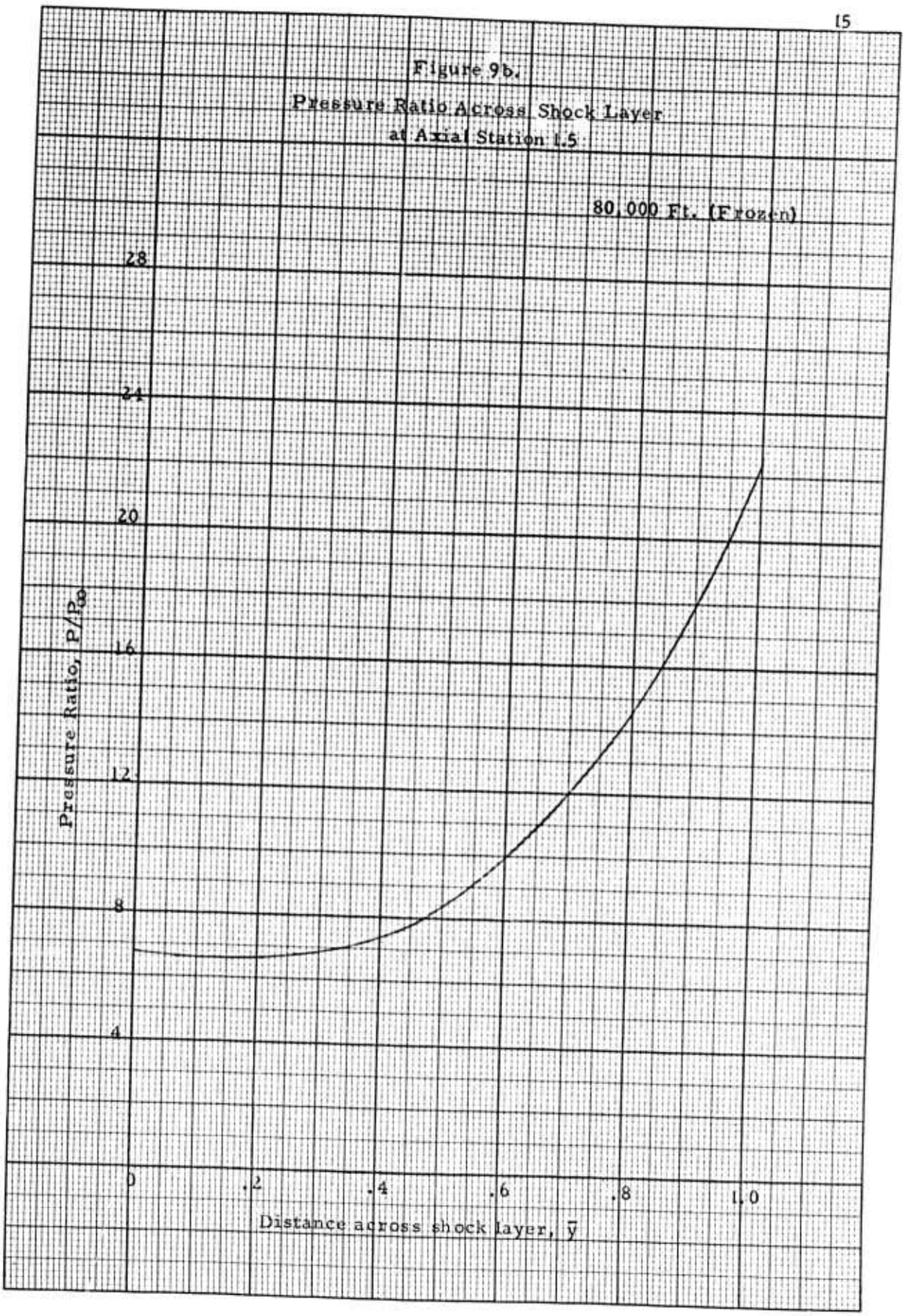

Figure 9c.

Pressure Ratio Across Shock Layer

at Axial Station L.5

100,000 Ft. (Equilibrium)

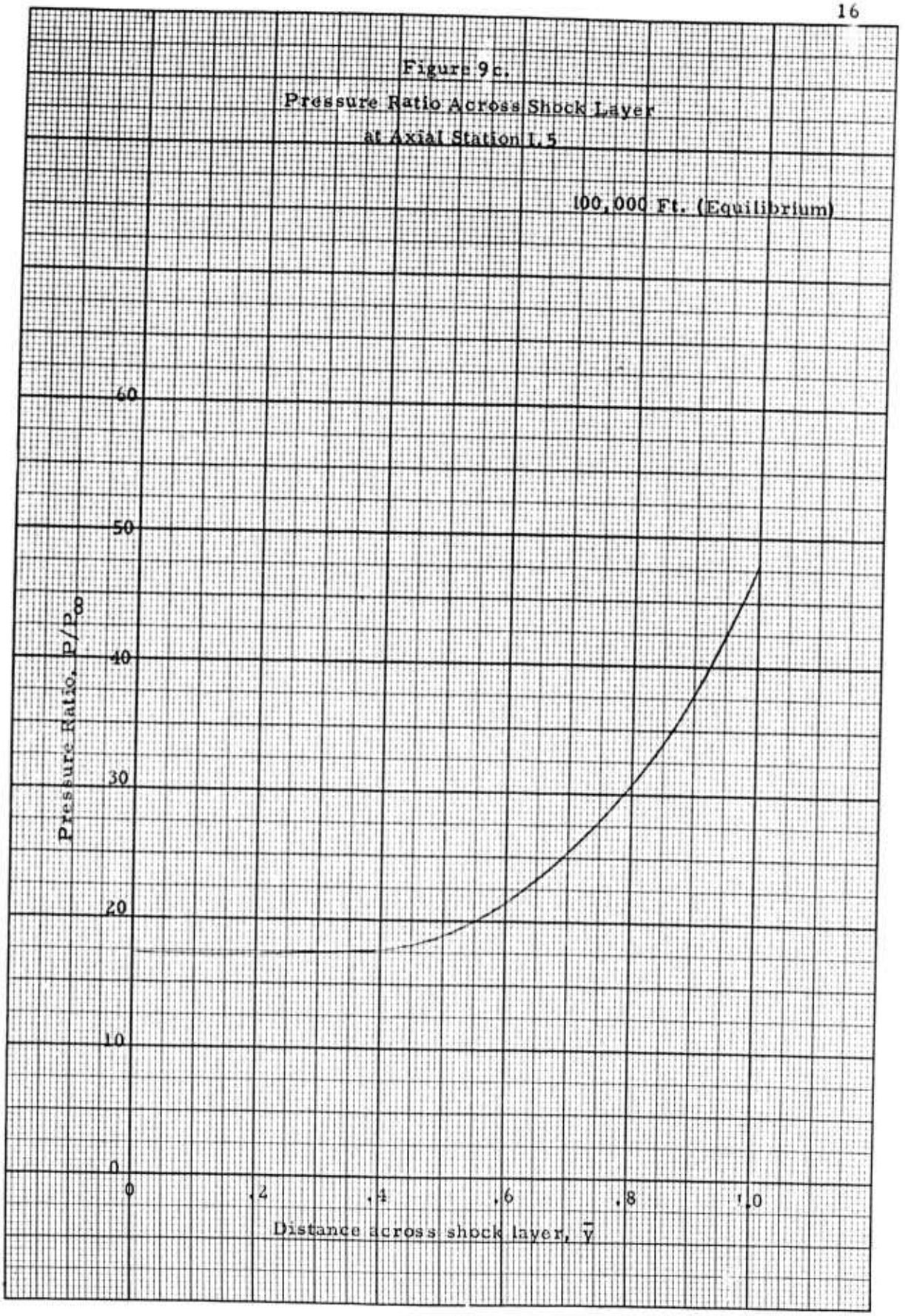

Figure 9d.
Pressure Ratio Across Shock Layer
at Axial Station 1.5
100,000 Ft. (Frozen)

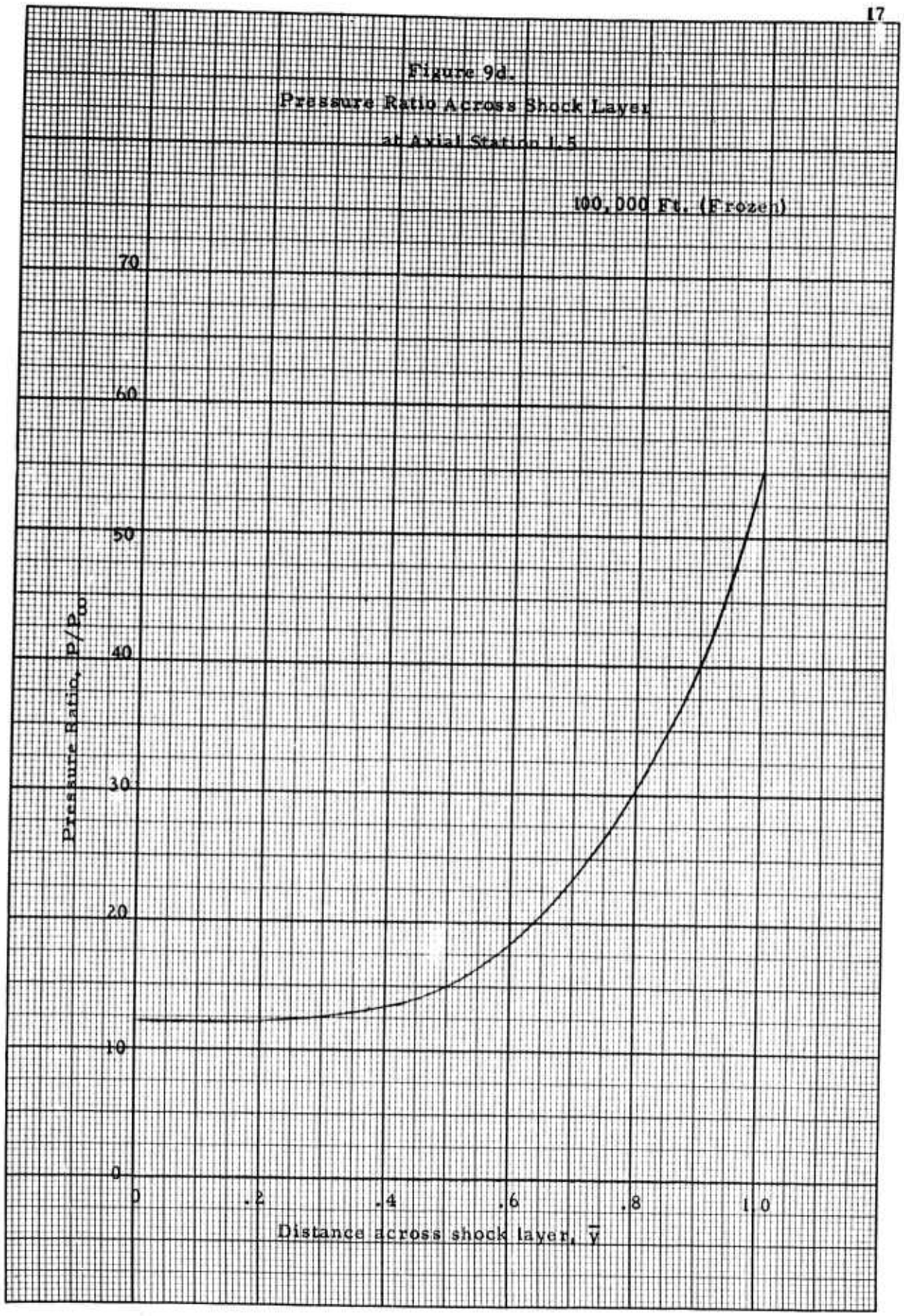

Figure 9e.
Pressure Ratio Across Shock Layer
at Axial Station 1.5

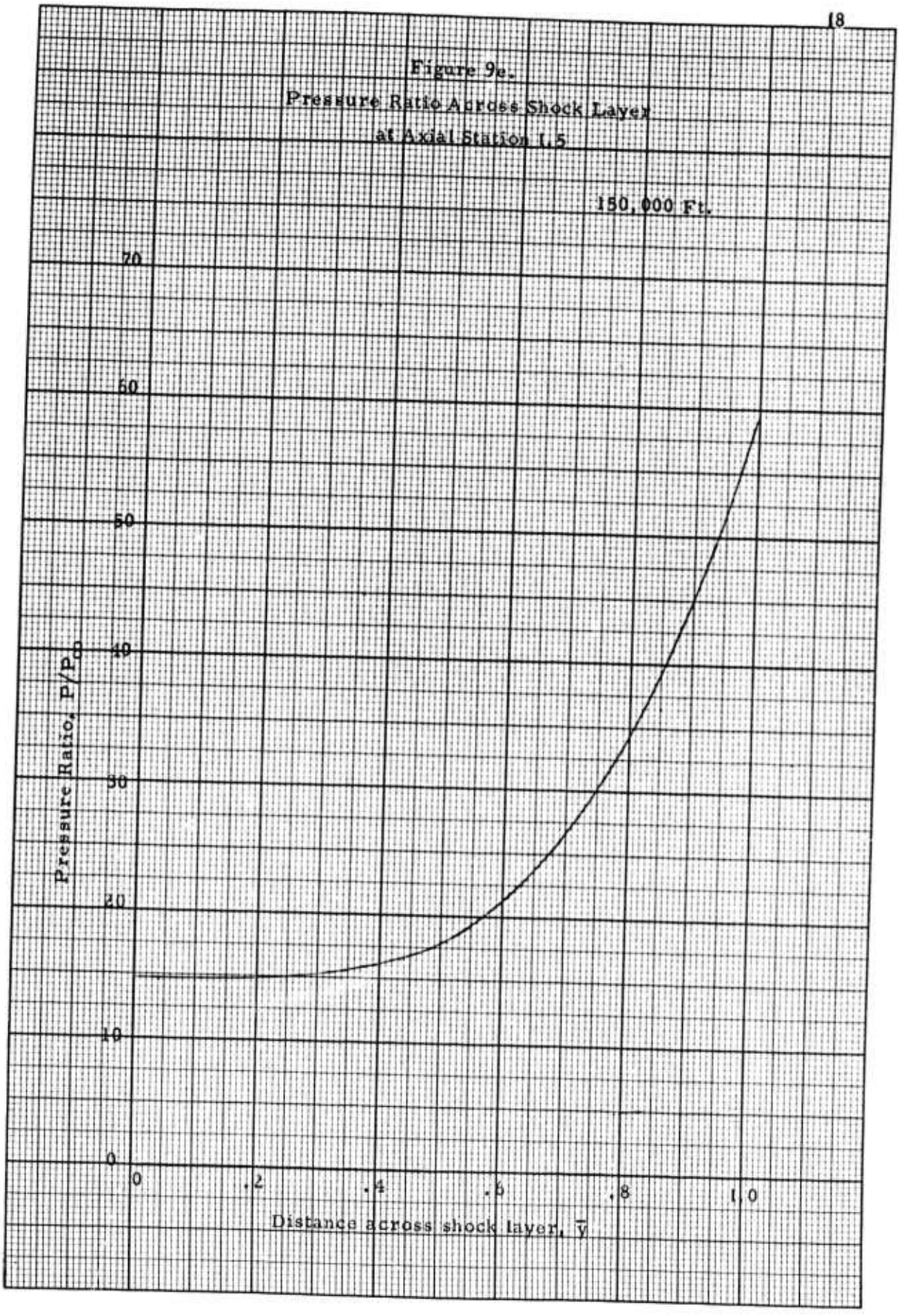

Figure 9f.
Pressure Ratio Across Shock Layer
at Axial Station 1.5

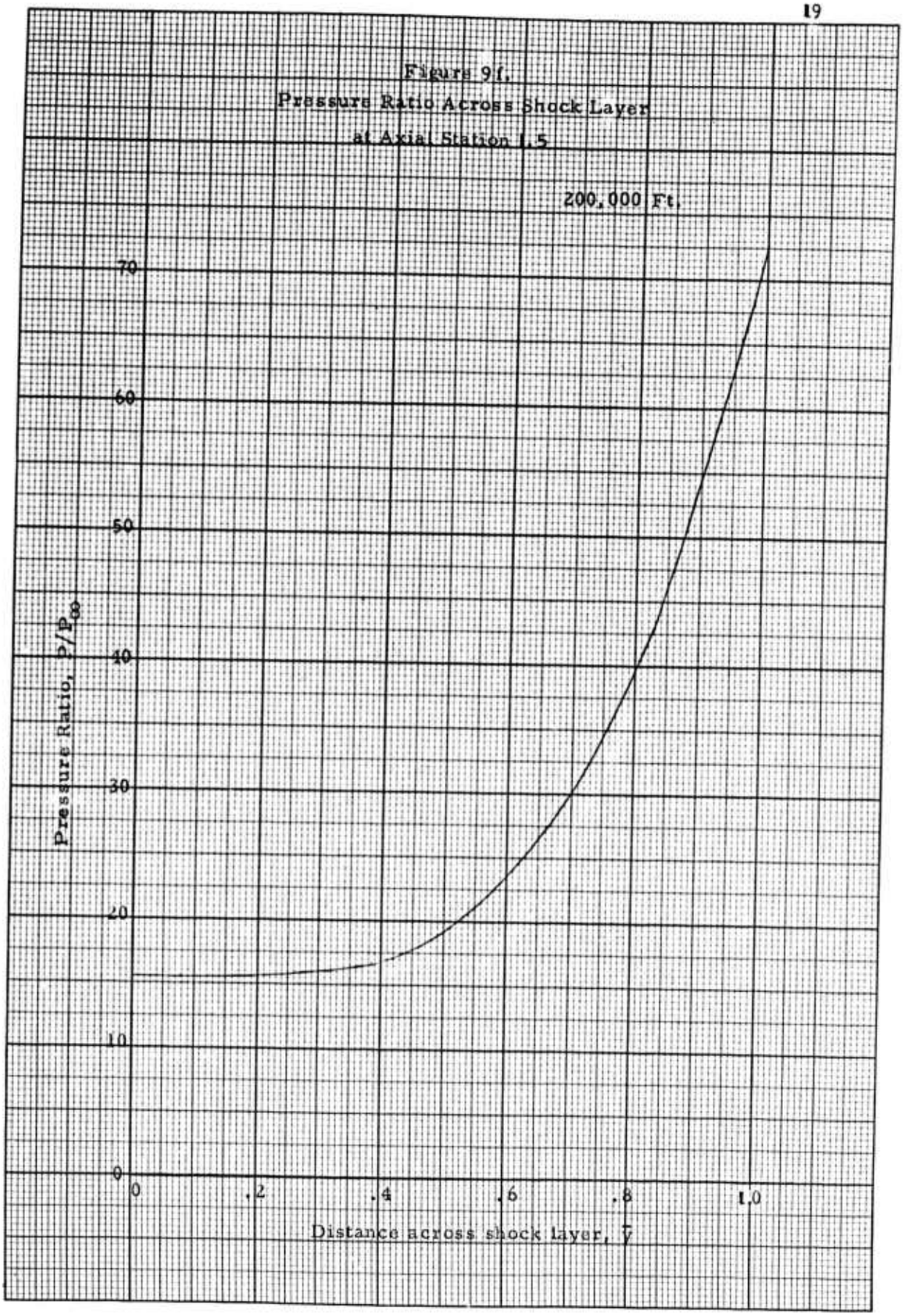

Figure 9 g.
Pressure Ratio Across Shock Layer
at Axial Station 1.5

250,000 Ft.

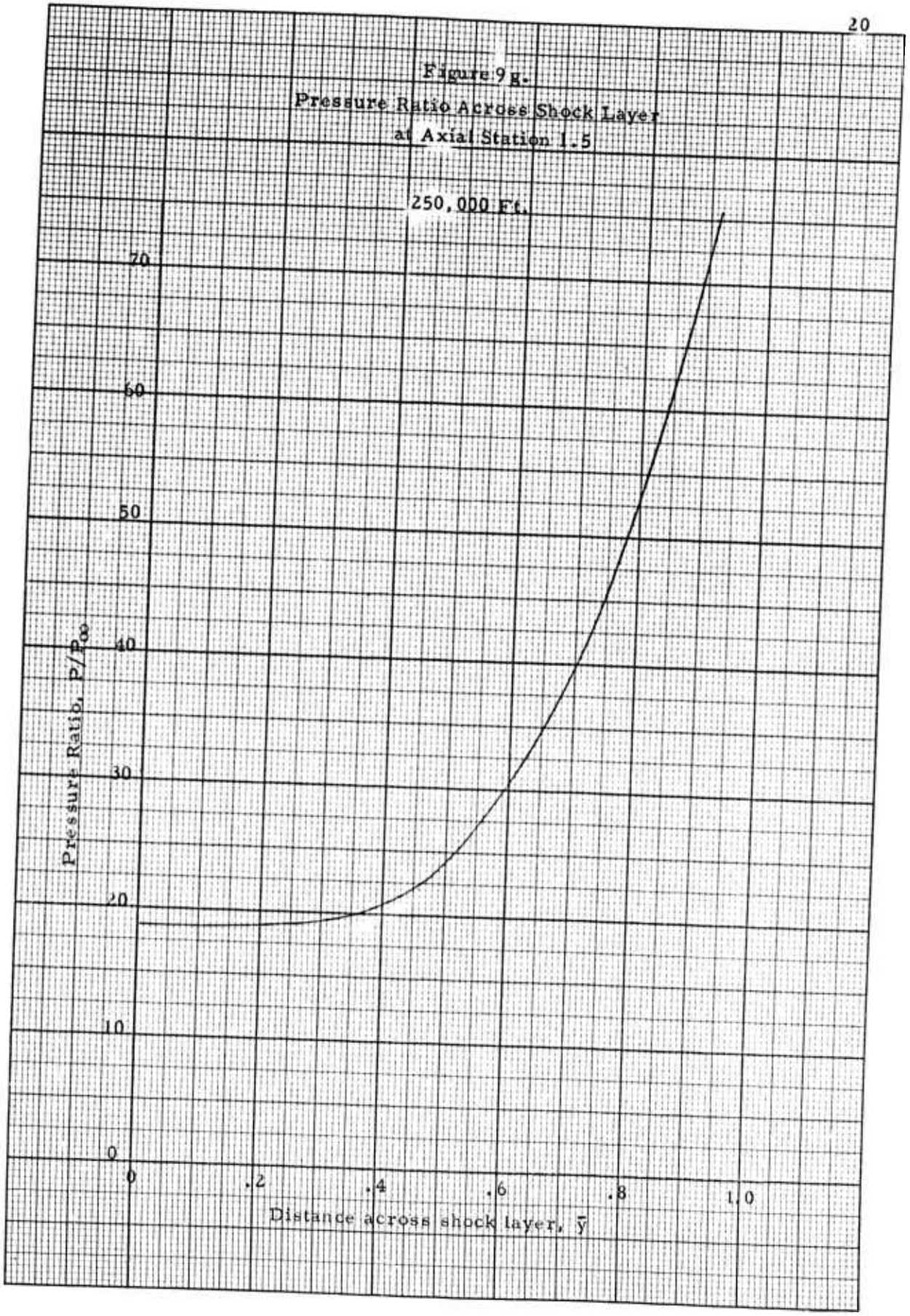

Figure 10a.
Density Ratio Across Shock Layer
at Axial Station 1.5

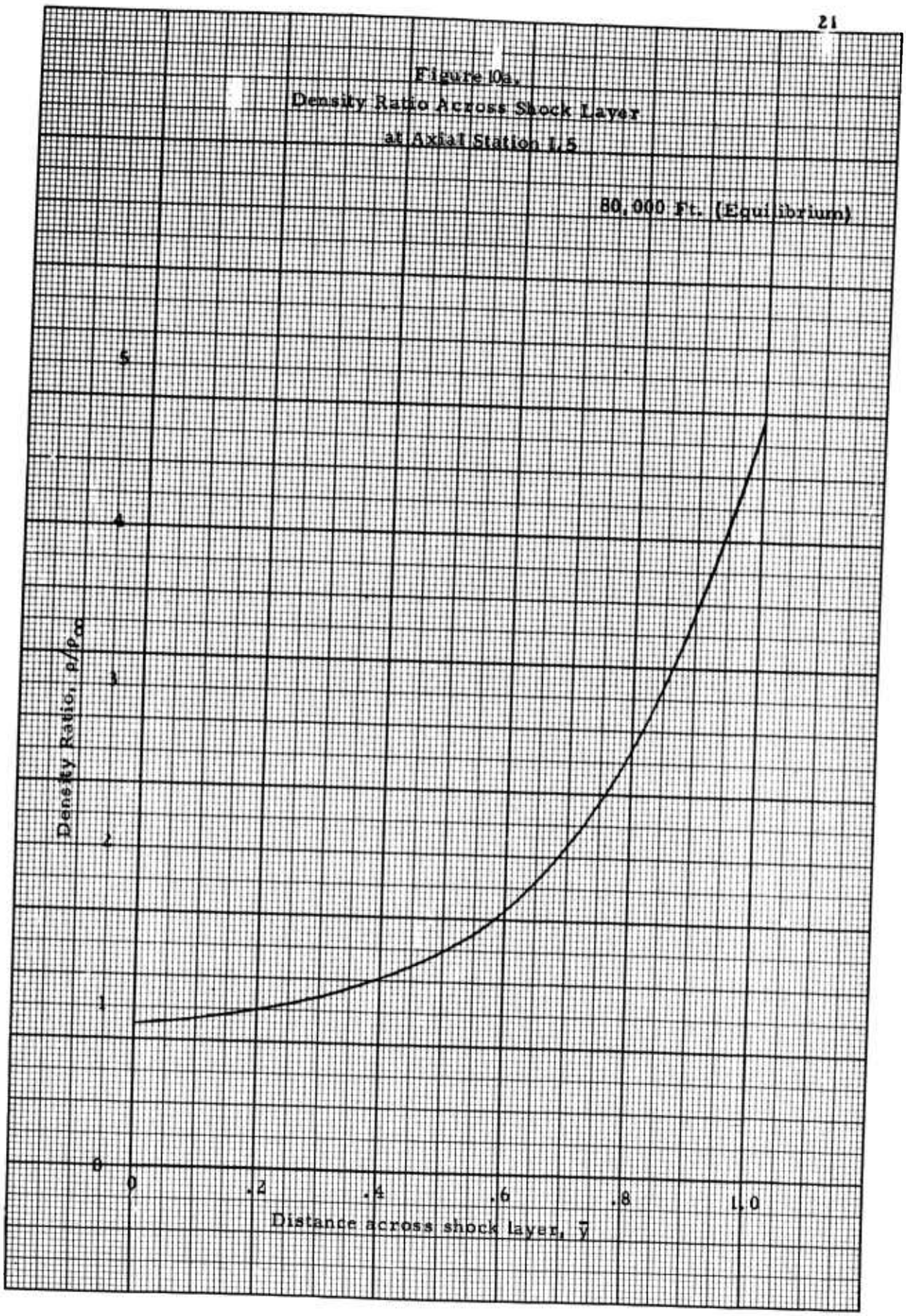

Figure10b.

Density Ratio Across Shock Layer
at Axial Station 1.5

80,000 Ft. (Frozen)

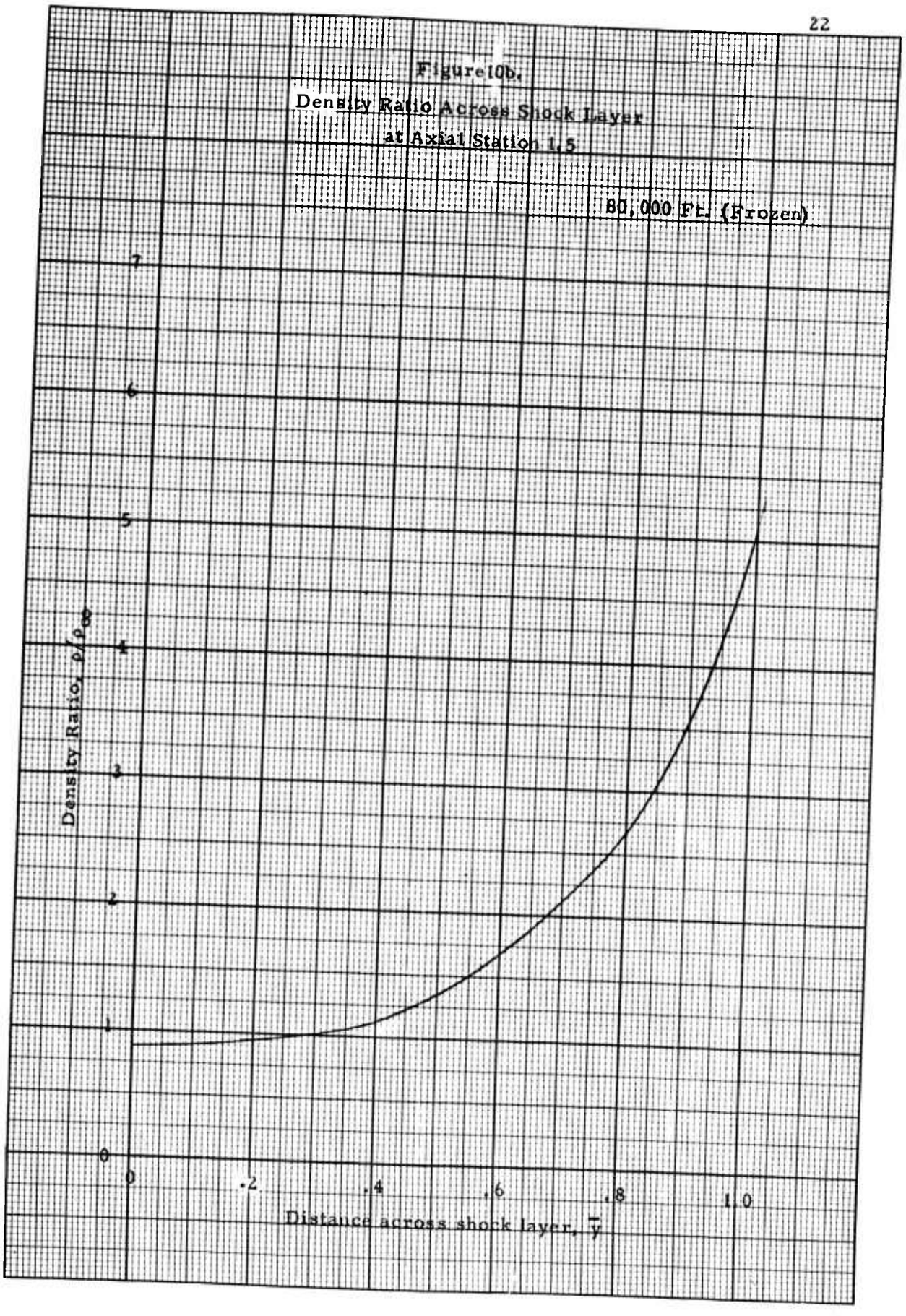

Figure 10e.

Density Ratio Across Shock Layer
at Axial Station 1.5

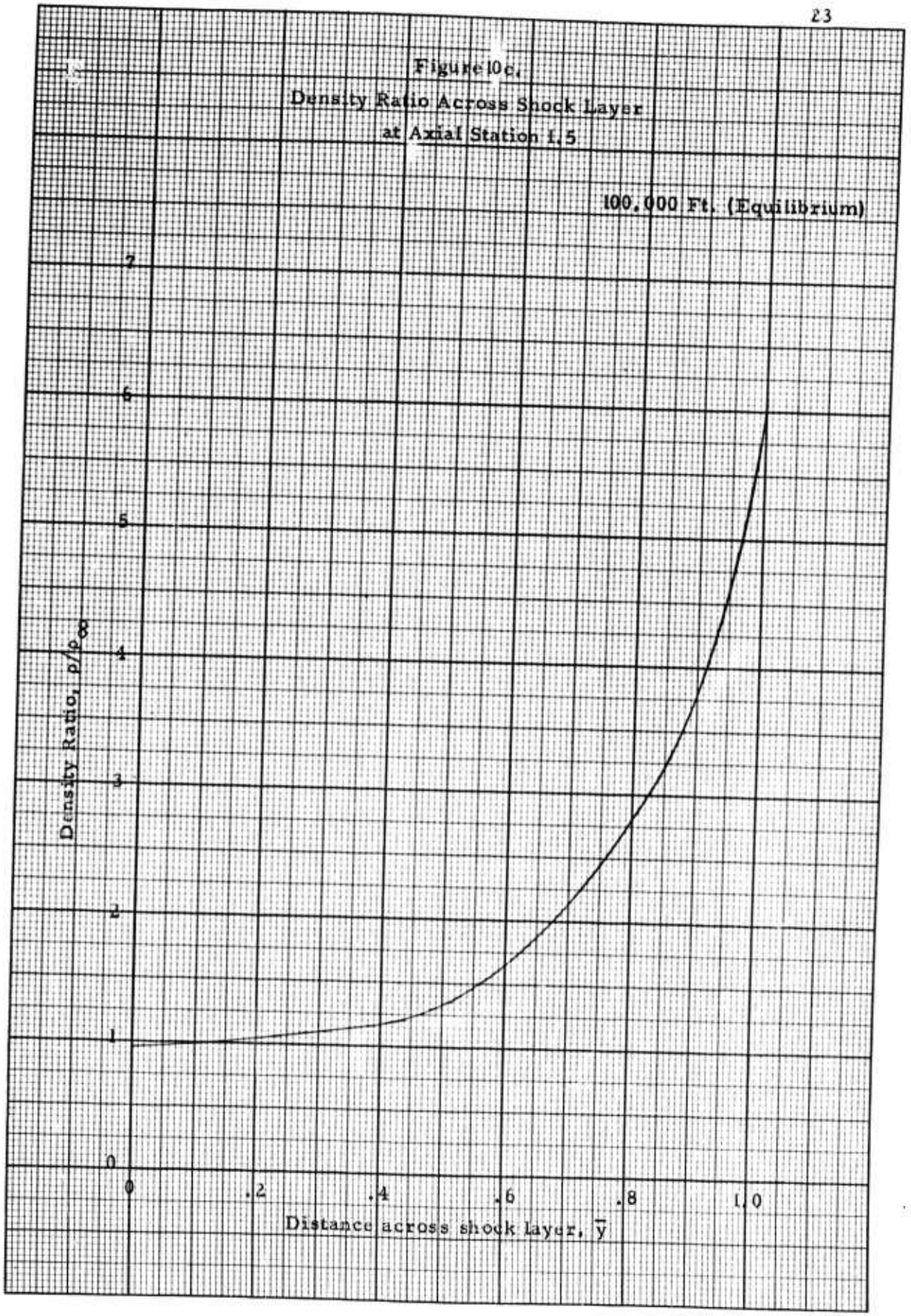

Figure 10d.
Density Ratio Across Shock Layer
at Axial Station 1.5

100,000 Ft. (Frozen)

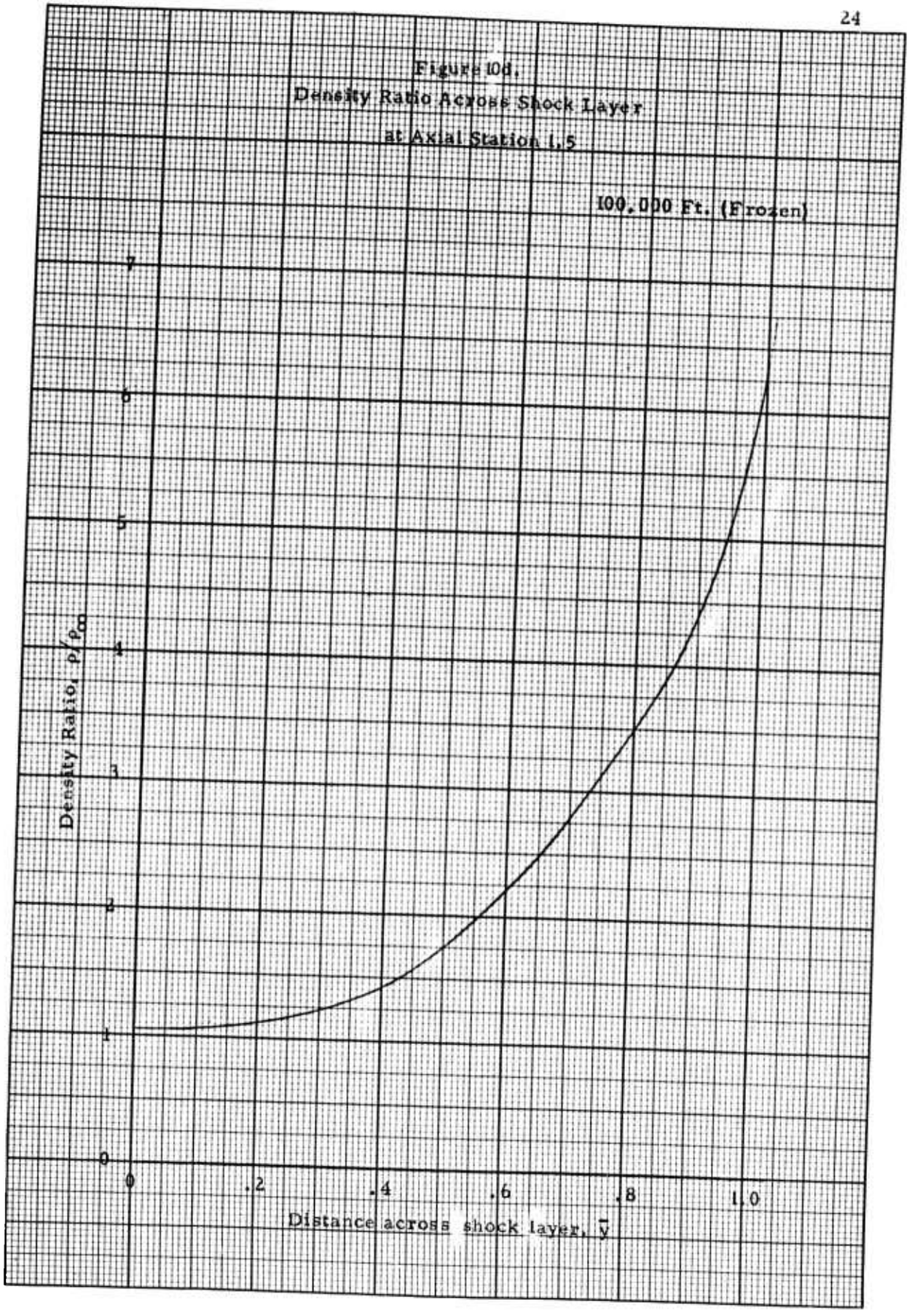

Figure 10e.
Density Ratio Across Shock Layer
at Axial Station 1.5

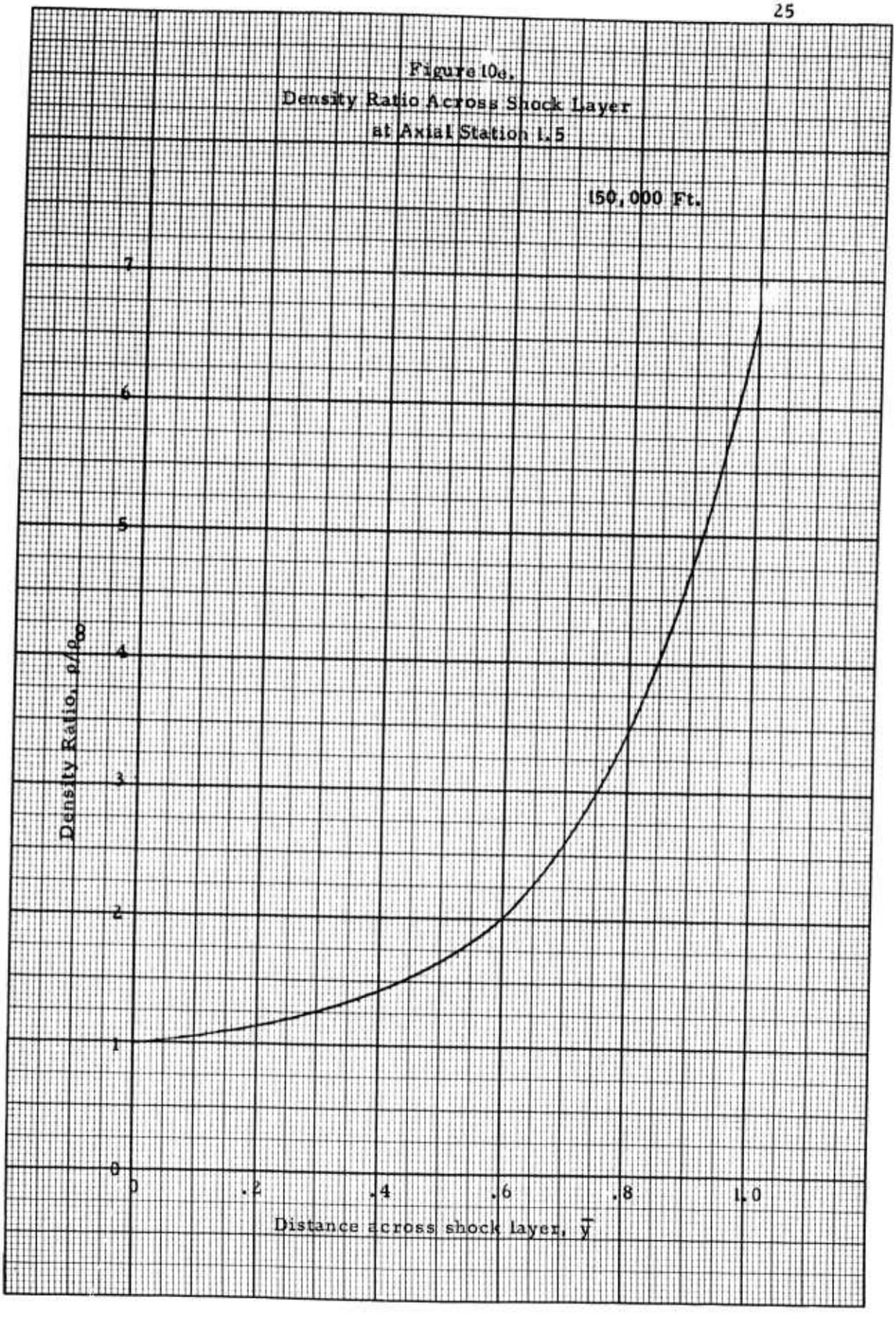

Figure 10f.
Density Ratio Across Shock Layer
at Axial Station 1.5

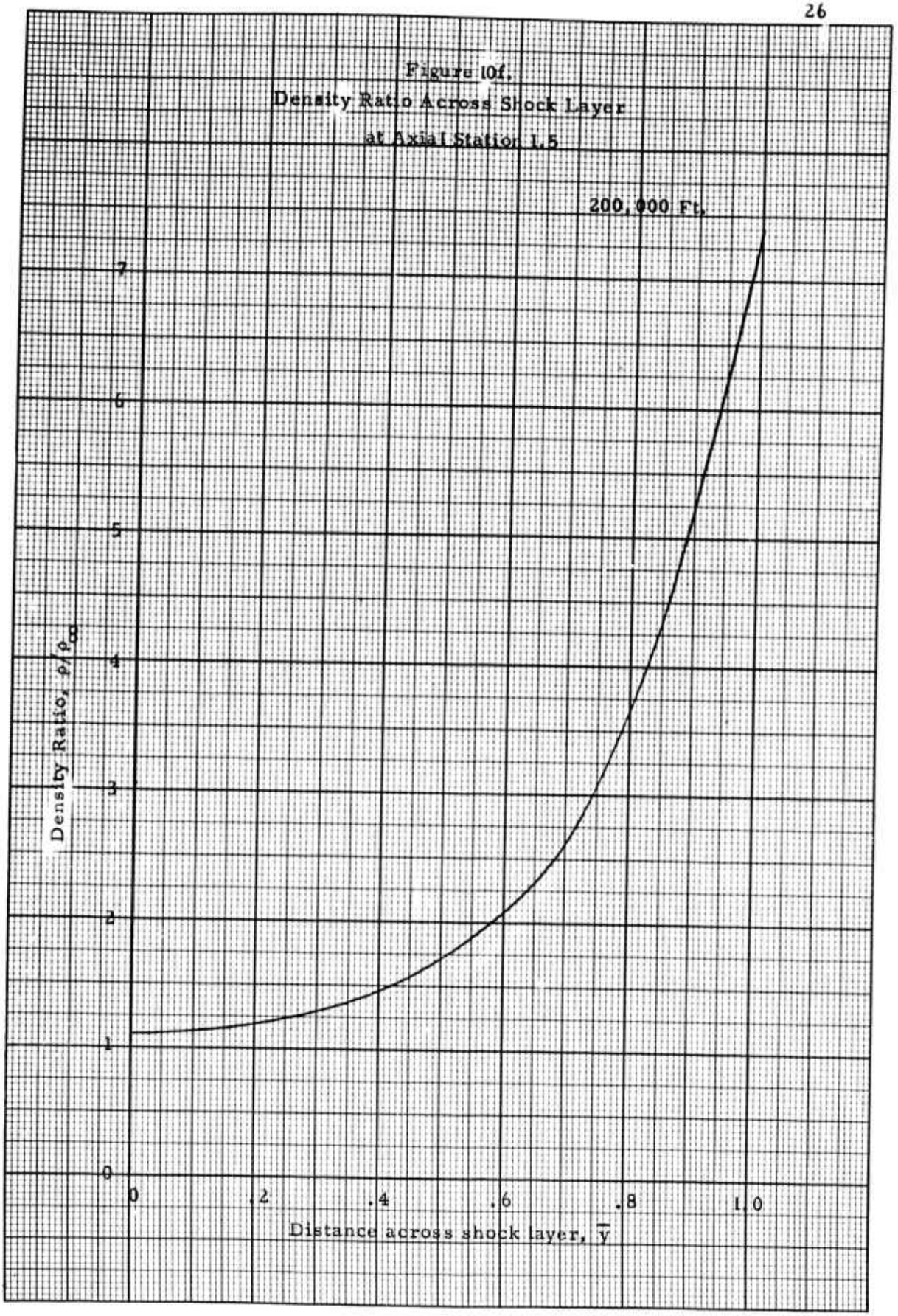

Figure 10g.
Density Ratio Across Shock Layer
at Axial Station 1.5

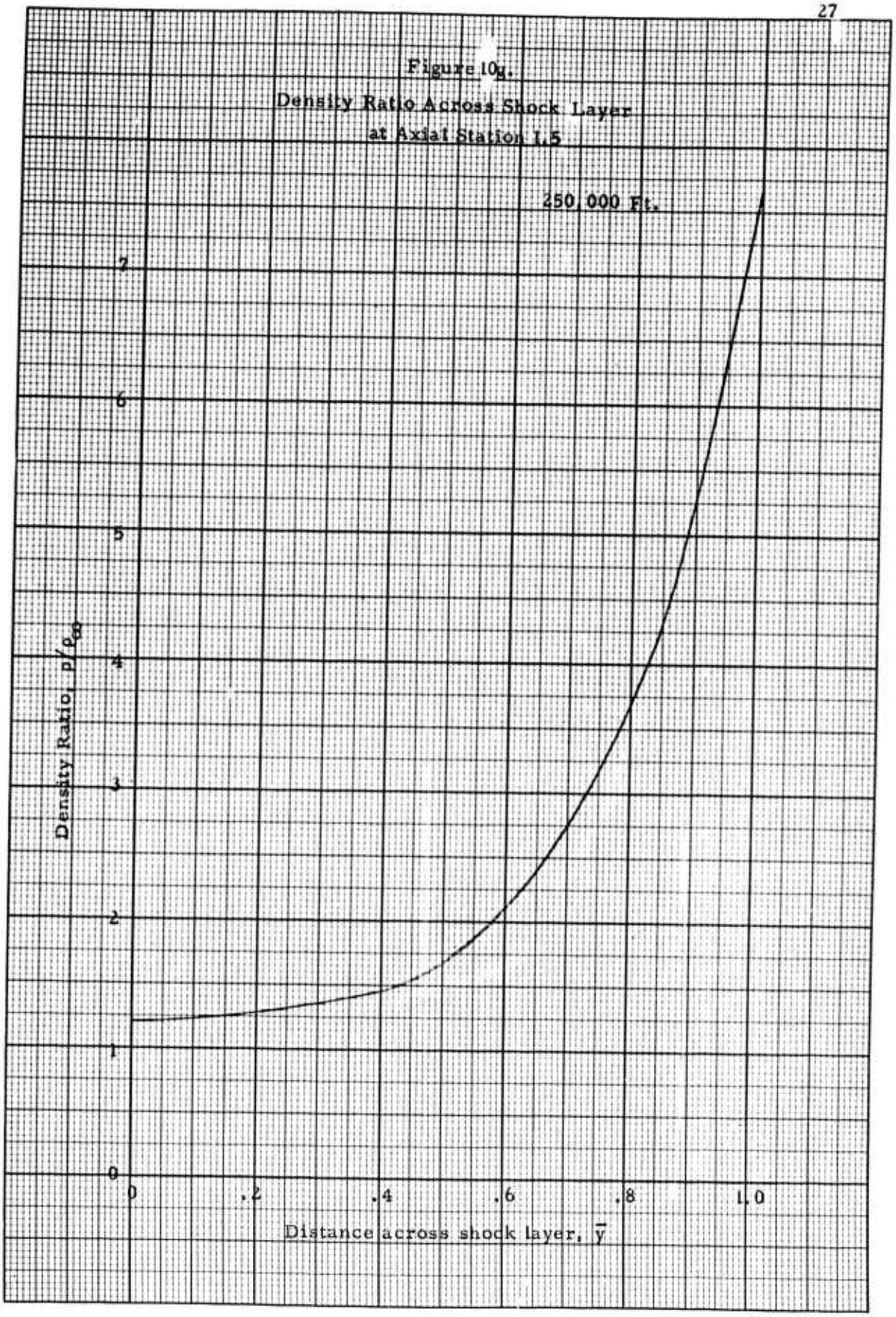

Figure 11a.

Temperature Distribution Across Shock Layer at Axial Station 1.5

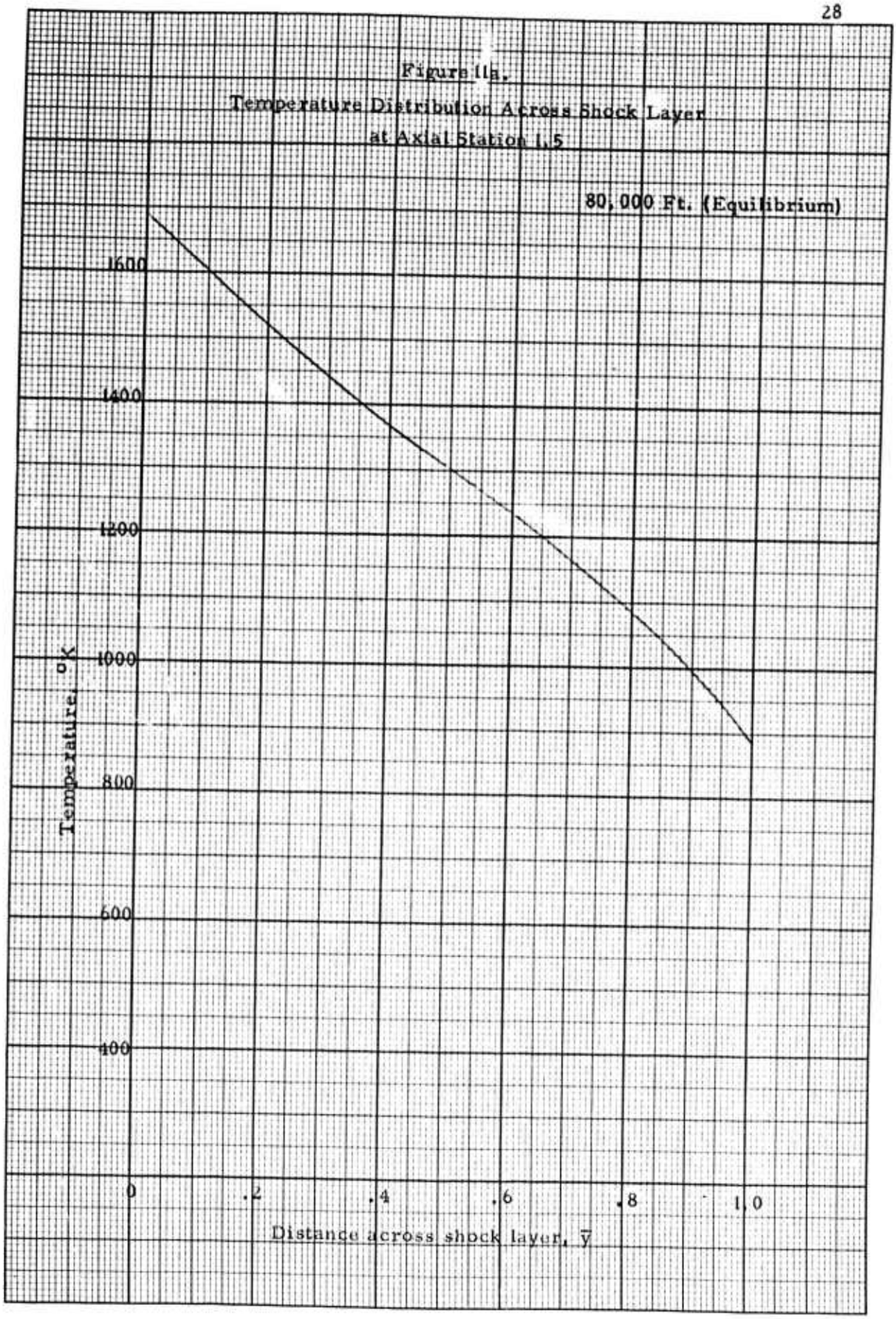

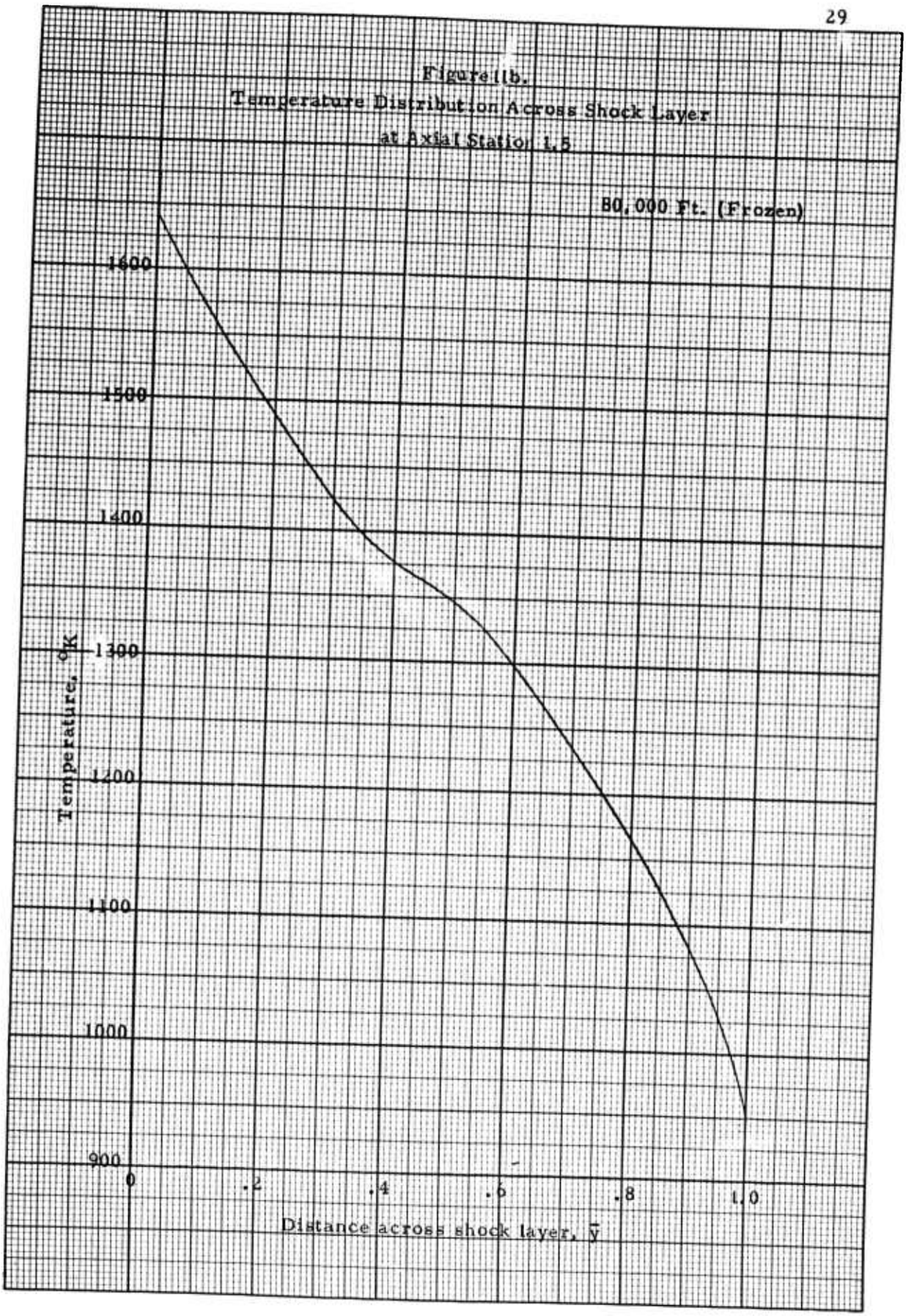

Figure 11b.
Temperature Distribution Across Shock Layer
at Axial Station 1.5

Figure IIc.
Temperature Distribution Across Shock Layer
at Axial Station 1.5

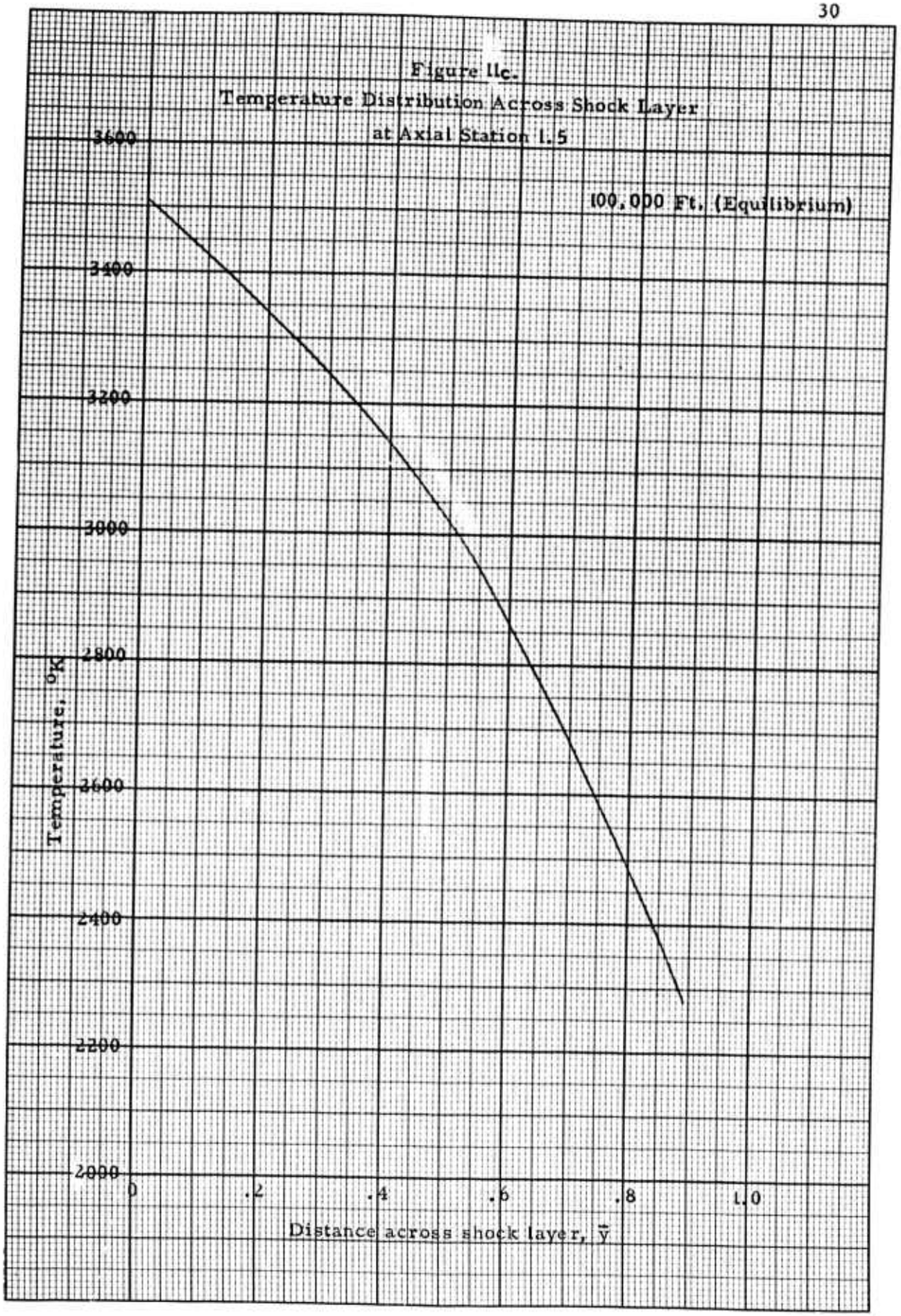

Figure IId.
Temperature Distribution Across Shock Layer
at Axial Station 1.5

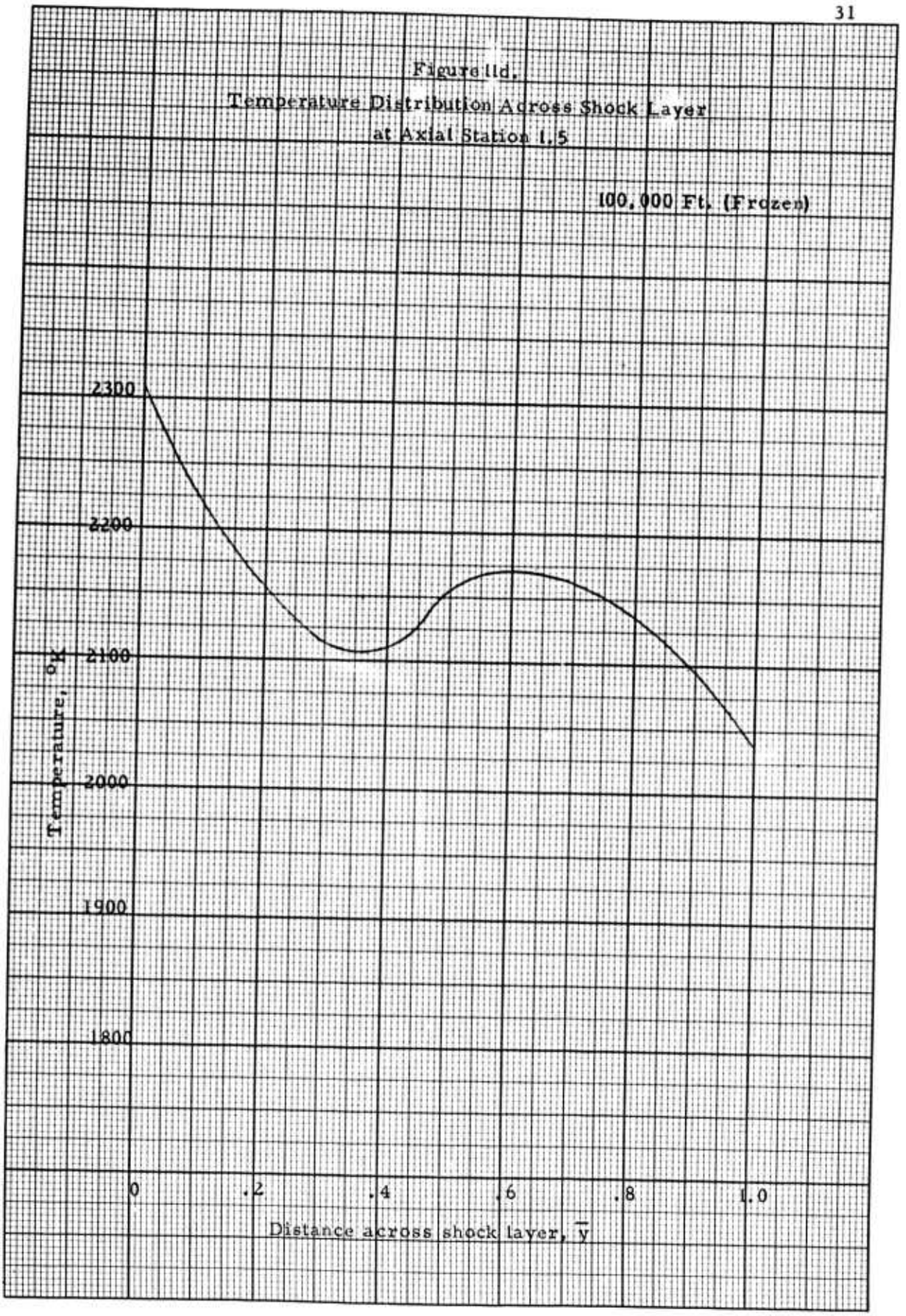

Figure IIe.
Temperature Distribution Across Shock Layer
at Axial Station L.5

150,000 Ft.

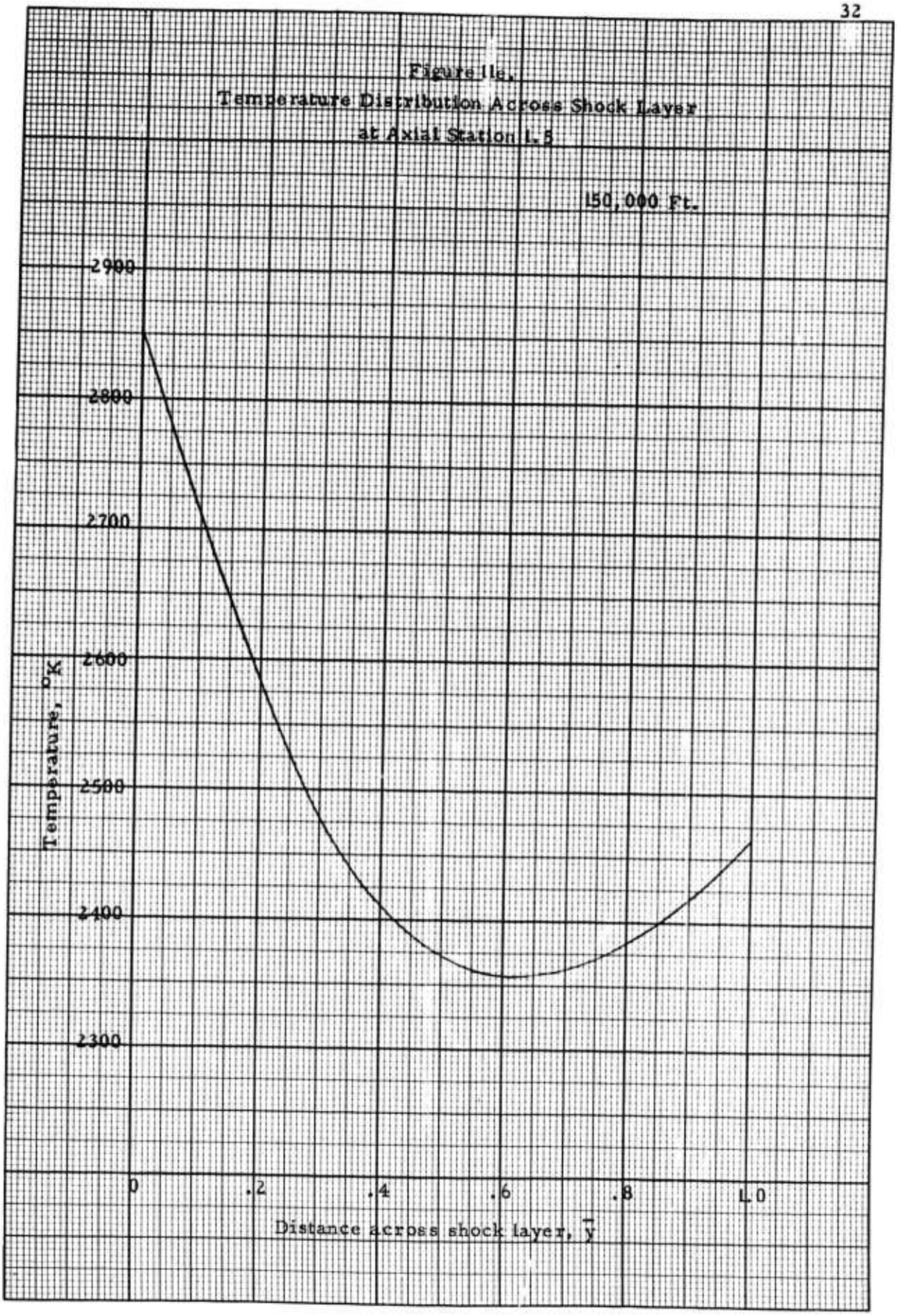

Figure 11f.
Temperature Distribution Across Shock Layer
at Axial Station L.5

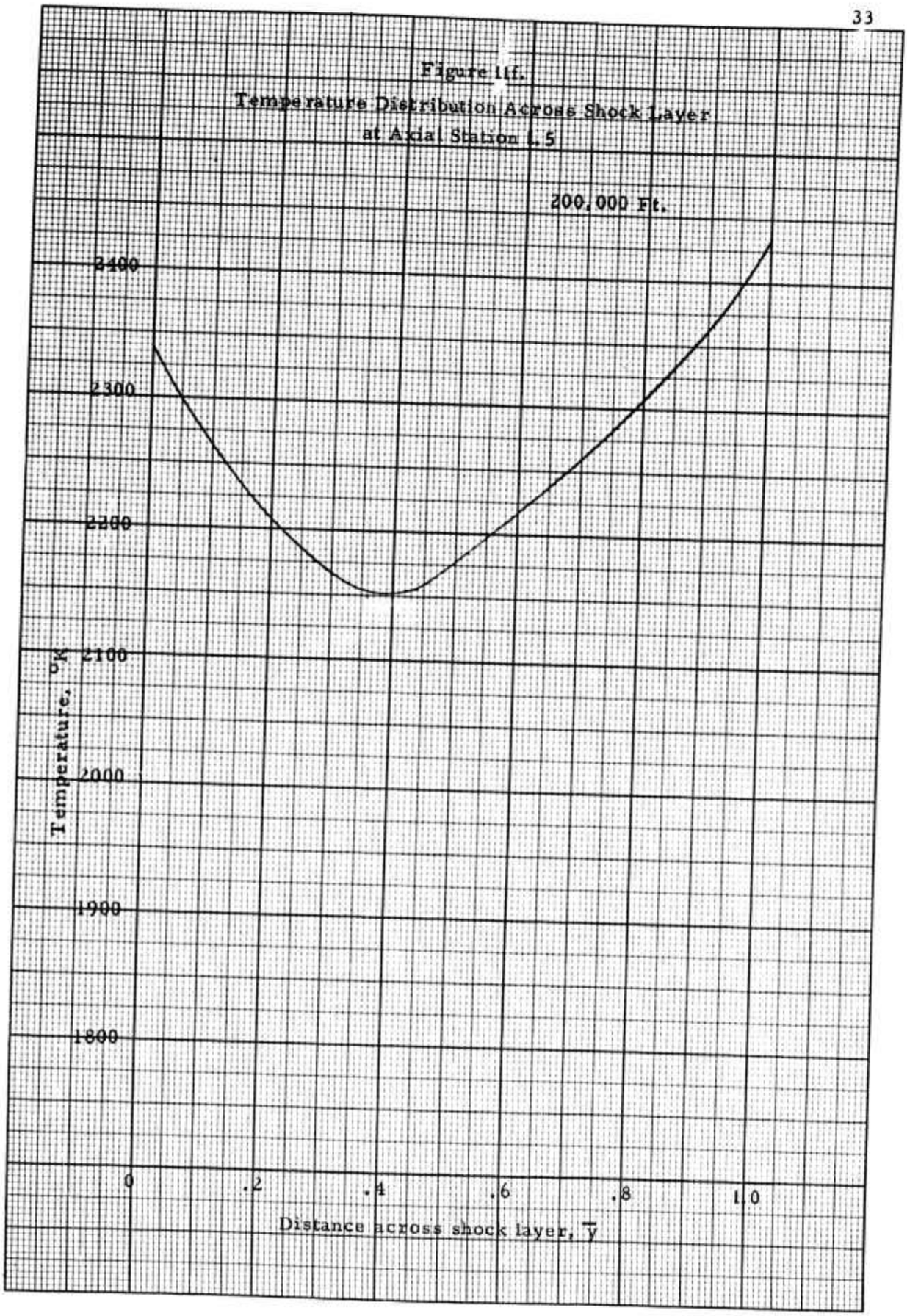

Figure 11g.
Temperature Distribution Across Shock Layer
at Axial Station 1.5

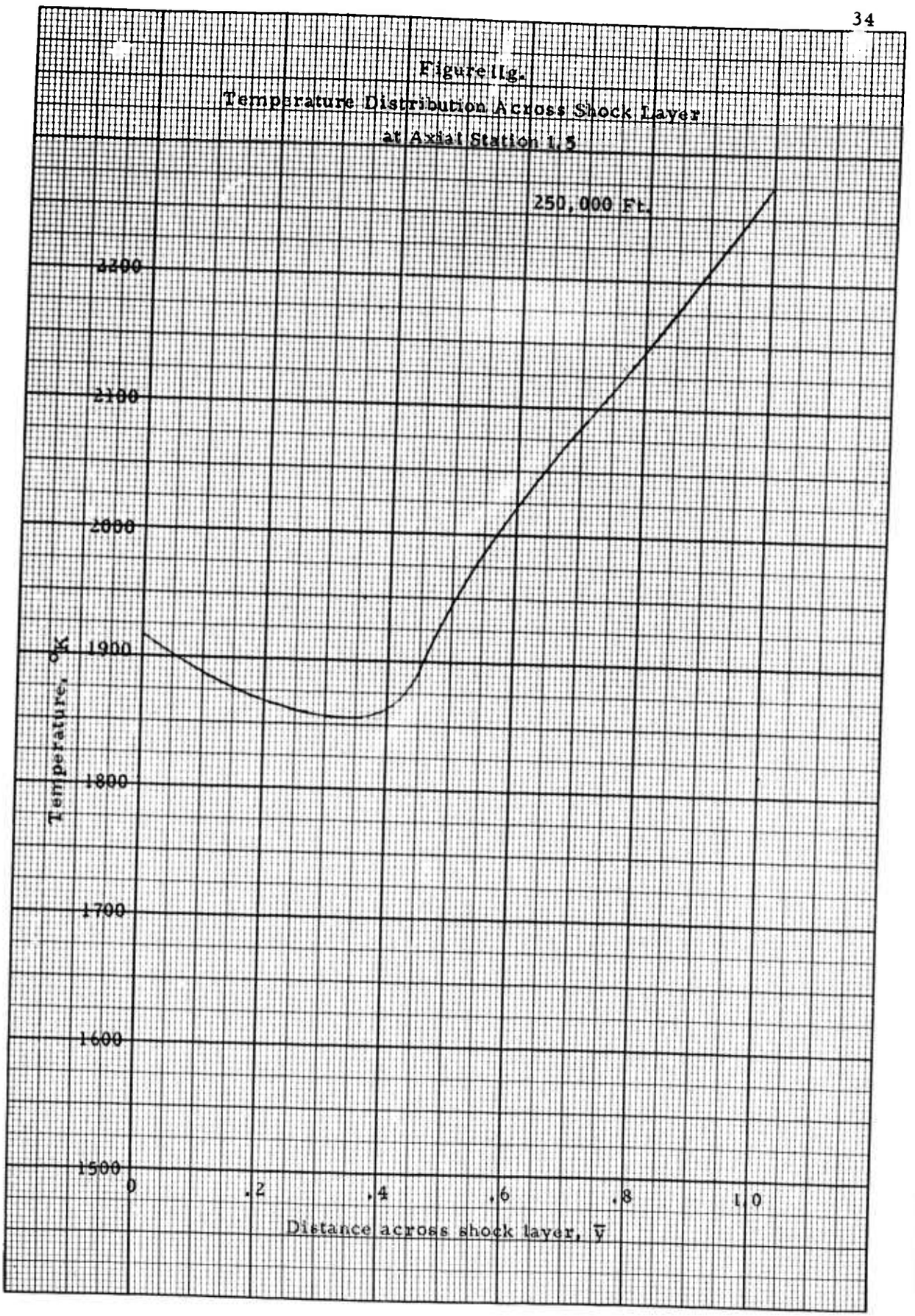

Figure 12a.
Electron Density Distribution Across Shock Layer
at Base of Core

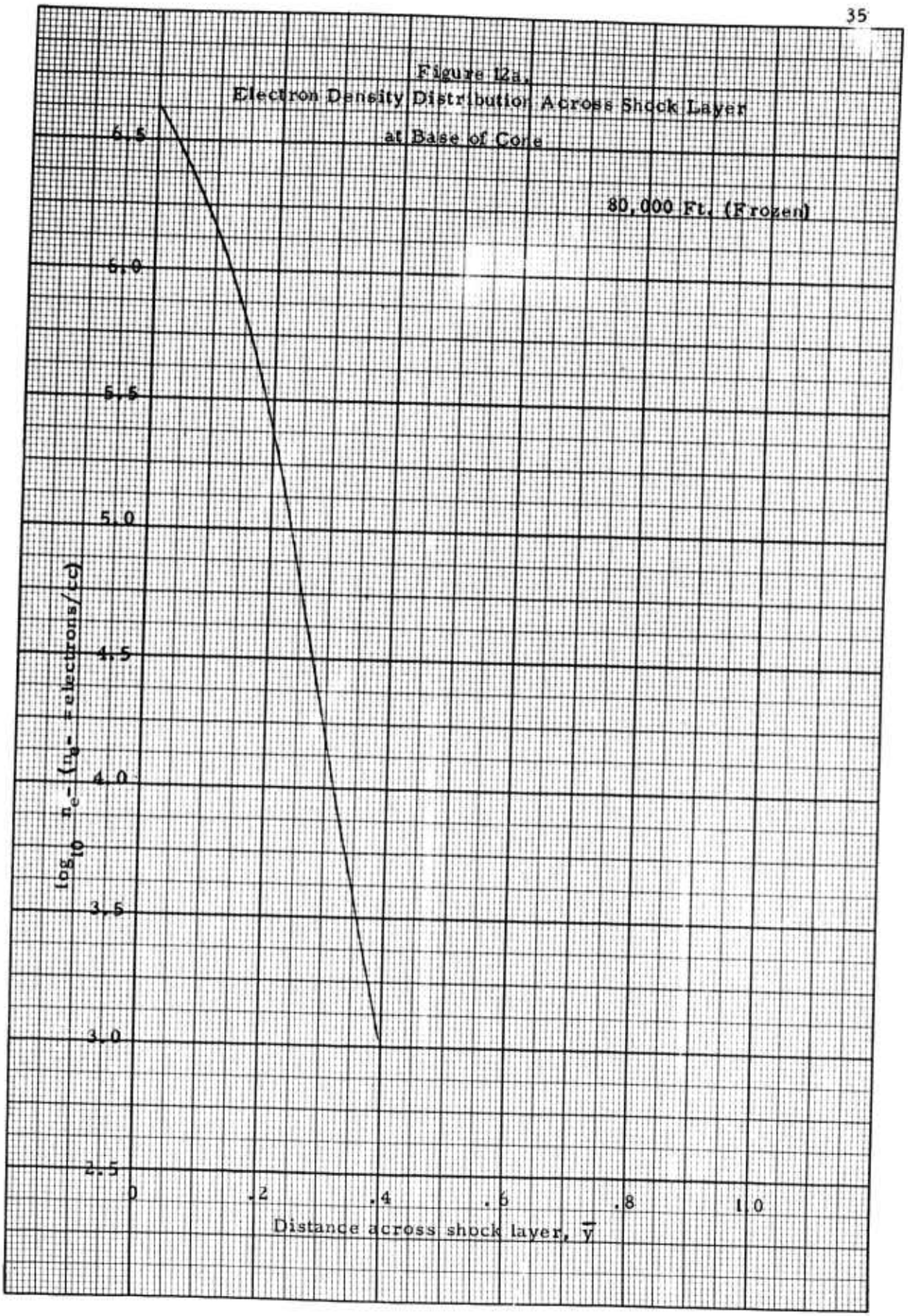

Figure 12b.
Electron Density Distribution Across Shock Layer
at Base of Cone

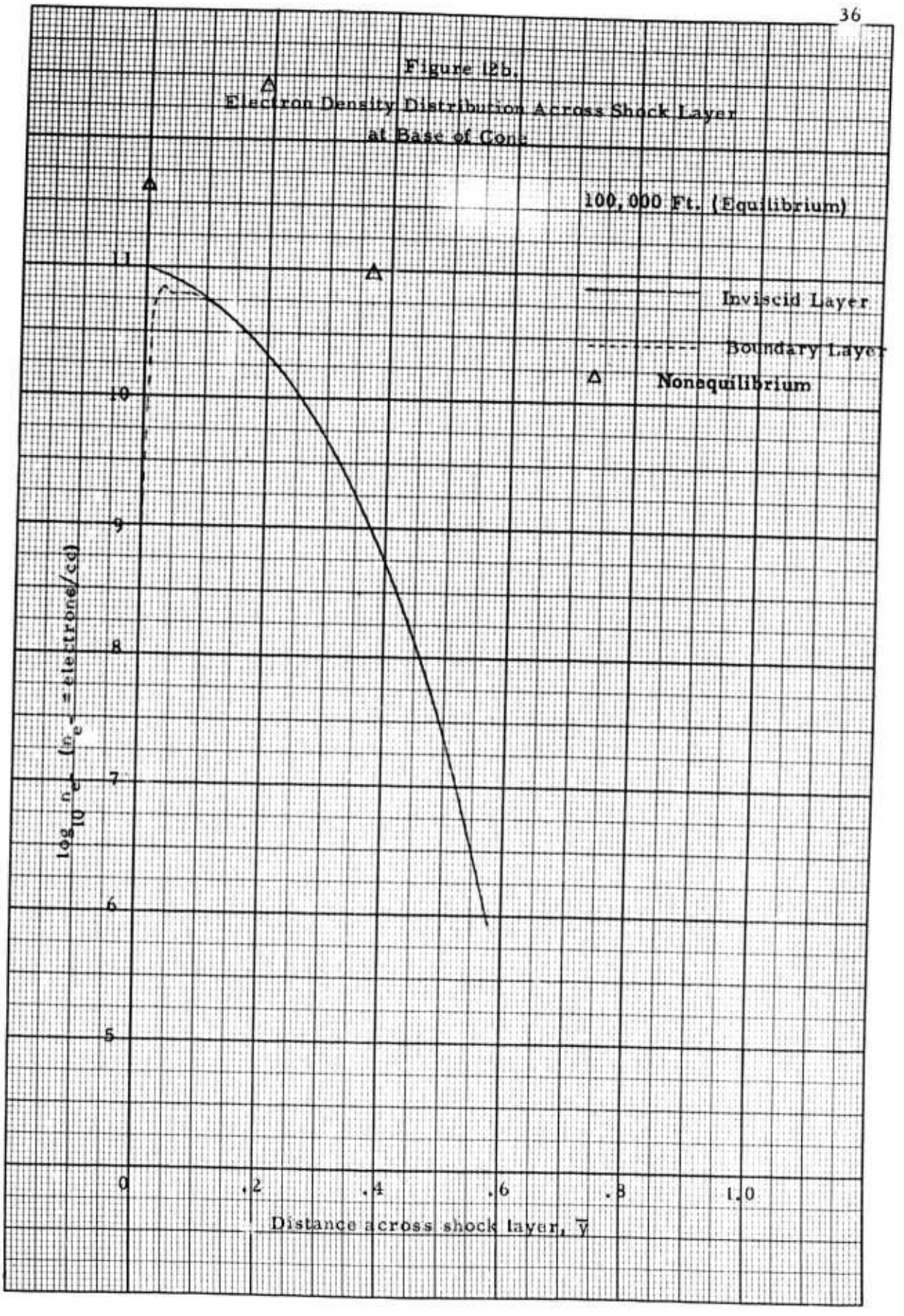

Figure 12c.
Electron Density Distribution Across Shock Layer
at Base of Cone

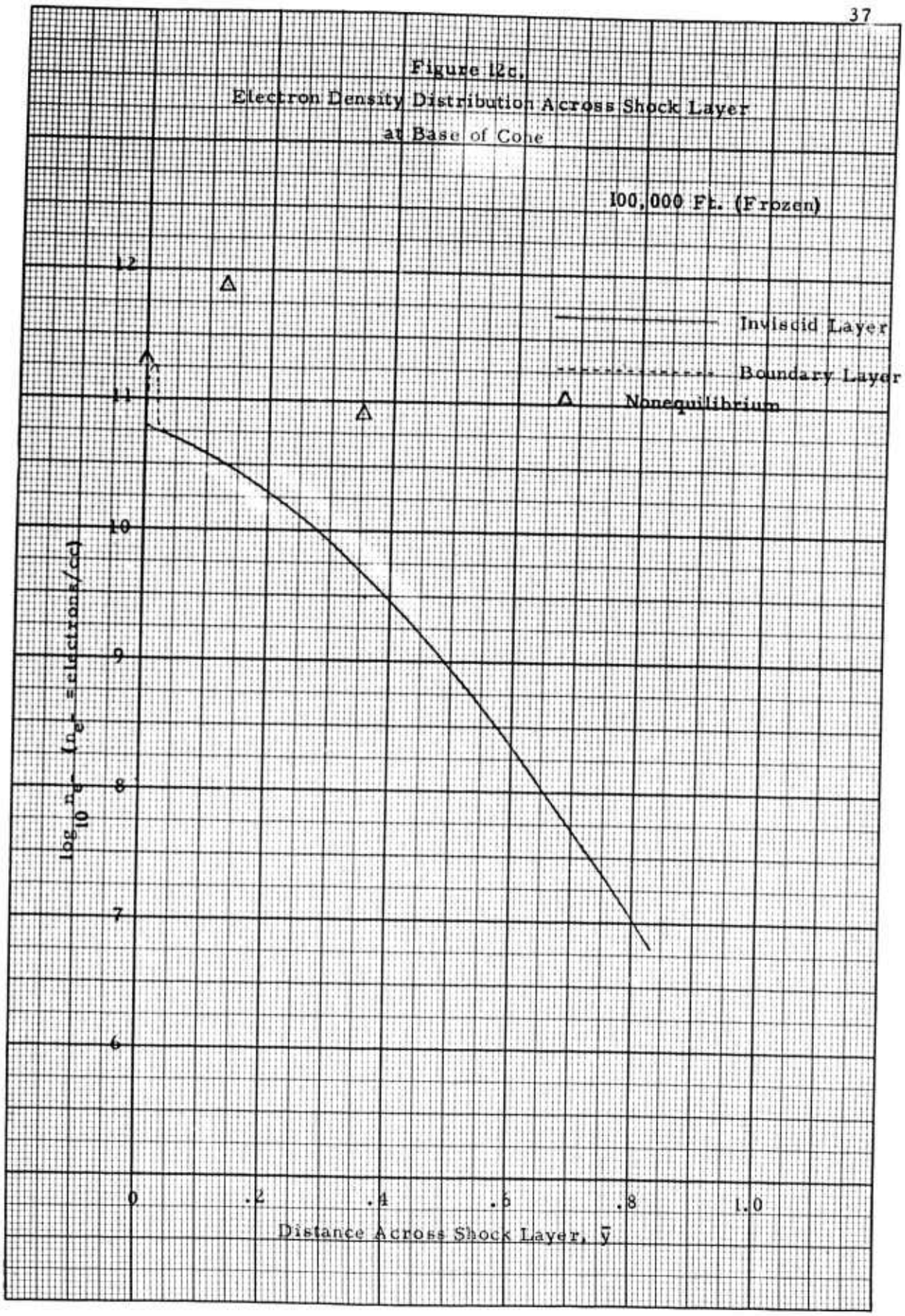

Figure 12d.
Electron Density Distribution Across Shock Layer
at Base of Cone

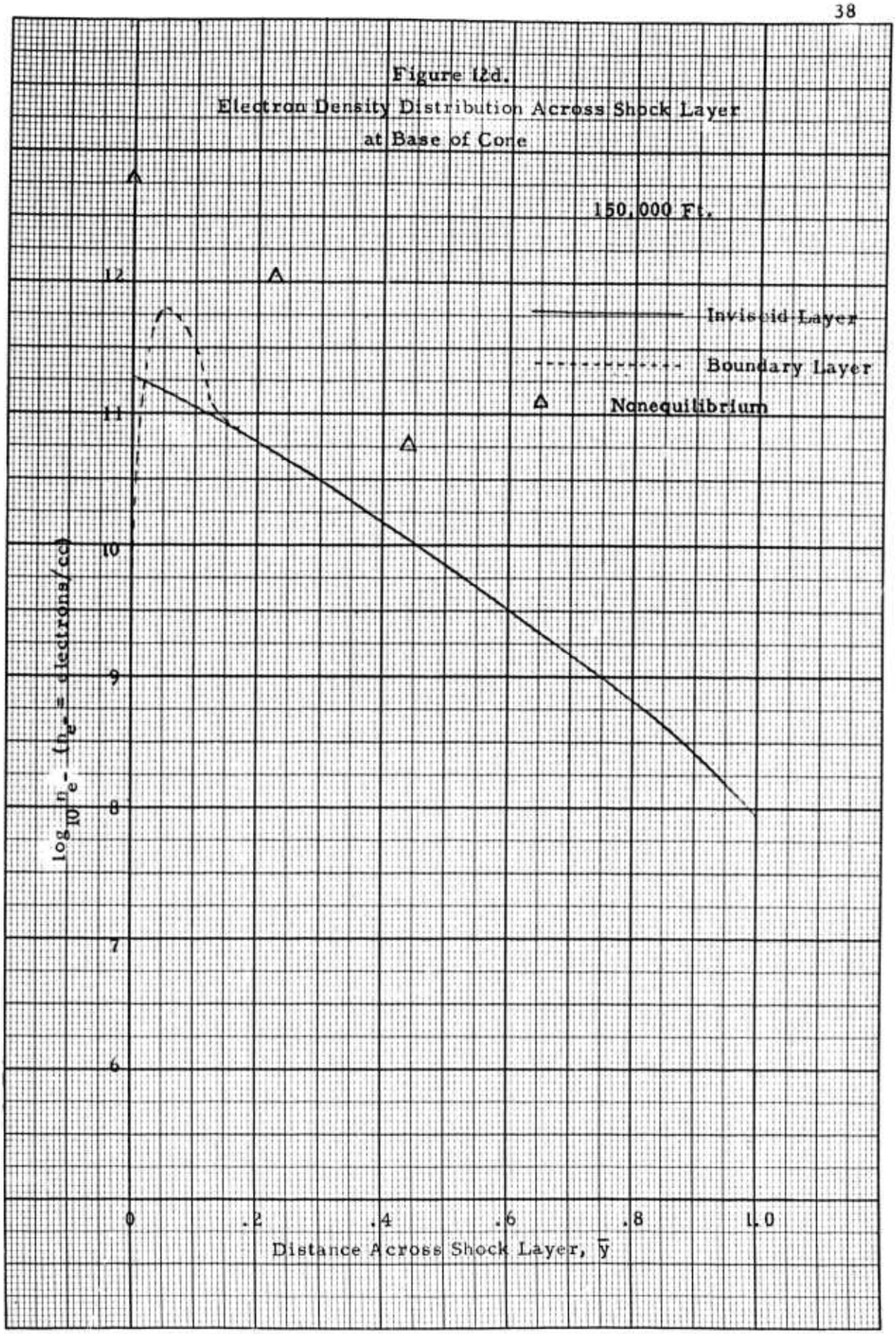

Figure 12e.

Electron Density Distribution Across Shock Layer at Base of Cone

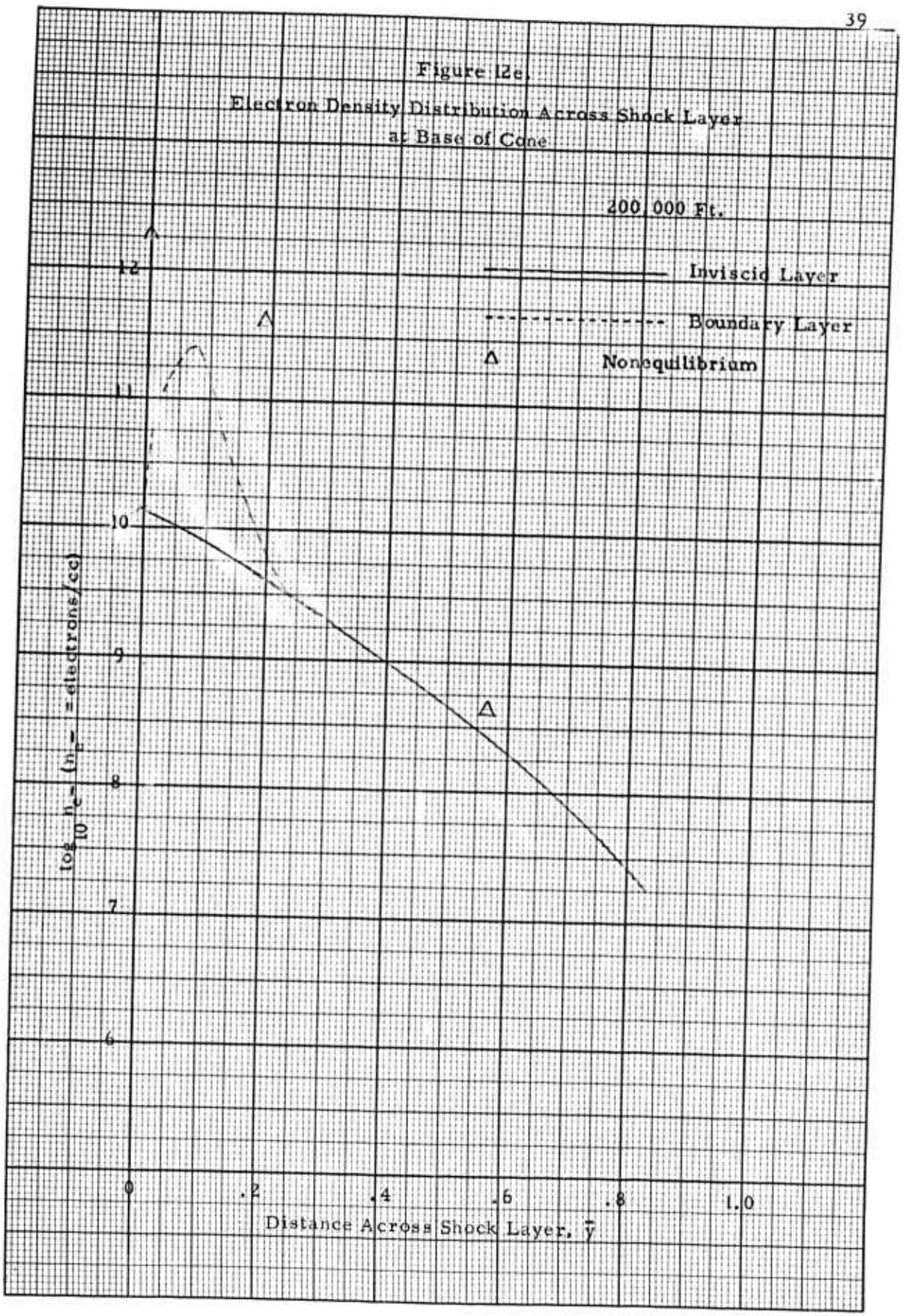

Figure 12 f.
Electron Density Distribution Across Shock Layer
at Base of Cone

250,000 Ft.

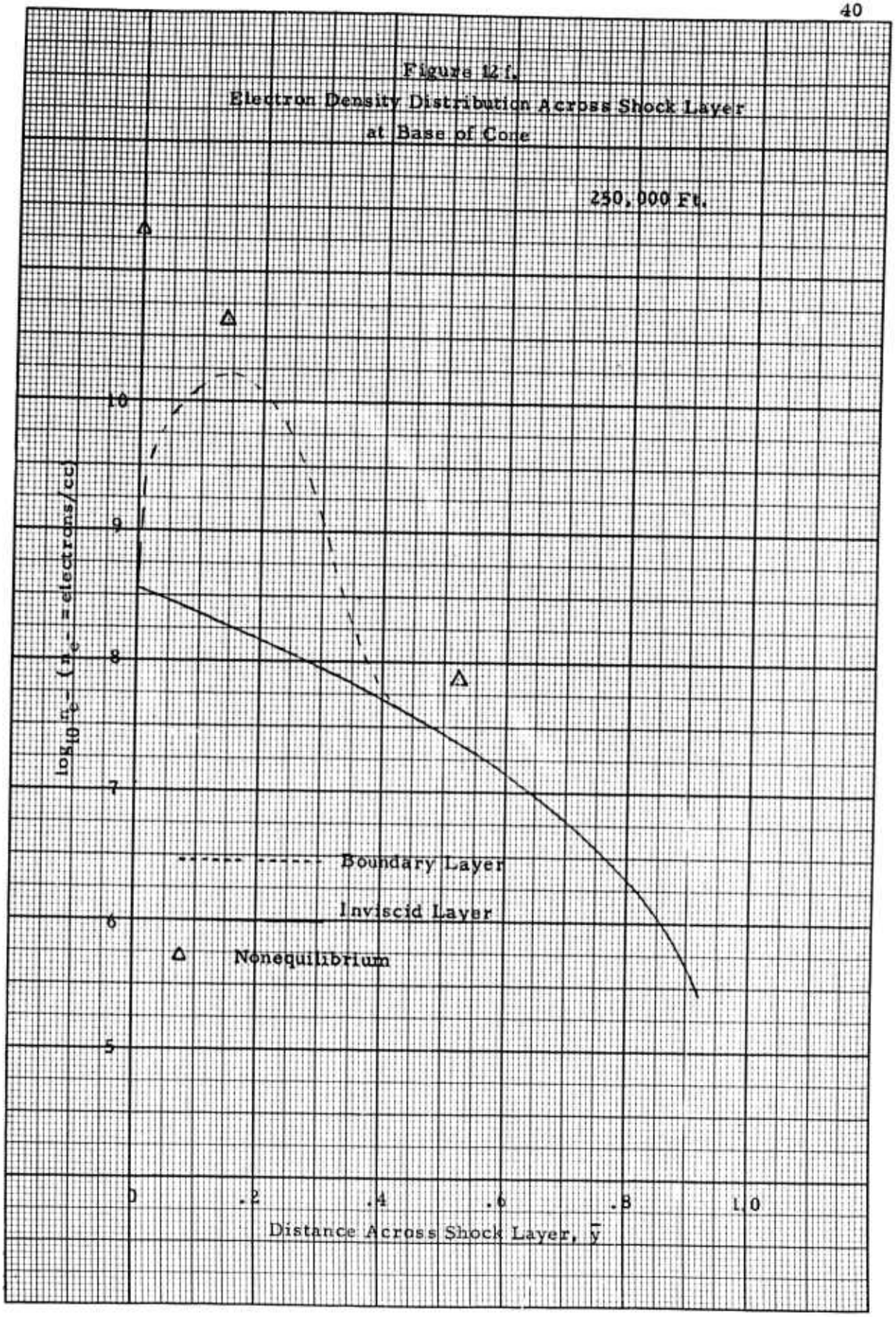

Figure 13a.
Pressure Ratio Across Shock Layer
at Base of Cone

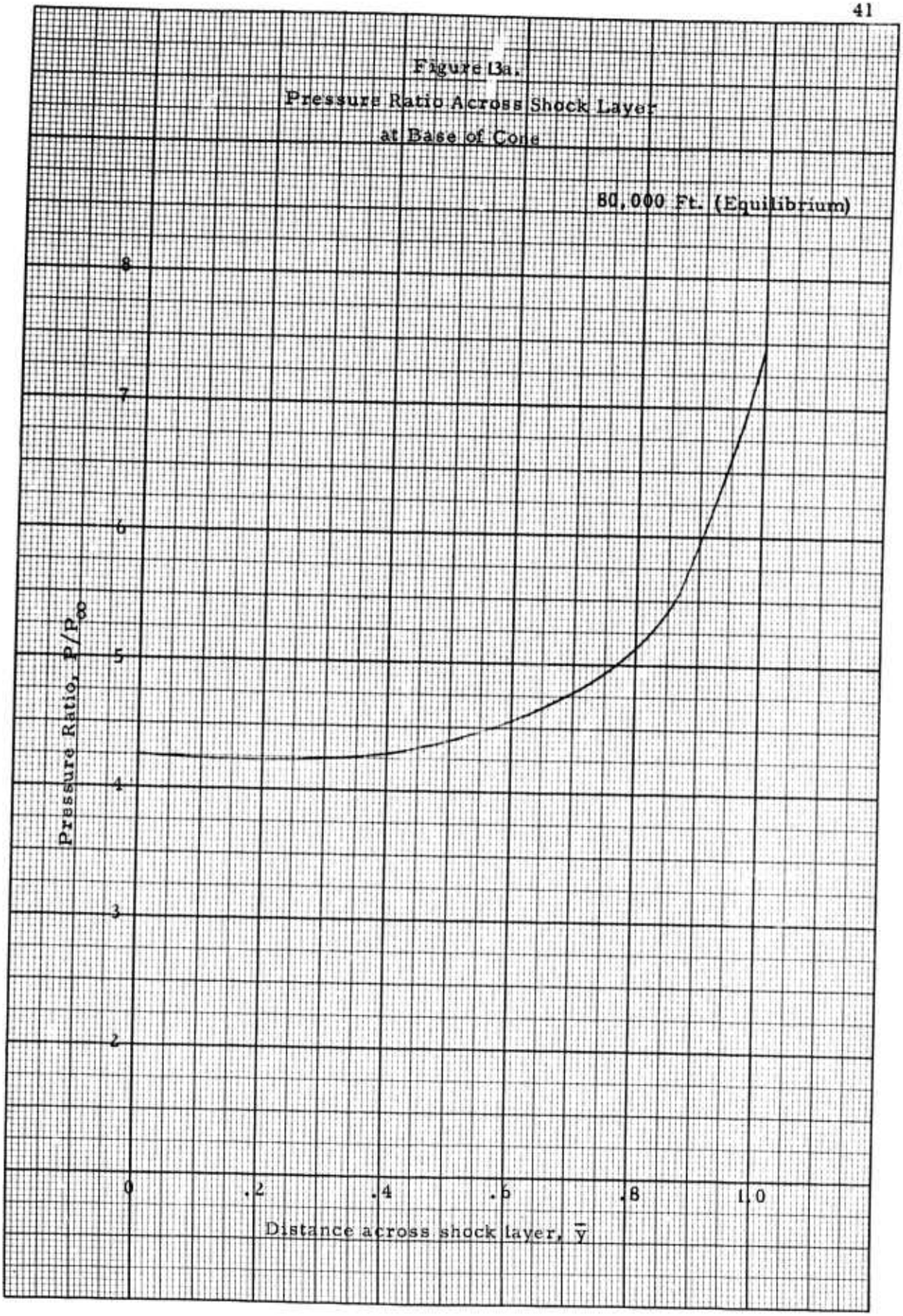

Figure 13b.
Pressure Ratio Across Shock Layer
at Base of Cone

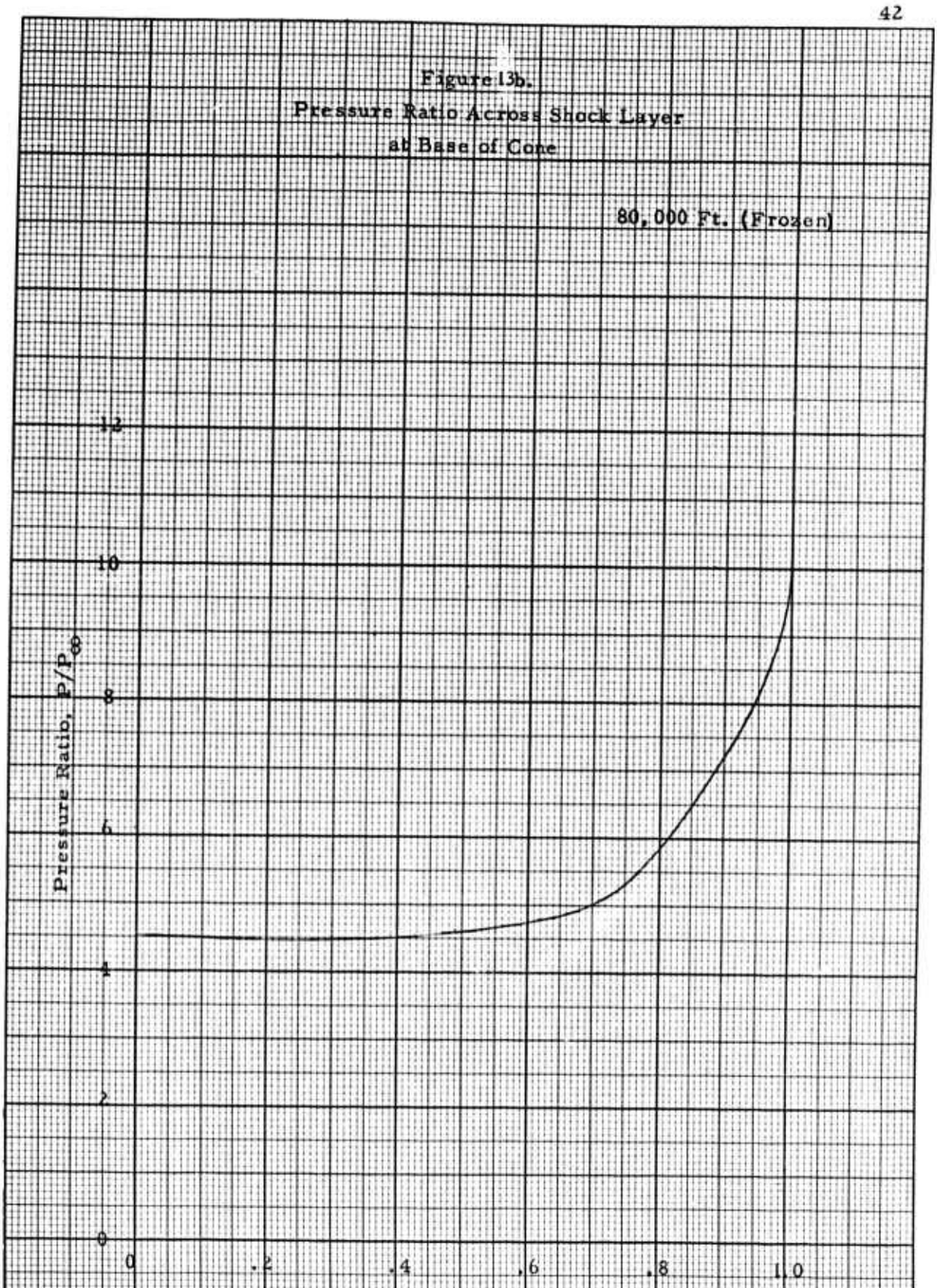

Figure 13c.
Pressure Ratio Across Shock Layer
at Base of Cone

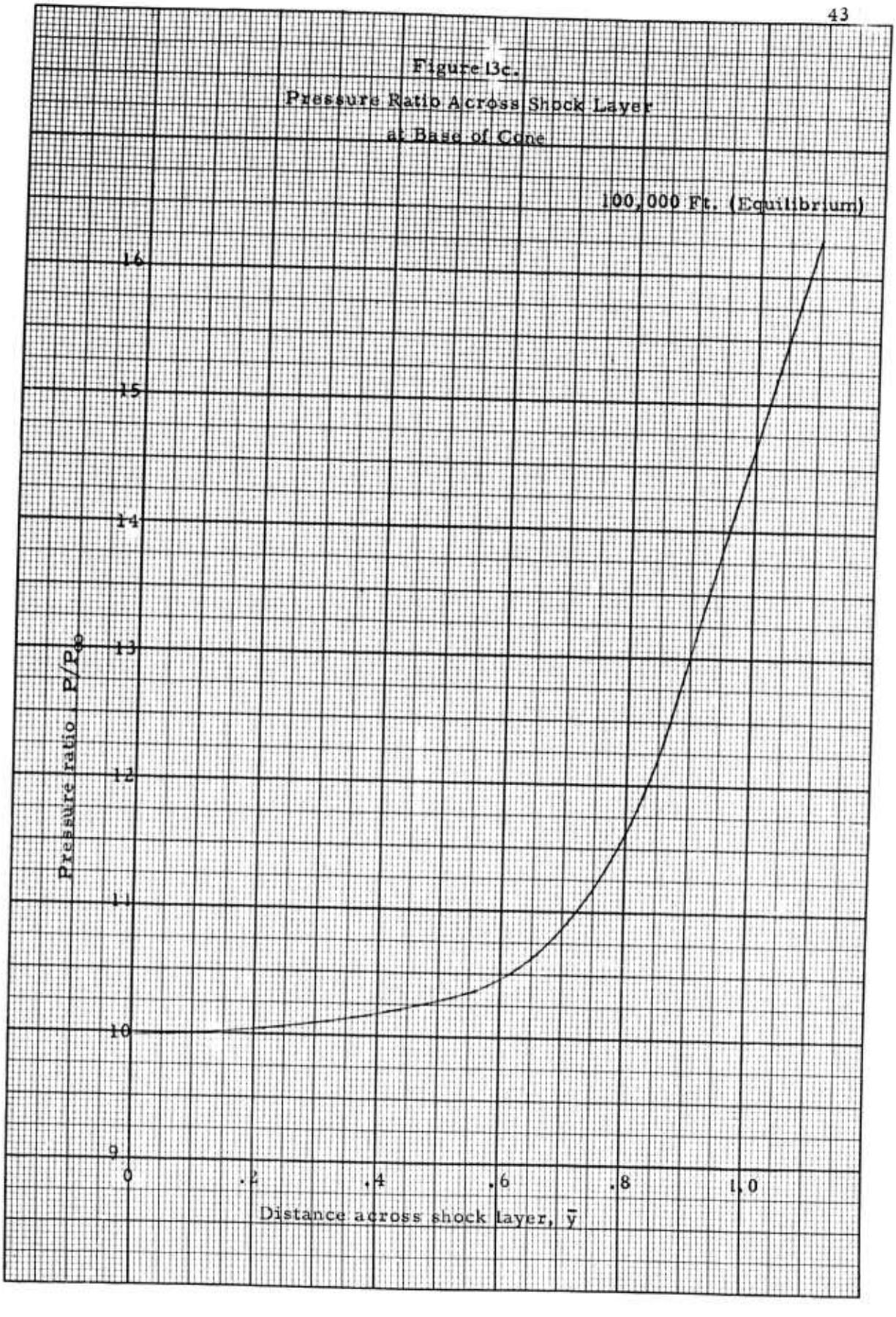

Figure13d.

Pressure Ratio Across Shock Layer at Base of Cone

100,000 Ft. (Frozen)

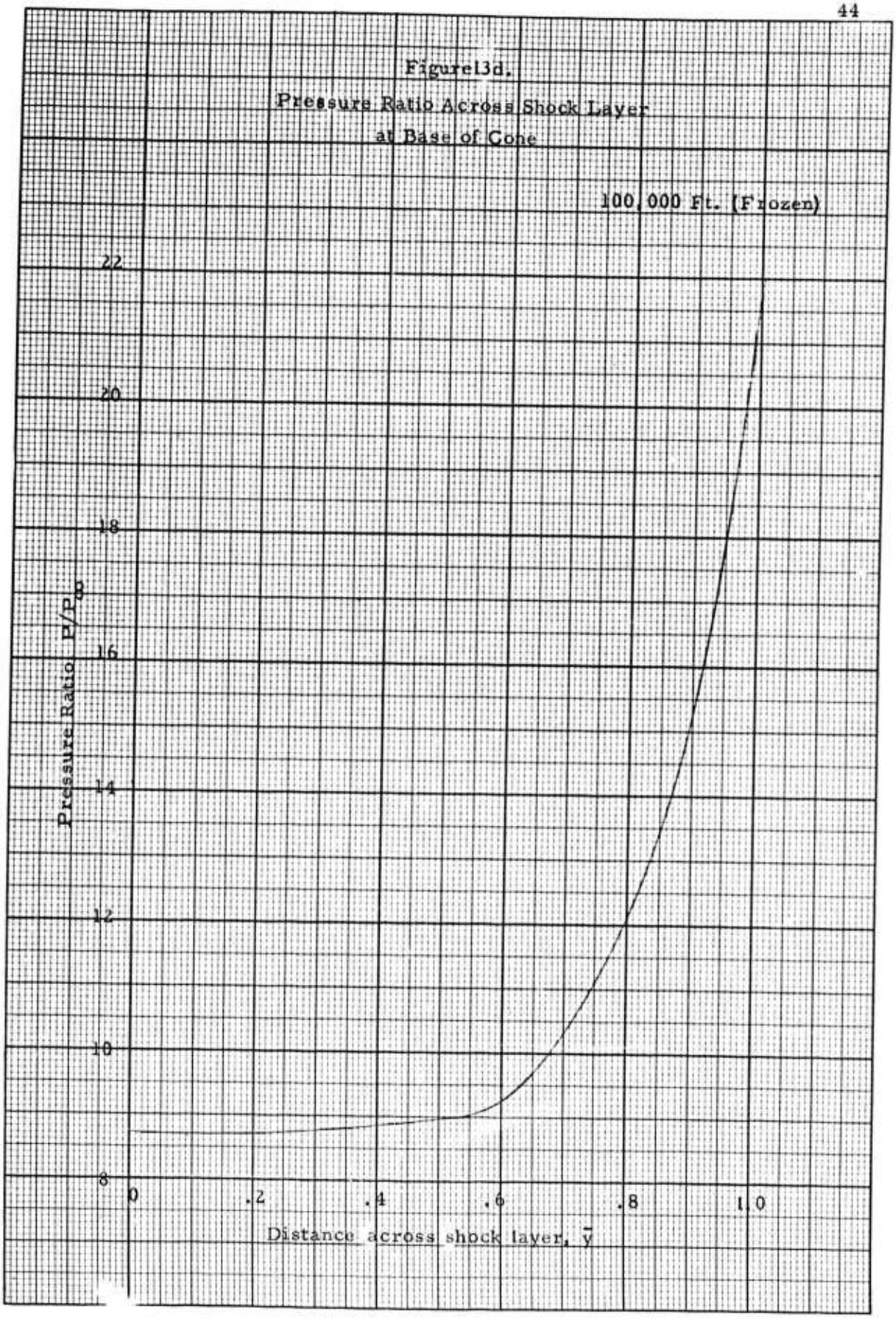

Figure 13e.
Pressure Ratio Across Shock Layer
at Base of Cone

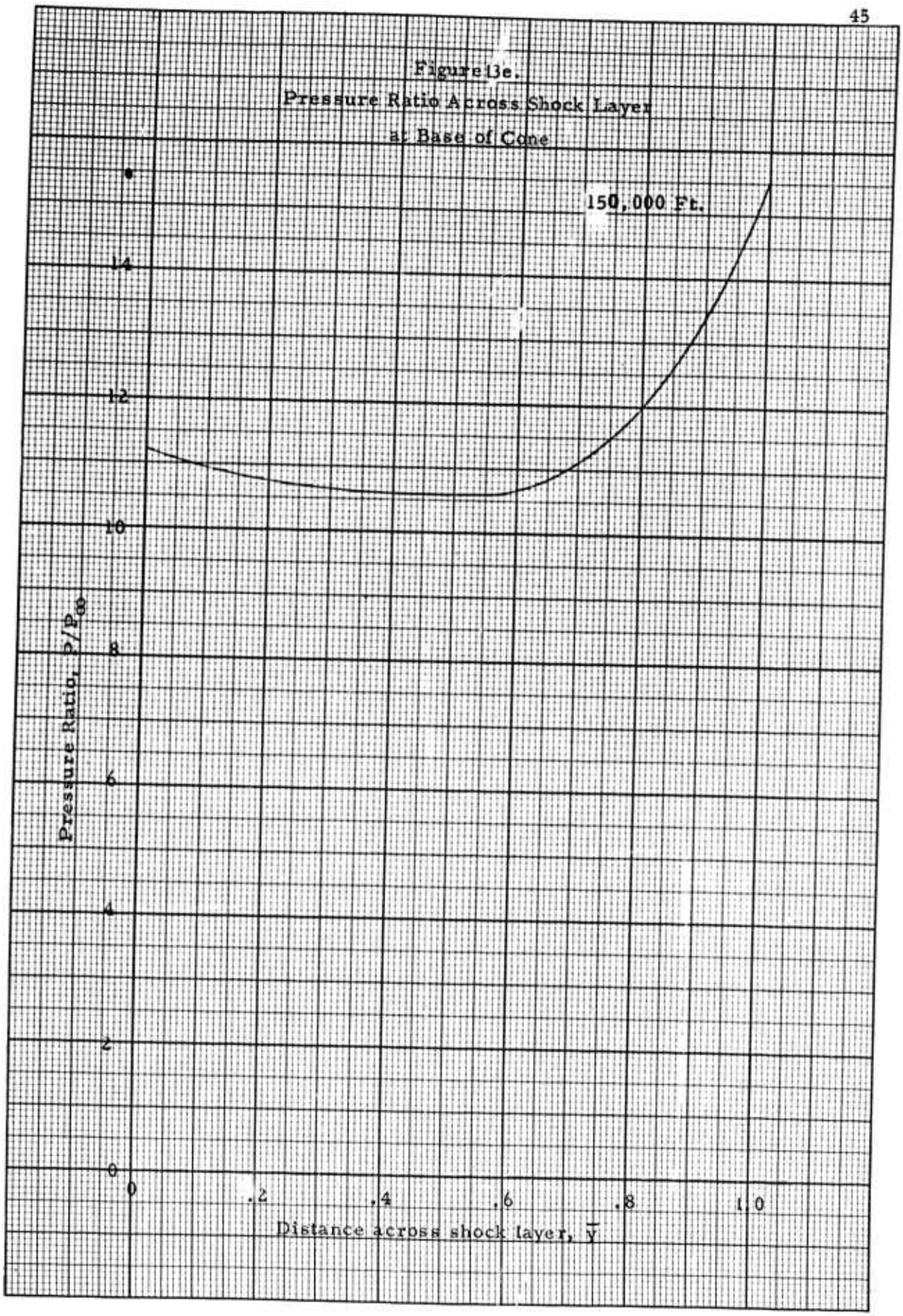

Figure 13f.
Pressure Ratio Across Shock Layer
at Base of Cone

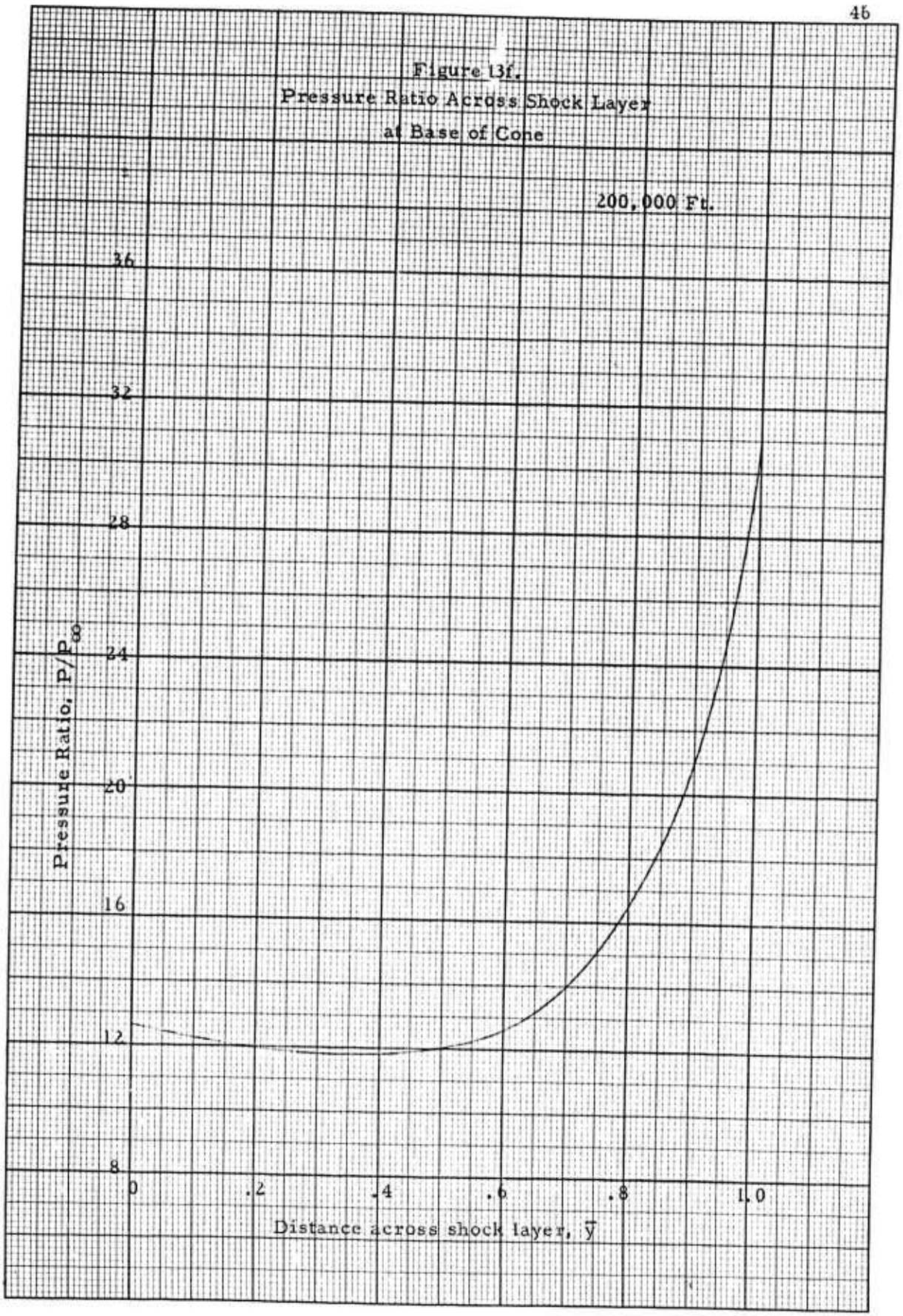

Figure 13 g.
Pressure Ratio Across Shock Layer
at Base of Cone

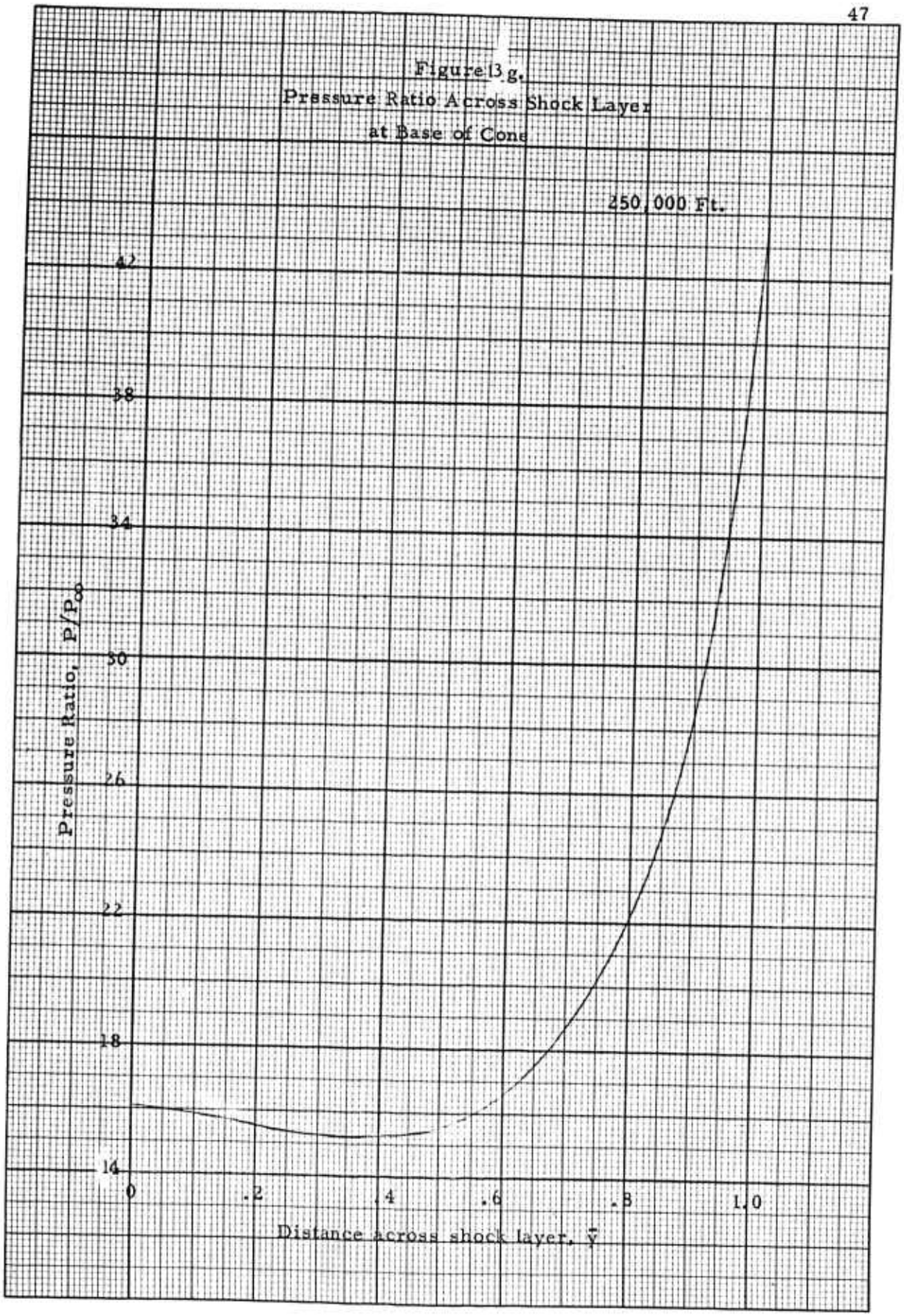

Figure 14a.

Density Ratio Across Shock Layer at Base of Cone

80,000 Ft. (Equilibrium)

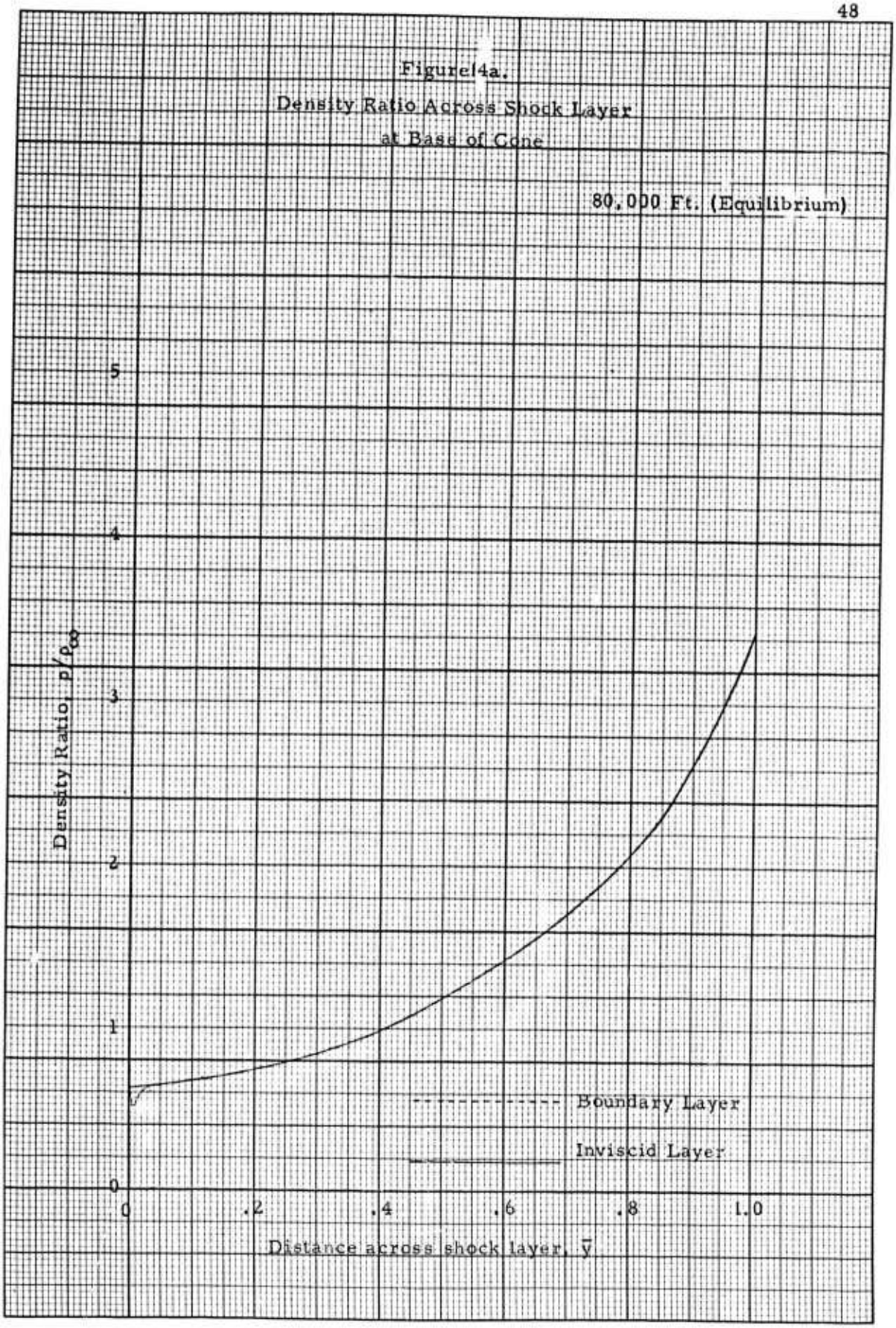

Figure 14b.

Density Ratio Across Shock Layer
at Base of Cone

80,000 Ft. (Frozen)

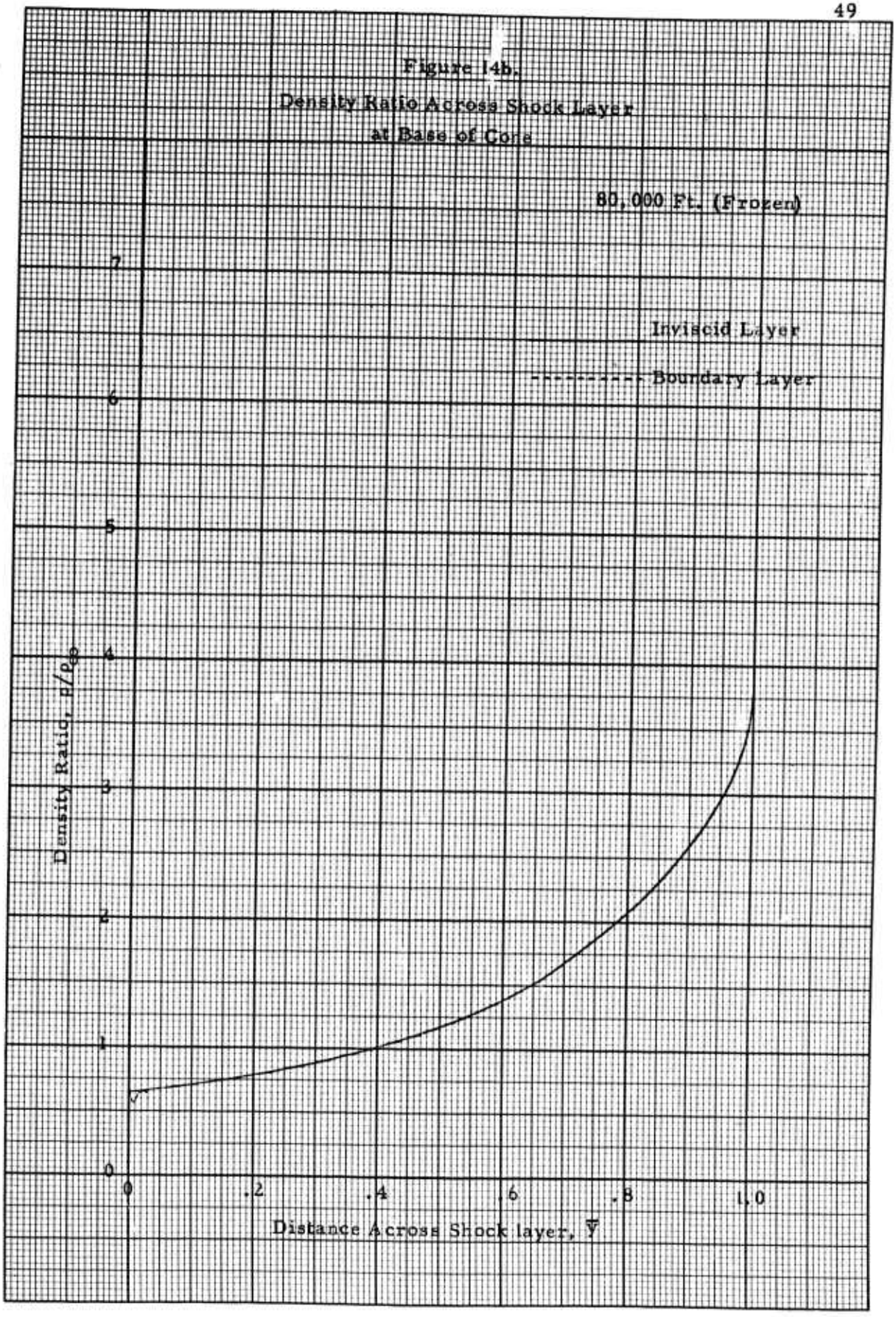

Figure 14c.
Density Ratio Across Shock Layer
at Base of Core

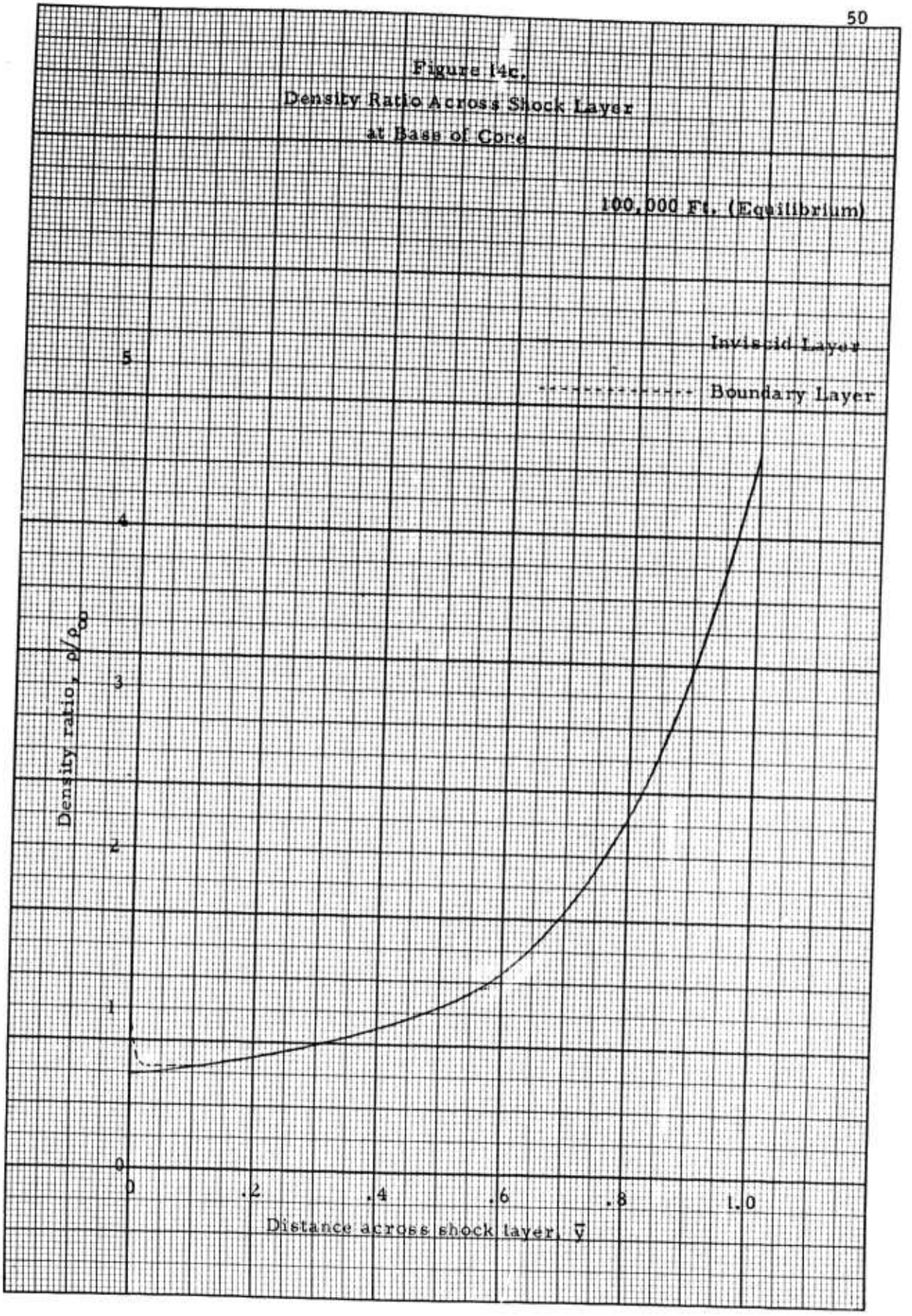

Figure 14d.
Density Ratio Across Shock Layer
at Base of Cone

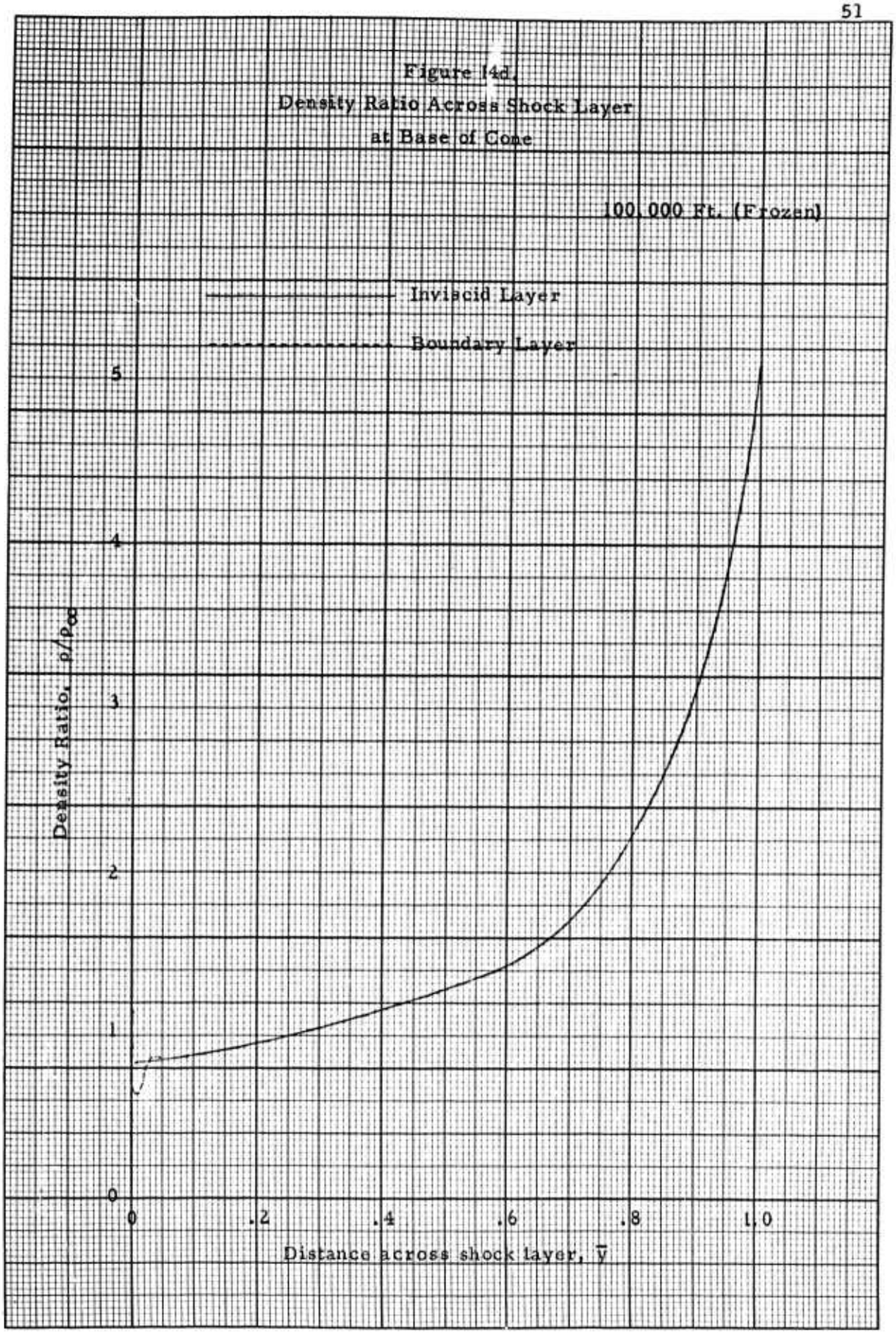

Figure 14e.

Density Ratio Across Shock Layer at Base of Cone

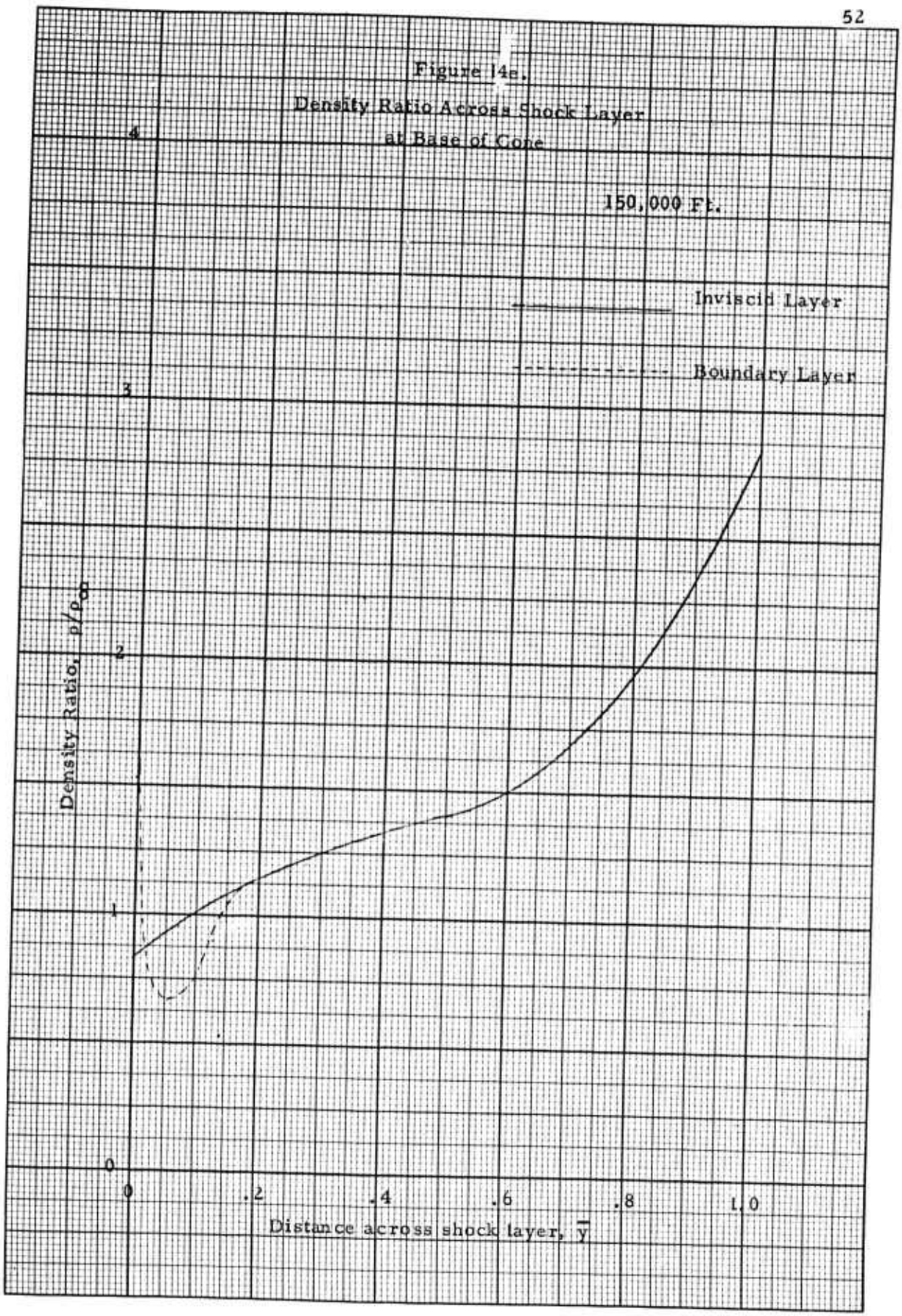

Figure 14f.
Density Ratio Across Shock Layer
at Base of Cone

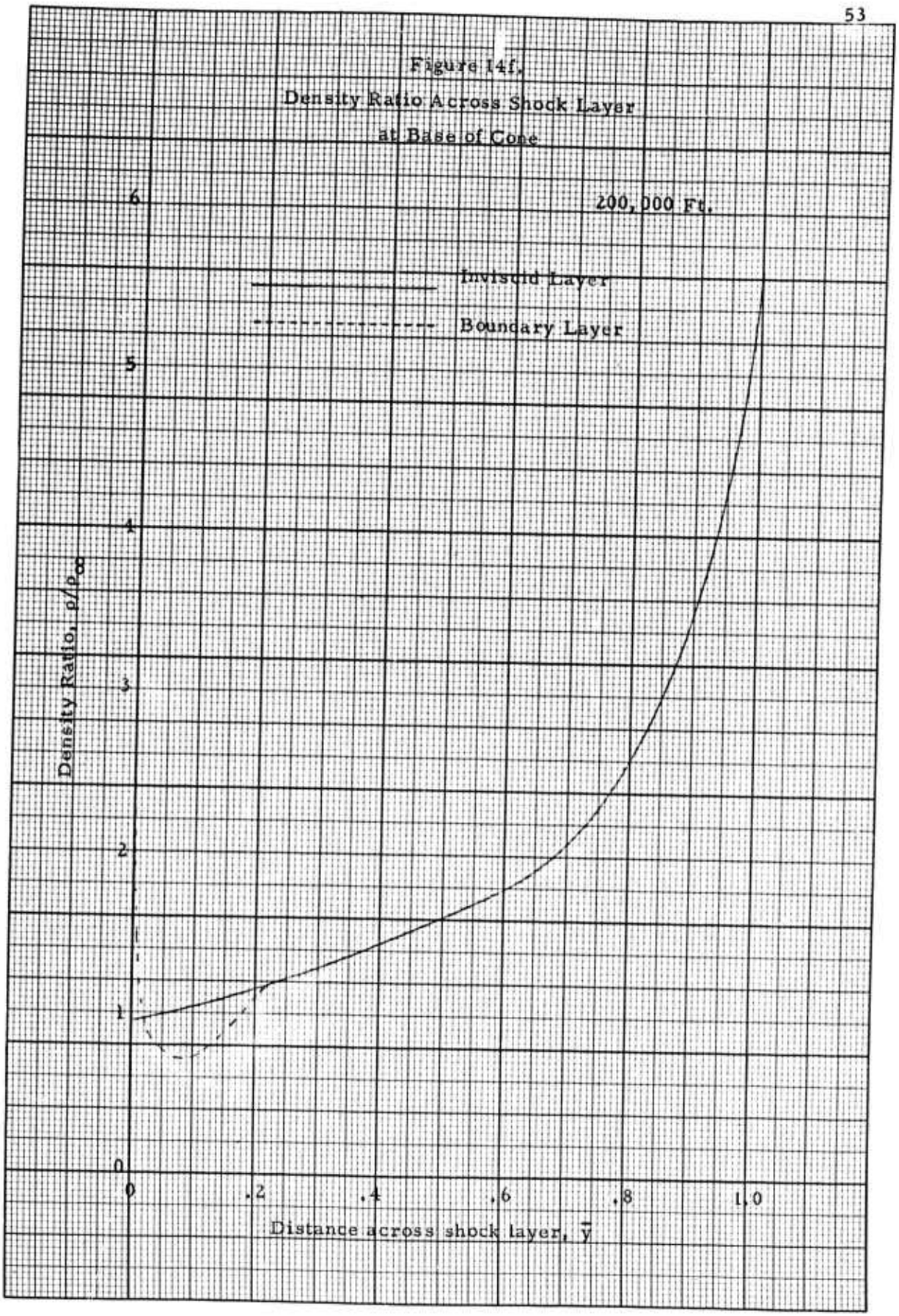

Figure 14g.
Density Ratio Across Shock Layer
at Base of Cone

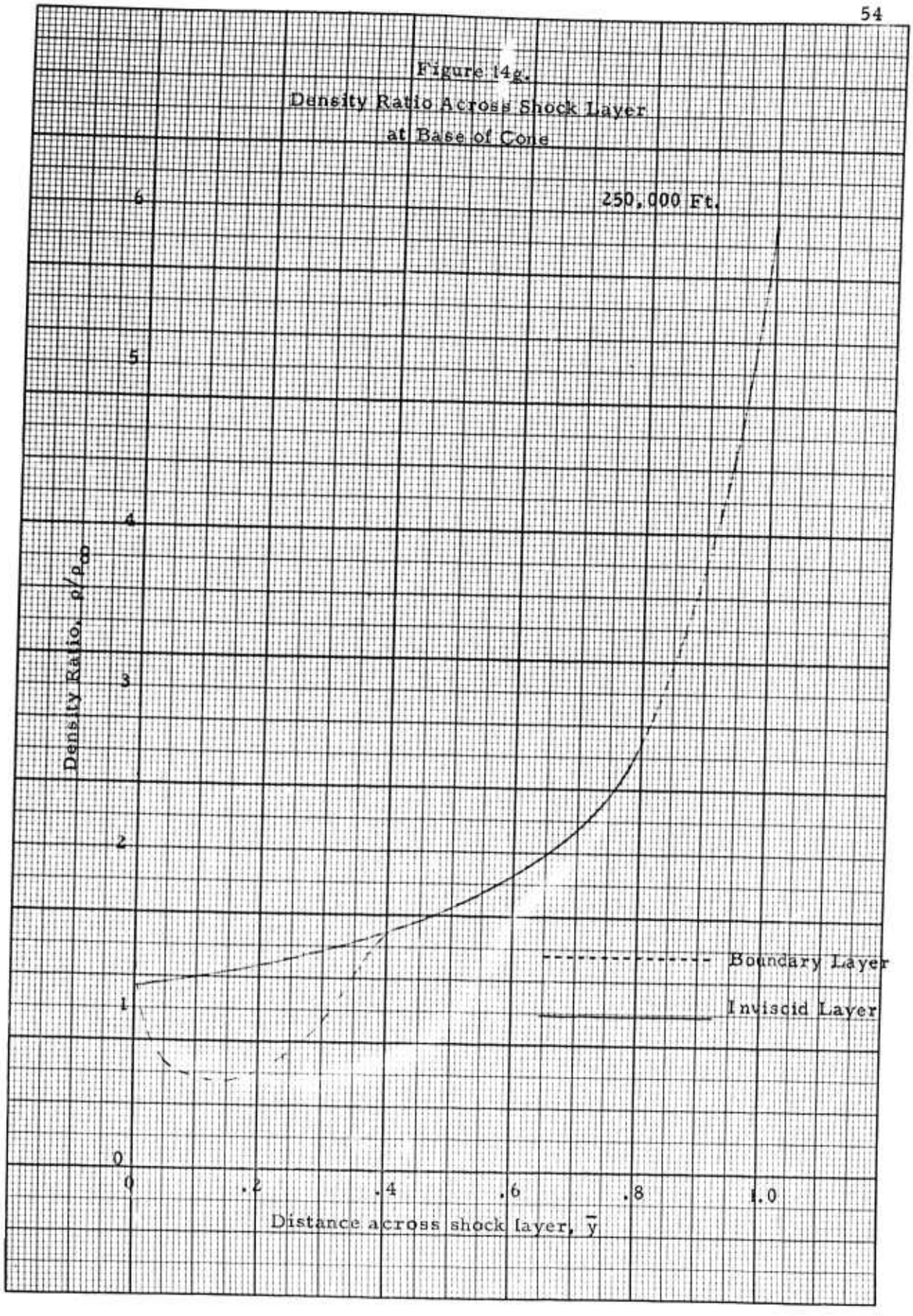

Figure 15a.

Temperature Distribution Across Shock Layer

at Base of Cone

80,000 Ft. (Equilibrium)

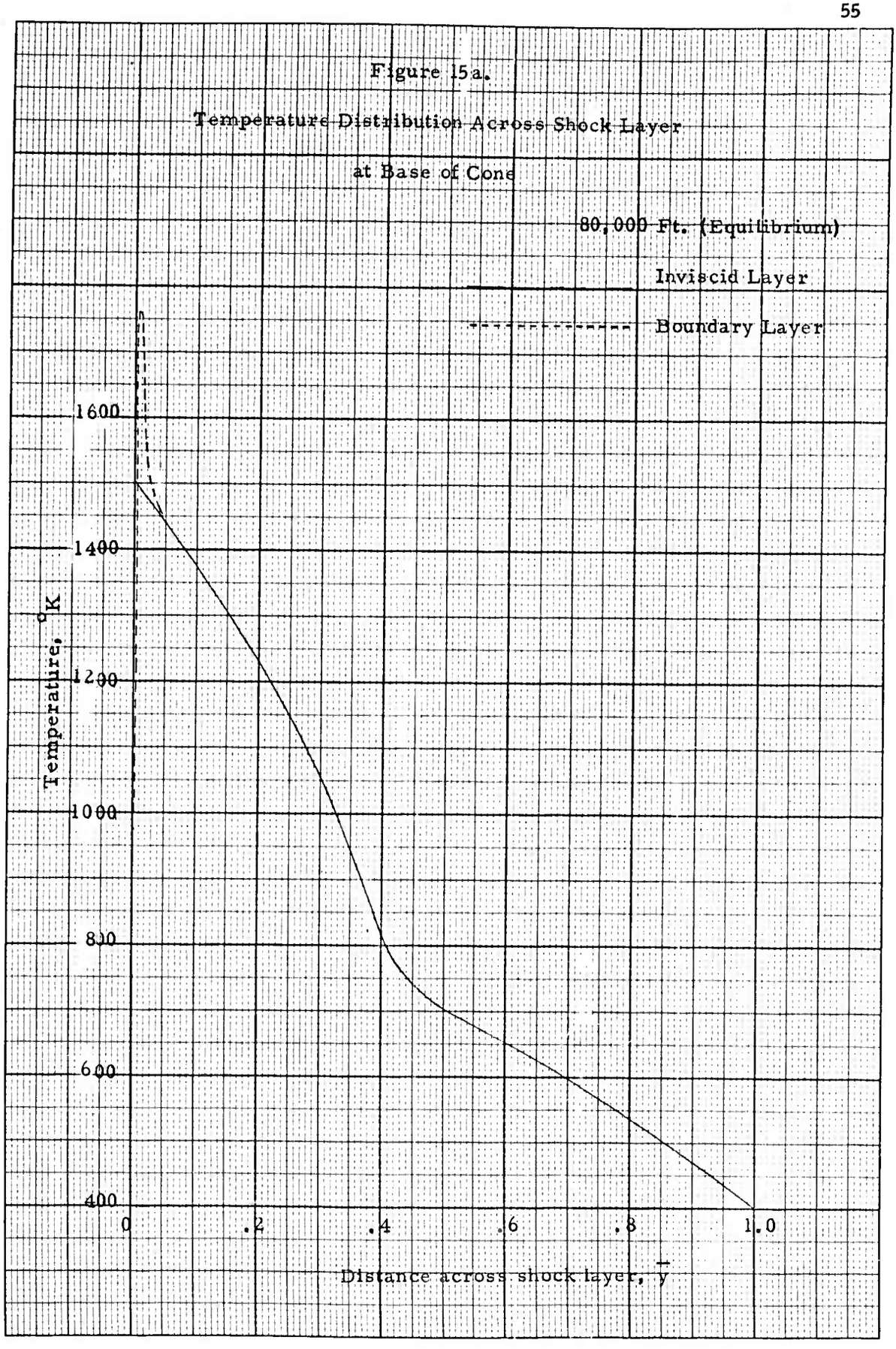

Figure 15b.

Temperature Distribution Across Shock Layer at Base of Cone

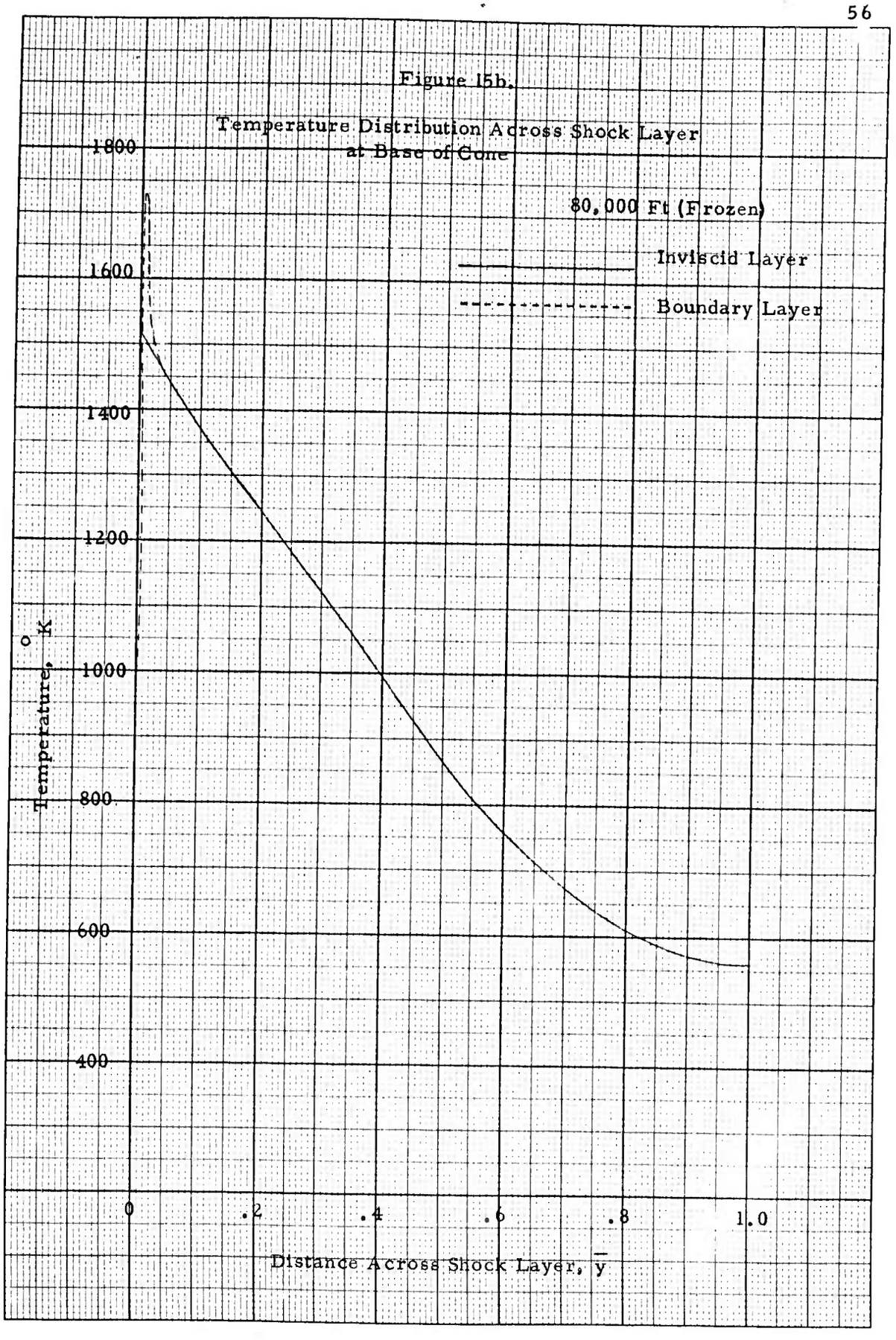

Figure 15c.

Temperature Distribution Across Shock Layer at Base of Cone

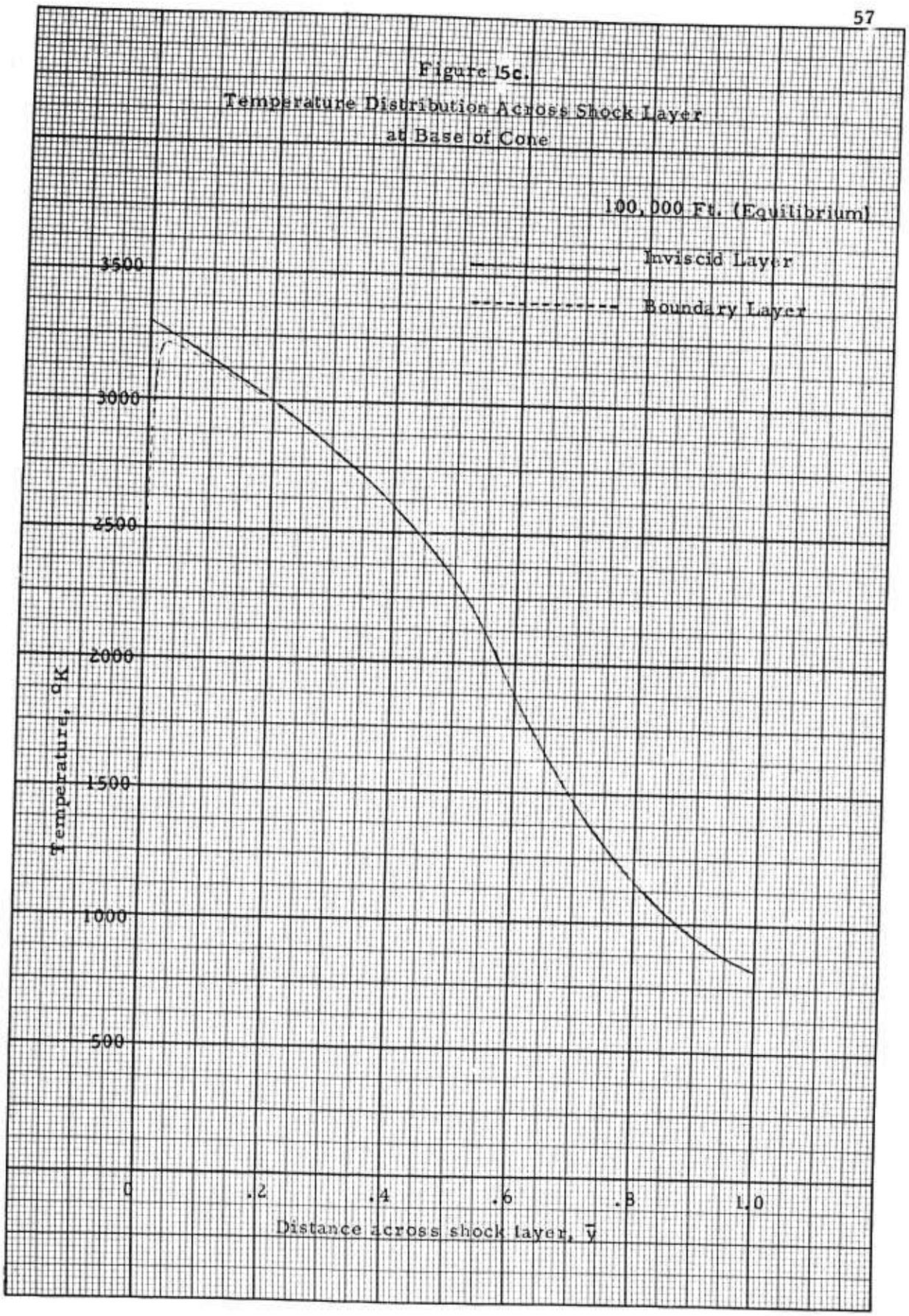

Figure 15 d.

Temperature Distribution Across Shock Layer
at Base of Cone

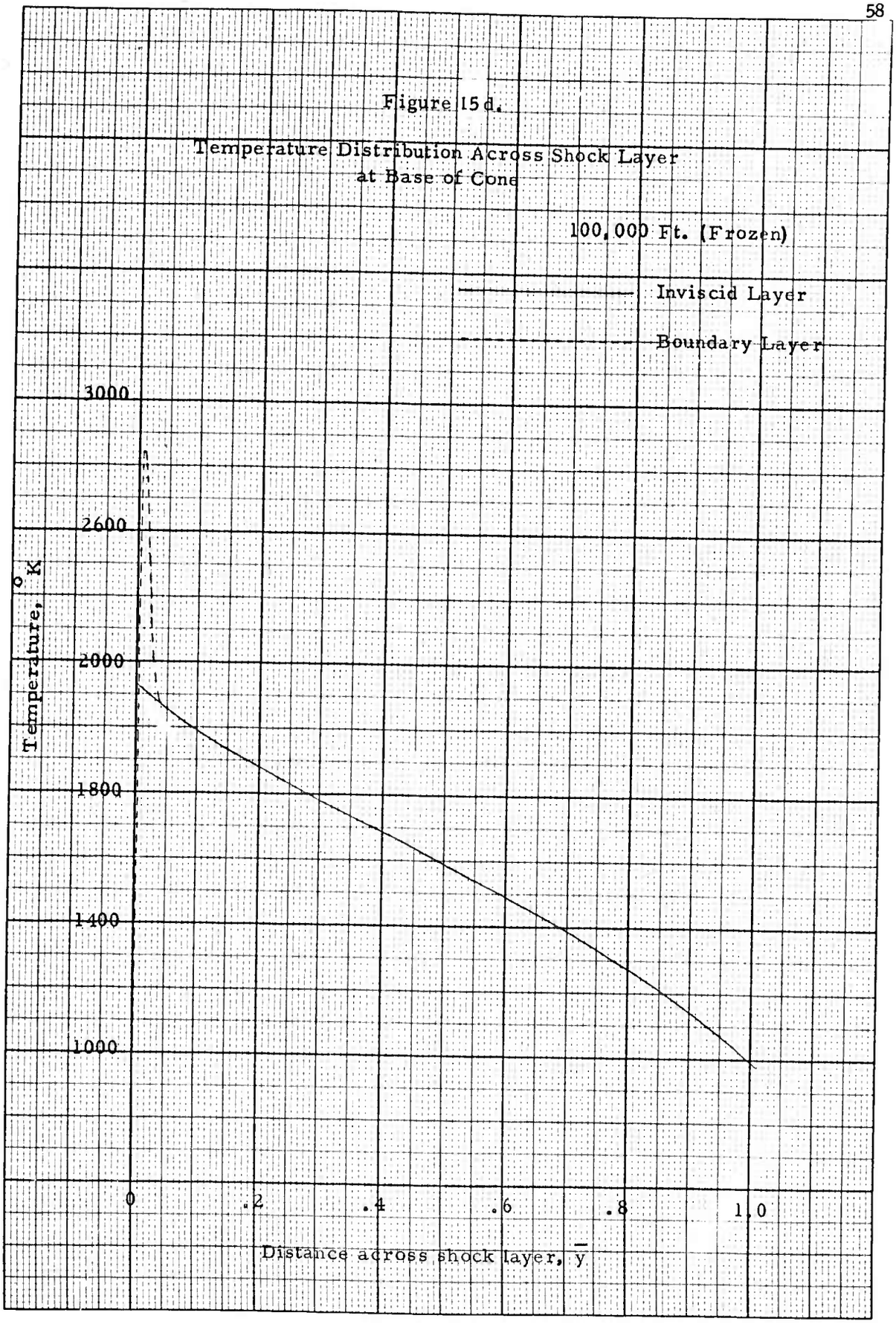

Figure 15e.

Temperature Distribution Across Shock Layer at Base of Cone

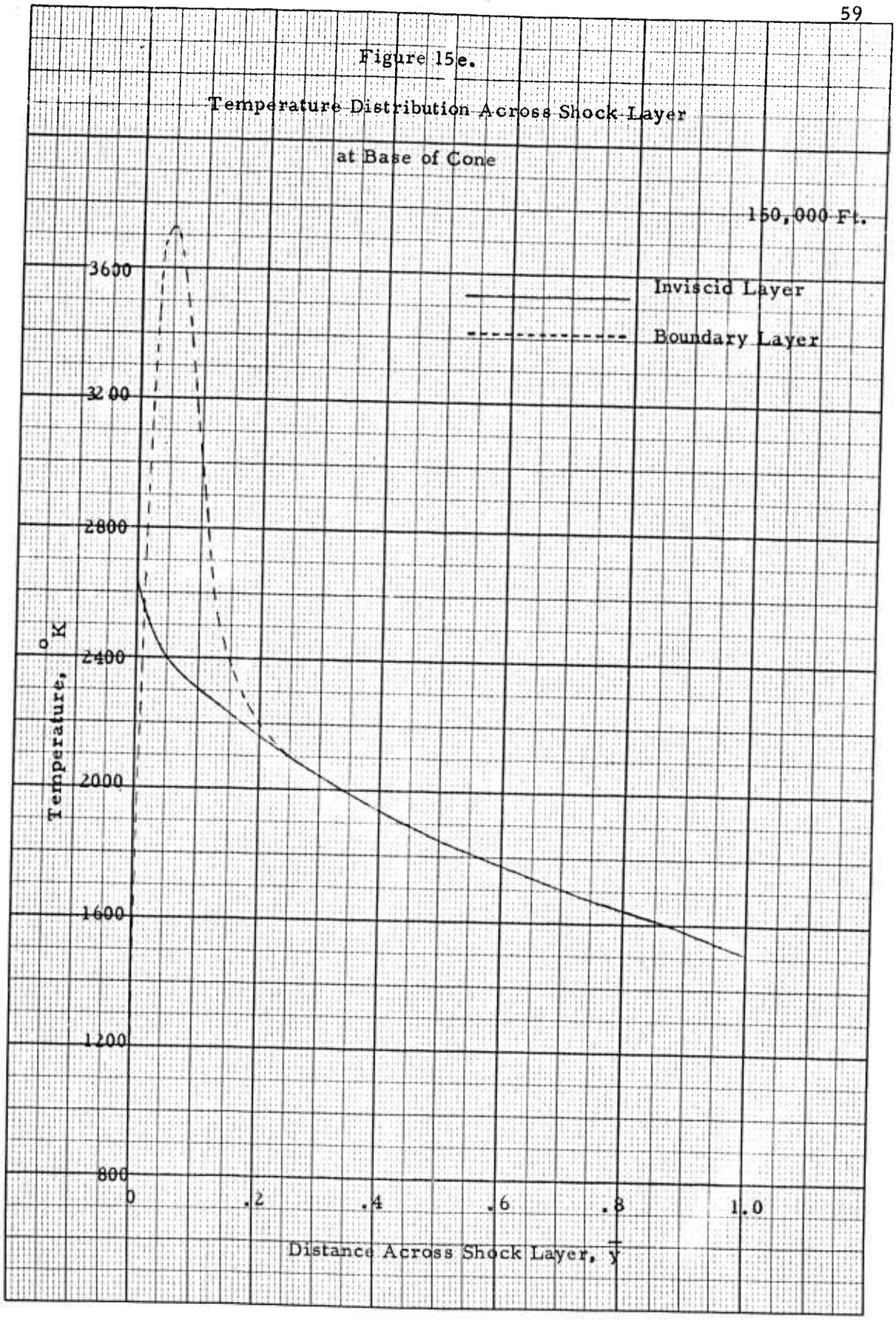

Figure 15f

Temperature Distribution Across Shock Layer at Base of Cone

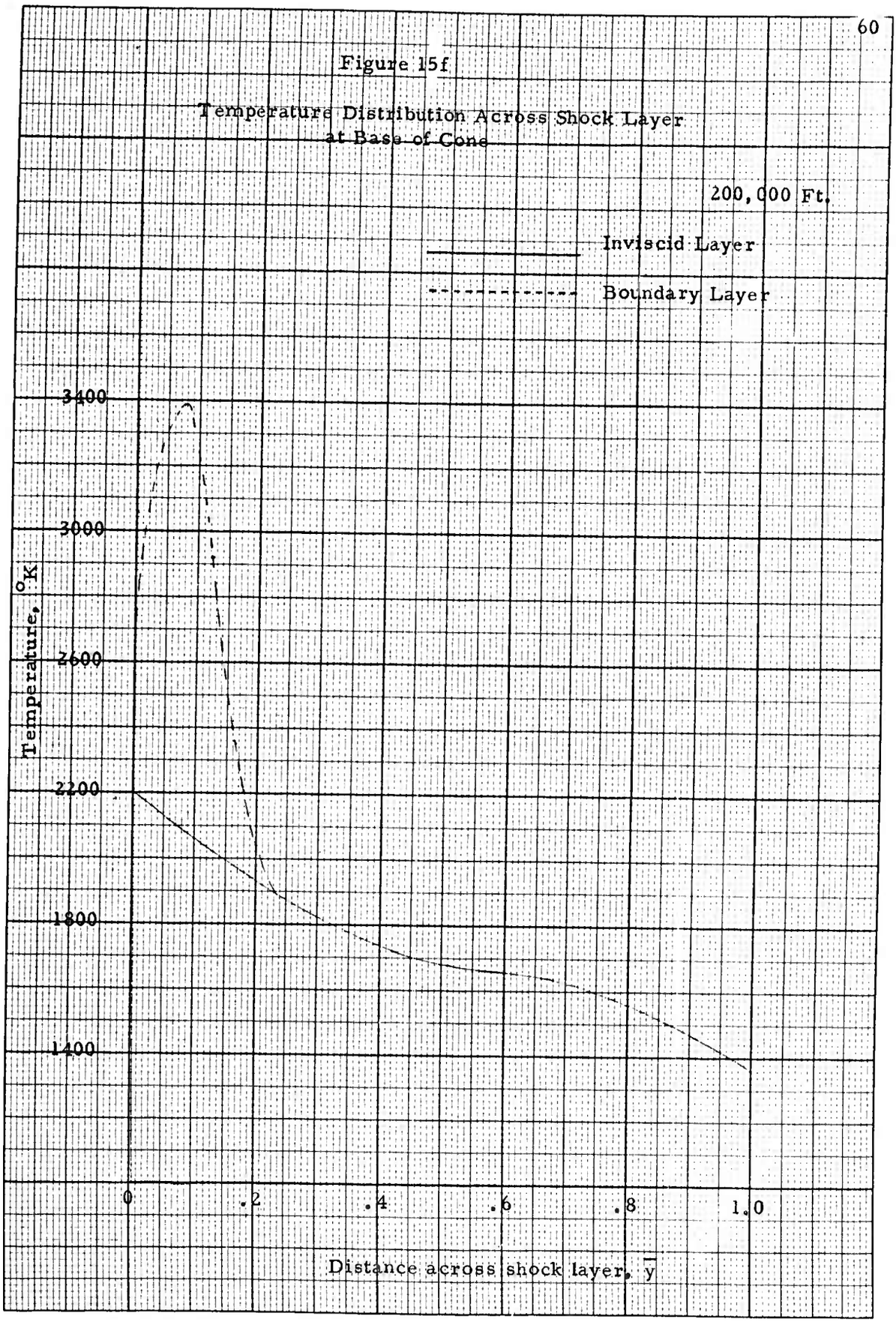

Figure 15g.

Temperature Distribution Across Shock Layer at Base of Cone

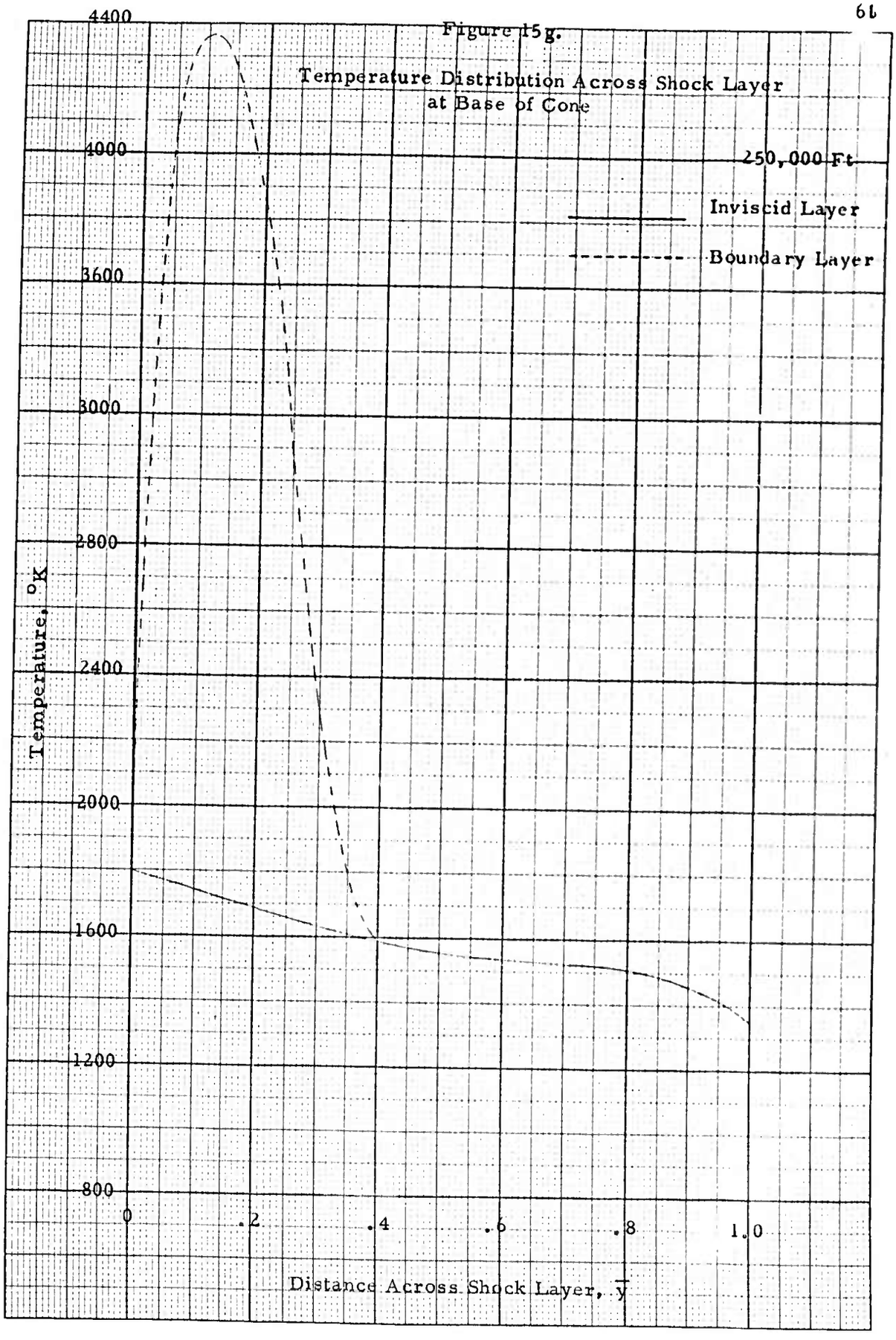

UNCLASSIFIED